NASA/TP—2013–217480

Elastic-Plastic J-Integral Solutions for Surface Cracks in Tension Using an Interpolation Methodology

P.A. Allen and D.N. Wells
Marshall Space Flight Center, Huntsville, Alabama

April 2013

The NASA STI Program…in Profile

Since its founding, NASA has been dedicated to the advancement of aeronautics and space science. The NASA Scientific and Technical Information (STI) Program Office plays a key part in helping NASA maintain this important role.

The NASA STI Program Office is operated by Langley Research Center, the lead center for NASA's scientific and technical information. The NASA STI Program Office provides access to the NASA STI Database, the largest collection of aeronautical and space science STI in the world. The Program Office is also NASA's institutional mechanism for disseminating the results of its research and development activities. These results are published by NASA in the NASA STI Report Series, which includes the following report types:

- TECHNICAL PUBLICATION. Reports of completed research or a major significant phase of research that present the results of NASA programs and include extensive data or theoretical analysis. Includes compilations of significant scientific and technical data and information deemed to be of continuing reference value. NASA's counterpart of peer-reviewed formal professional papers but has less stringent limitations on manuscript length and extent of graphic presentations.

- TECHNICAL MEMORANDUM. Scientific and technical findings that are preliminary or of specialized interest, e.g., quick release reports, working papers, and bibliographies that contain minimal annotation. Does not contain extensive analysis.

- CONTRACTOR REPORT. Scientific and technical findings by NASA-sponsored contractors and grantees.

- CONFERENCE PUBLICATION. Collected papers from scientific and technical conferences, symposia, seminars, or other meetings sponsored or cosponsored by NASA.

- SPECIAL PUBLICATION. Scientific, technical, or historical information from NASA programs, projects, and mission, often concerned with subjects having substantial public interest.

- TECHNICAL TRANSLATION. English-language translations of foreign scientific and technical material pertinent to NASA's mission.

Specialized services that complement the STI Program Office's diverse offerings include creating custom thesauri, building customized databases, organizing and publishing research results…even providing videos.

For more information about the NASA STI Program Office, see the following:

- Access the NASA STI program home page at <http://www.sti.nasa.gov>

- E-mail your question via the Internet to <help@sti.nasa.gov>

- Fax your question to the NASA STI Help Desk at 443–757–5803

- Phone the NASA STI Help Desk at 443–757–5802

- Write to:
  NASA STI Help Desk
  NASA Center for AeroSpace Information
  7115 Standard Drive
  Hanover, MD 21076–1320

NASA/TP—2013–217480

Elastic-Plastic J-Integral Solutions for Surface Cracks in Tension Using an Interpolation Methodology

P.A. Allen and D.N. Wells
Marshall Space Flight Center, Huntsville, Alabama

National Aeronautics and
Space Administration

Marshall Space Flight Center • Huntsville, Alabama 35812

April 2013

Acknowledgments

The authors would like to acknowledge James C. Newman, Jr. (Mississippi State University) and Ivatury S. Raju (NASA Langley) for their pivotal work on the linear-elastic stress intensity factor equations for surface cracks. The work of Dr. Newman and Dr. Raju has provided the foundation for a wealth of study into the fracture behavior of surface cracks. The authors would also like to thank Preston McGill (NASA Marshall Space Flight Center) for his thorough review of this paper. Finally, the authors would like to especially thank Robert H. Dodds Jr. (University of Illinois at Urbana-Champaign Professor Emeritus) for reviewing this paper and for his continual guidance, mentoring, and encouragement.

TRADEMARKS

Available from:

NASA Center for AeroSpace Information
7115 Standard Drive
Hanover, MD 21076–1320
443–757–5802

EXECUTIVE SUMMARY

No closed form solutions exist for the elastic-plastic *J*-integral for surface cracks due to the nonlinear three-dimensional (3D) nature of the problem. Traditionally, each surface crack case must be analyzed with a unique and time-consuming nonlinear finite element analysis (FEA). Additionally, knowledge of nonlinear FEA, plasticity theory, and elastic-plastic fracture mechanics is required to reliably execute this type of analysis. To simplify this process, the authors have developed and analyzed an array of 600 3D nonlinear finite element models for surface cracks in flat plates under tension loading. The solution space covers a wide range of crack shapes and depths (shape: $0.2 \leq a/c \leq 1$, depth: $0.2 \leq a/B \leq 0.8$) and material flow properties (elastic modulus to yield ratio: $100 \leq E/\sigma_{ys} \leq 1{,}000$, and hardening: $3 \leq n \leq 20$). The solution of this large array of nonlinear models was made practical by computer routines that automate the process of building the finite element models, running the nonlinear analyses, post-processing model results, and compiling and organizing the solution results into multidimensional arrays. The authors have developed a methodology for interpolating between the geometric and material property variables that allows the user to estimate the *J*-integral solution around the surface crack perimeter as a function of loading condition from the linear-elastic regime through the elastic-plastic regime. In addition to the *J*-integral solution, the complete force versus crack mouth opening displacement (*CMOD*) record is estimated. The solution space and interpolation routines have been extensively verified throughout the range of applicable geometries and materials. The user of this interpolated solution space need only know the crack and plate geometry and the basic material flow properties to reliably evaluate the full surface crack *J*-integral and force versus *CMOD* solution; thus, a solution can be obtained very rapidly by users without elastic-plastic fracture mechanics modeling experience. Enabling a convenient surface crack solution in the fully elastic-plastic domain, which up to now was only available for linear-elastic conditions, will significantly reduce the costs typically associated with evaluating elastic-plastic surface crack behavior. The authors hope this will promote advanced surface crack testing methodologies in the elastic-plastic regime and simplify aspects of surface crack structural assessment using the elastic-plastic *J*-integral.

TABLE OF CONTENTS

LIST OF FIGURES

LIST OF FIGURES (Continued)

LIST OF FIGURES (Continued)

LIST OF FIGURES (Continued)

LIST OF TABLES

LIST OF ACRONYMS, ABBREVIATIONS, AND DESIGNATORS

2D	two-dimensional
3D	three-dimensional
C(T)	compact tension
EPFM	elastic-plastic fracture mechanics
EPRI	Electric Power Research Institute
FEA	finite element analysis
FEM	finite element model
Int.	interpolation solution (see table 3)
LEFM	linear-elastic fracture mechanics
LPPL	linear plus power law
NR	Newman-Raju
RR	round robin
RSM	reference stress method

NOMENCLATURE

$2c$	total surface crack length
a	crack depth
B	plate thickness
c	half surface crack length
$CMOD$	crack mouth opening displacement
E	elastic modulus
g	geometry matrix
h_1	nondimensional influence factor
J_{el}	linear-elastic portion of J_{total}
J_n	normalized J-integral value
J_ϕ	J-integral value at a given parametric crack front angle
K_I	mode I linear-elastic stress intensity factor
L	plate length
M	crack front deformation level
m	material matrix
n	strain hardening exponent
P	force
$\bar{R}$	final interpolated result
$r_{\phi a}$ and $r_{\phi b}$	specimen characteristic lengths
W	plate width

NOMENCLATURE (Continued)

α	fitting constant
β	fitting constant
γ	fitting constant
δ	axial displacement
δ_{far}	far-field axial displacement
ε	engineering strain
ε_{pl}	plastic strain
ε_{ys}	yield strain
λ	geometry correction factor
ν	Poisson's ratio
σ	stress
σ_n	normalized far-field stress
σ_{net}	net section stress
σ_{ys}	material yield stress
ϕ	parametric crack front angle

TECHNICAL PUBLICATION

ELASTIC-PLASTIC J-INTEGRAL SOLUTIONS FOR SURFACE CRACKS IN TENSION USING AN INTERPOLATION METHODOLOGY

1. INTRODUCTION

Surface cracks are among the most common defects found in structural components and frequently reach failure once the limits of linear-elastic fracture mechanics (LEFM) have been exceeded and elastic-plastic fracture mechanics (EPFM) governs. For example, in the aerospace industry EPFM conditions commonly exist due to small critical crack sizes, thin walls, and high loading conditions inherent to lightweight, high-performance structures. Conversely, in the nuclear and petroleum industries EPFM conditions often prevail due to the use of lower strength, very high-toughness materials. EPFM assessment has become significantly more accessible through improved finite element interfaces such as FEACrack™ or ABAQUS® CAE,[1,2] but unfortunately the cost of such assessments in analysis time remains a significant impediment to common use. Similar difficulties arise in assessing laboratory fracture toughness tests with surface cracks. In these tests, due to practical specimen size limitations, the material fracture toughness is commonly not reached until well beyond the LEFM limit. Surface crack fracture testing is hindered significantly by the lack of a readily available set of surface crack solutions for the nonspecialist to evaluate the elastic-plastic J-integral, crack mouth opening displacement ($CMOD$) values, or deformation state of a test specimen at fracture. A convenient set of elastic-plastic surface crack solutions could help mitigate many of these obstacles.

Figure 1 illustrates a typical semielliptical surface crack in a flat plate in tension, where W is the total width of the plate, L is the length, B is the thickness, $2c$ is the total surface crack length, and a is the crack depth. The parametric crack front angle, ϕ, is defined in the conventional form as shown in section A-A of figure 1 where $\phi = 0°$ and 180° at the free surface, and $\phi = 90°$ at the deepest point of the crack. The $CMOD$ is defined as the axial displacement between the two crack mouth faces on the free surface of the plate at the centerline of the crack. A uniform far-field displacement, δ, or stress, σ, is designated by the arrows on the top and bottom faces of the plate.

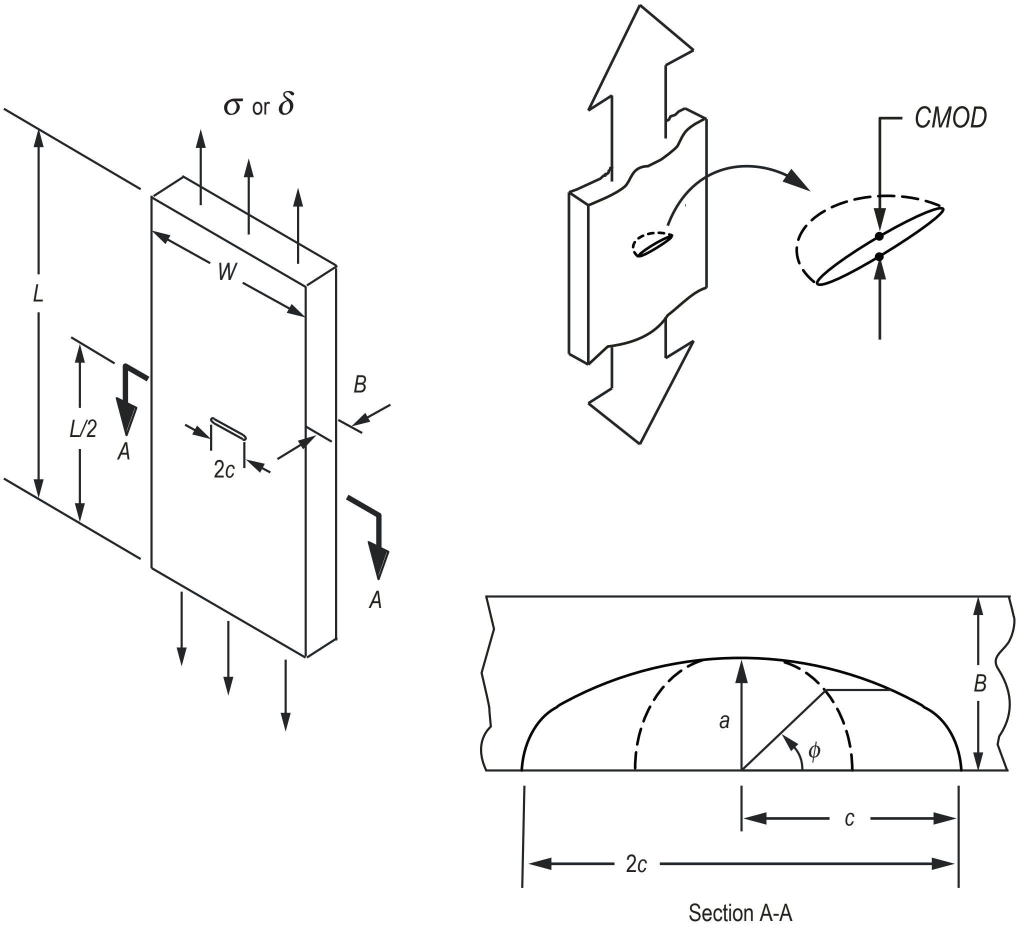

Figure 1. Semielliptical surface crack in a flat plate.

The Newman-Raju (NR) equations[3,4] provide a robust and convenient linear-elastic stress intensity (K_I) solution for surface cracks in tension and bending. Other common linear-elastic codes, such as NASGRO® utilize an interpolated table look-up approach for surface crack K_I solutions.[5] Unfortunately, no concise solutions exist for elastic-plastic surface cracks due to their nonlinear three-dimensional (3D) nature. The contemporary method for solving the elastic-plastic surface crack problem requires a unique and time-consuming nonlinear finite element analysis (FEA) for each surface crack geometry of interest. To reliably execute this type of analysis requires knowledge of nonlinear FEA, plasticity theory, and EPFM. In the years prior to the advent of routine finite element based fracture mechanics analysis, many researchers provided alternative and robust engineering solutions to the elastic-plastic surface crack problem, though subject to many practical limitations. An excellent summary of the development of elastic-plastic *J*-integral solutions up to the year 1999 is given by McClung et al.[6] Apart from FEA, the commonly used methods for calculating elastic-plastic *J*-integral solutions usually follow one of two basic techniques:[7] the Electric Power Research Institute (EPRI) approach[8–10] or the reference stress method (RSM).[11] The EPRI method assumes a Ramberg-Osgood[12] material stress-strain behavior, requires an estimate for the yield load, and requires the use of nondimensional h_1 influence factors in the calculation of the *J*-integral. The h_1 influence factors are a function of both constitutive relationship and geometry and are obtained from a fully plastic elastic-plastic finite element solution. Tables of h_1 factors for surface cracks in flat plates have been generated by several researchers[6,13–15] for limited combinations of material properties, geometry values, and surface crack front angle, ϕ. Yagawa et al.[13] also developed influence factors for the fully plastic crack opening displacement for the geometries and materials covered in their study. In addition, Kim et al.[16] performed investigations into the RSM for a limited number of surface crack geometries and Ramberg-Osgood material combinations.

The EPRI and RSM techniques have found wide application in analysis of structures but have limited application in the assessment of surface crack laboratory tests. To understand with sufficient precision the crack front conditions at the point the fracture toughness is reached in an experimental surface crack test requires knowledge of the force, P, versus $CMOD$ response, the elastic-plastic deformation state of the specimen, and detailed knowledge of the J-integral versus ϕ relationship as a function of deformation. The current RSM and EPRI solutions for surface cracks do not provide the user with the full P versus $CMOD$ trace which serves as the most fundamental connection between experiment and analysis. The $CMOD$ value provides the most robust predictor of the J-integral values at the crack tip.[7,17] Most conventional fracture toughness test specimens such as the compact tension, C(T), or single edge notched bend are considered two-dimensional (2D) in nature and report a single value of fracture toughness representing the average driving force along the entire crack front. Conversely, the surface crack toughness test is highly 3D, and the toughness values are usually reported as a single, local value of toughness at a given ϕ location along the crack front. Most of the current RSM and EPRI solutions only have solution values at a limited number of ϕ locations. In addition, the EPRI and RSM techniques have J versus ϕ relationships that are based on either linear-elastic solutions (RSM) or fully plastic solutions (EPRI) which do not capture the changes in the J versus ϕ distribution and maximum J-integral location with increasing deformation.

To overcome these shortcomings and provide a simple and robust method for analyzing surface crack tension tests, the authors have developed and analyzed an array of 600, 3D nonlinear finite element models (FEMs) for surface cracks in flat plates under tension loading. The solution space covers a wide range of crack geometric parameters and material properties. The solution of this large array of nonlinear models was made practical by computer routines that automate the process of building the FEMs, running the nonlinear analyses, post-processing model results, and compiling and organizing the solution results into multidimensional arrays. The authors have developed a methodology for interpolating between the geometric and material property variables that allows the user to estimate the J-integral solution around the surface crack perimeter (ϕ) as a function of loading condition from the linear-elastic regime through the elastic-plastic regime. In addition to the J-integral solution, the complete force versus $CMOD$ record is estimated. The user of this interpolated solution space need only know the crack and plate geometry and the basic material flow properties to reliably evaluate the full surface crack J-integral and force versus $CMOD$ solution; thus, a solution can be obtained very rapidly by users without EPFM modeling experience.

2. COMPUTATIONAL PROCEDURES

This project is logistically intense. Though computationally, each part of the process of building this new solution space follows mostly well-established paths, combining those parts effectively into a functional whole requires planning at every level. This section provides insight into the basic computational procedures used in the FEMs which constitutes the solution space as well as the parameters of the geometric and material property variables that define the overall solution space. Briefly discussed in the conclusion are the logistics of building, executing, and then assembling the solution space—made practical only through automation.

2.1 Constitutive Model

The constitutive model for this study employs incremental von Mises plasticity theory in a conventional small geometry change (small strain) setting. The material is assumed to be isotronic and homogenous with flow behavior following a linear plus power law (LPPL) representation of the stress-strain response. For the LPPL model, the uniaxial stress-strain curve follows a linear then power law model given by

$$\frac{\varepsilon}{\varepsilon_{ys}} = \frac{\sigma}{\sigma_{ys}} \quad \varepsilon \le \varepsilon_{ys}; \quad \frac{\varepsilon}{\varepsilon_{ys}} = \left(\frac{\sigma}{\sigma_{ys}}\right)^n \quad \varepsilon > \varepsilon_{ys} \quad , \tag{1}$$

where ε is engineering strain, n is the strain hardening exponent, σ is engineering stress, σ_{ys} is a representative yield stress, and ε_{ys} is a corresponding yield strain defined by $\varepsilon_{ys} = \sigma_{ys}/E$, with the elastic modulus, E. For this analytical work, σ_{ys} is equivalent to the proportional limit and defines the limits of the initial linear-elastic portion of the response. This approach to modeling the stress-strain response has numerous advantages in this study: first, the model lends itself to easy implementation in the planned material space because the curve is fully defined by three parameters (σ_{ys}, ε_{ys} or E, and n); second, the model faithfully represents the stress-strain response of a large majority of structural metals; and third, unlike the commonly used Ramberg-Osgood model, prior to exceeding the yield strain, the LPPL model is purely linear-elastic, and thus does not prematurely accumulate plastic strain. Unlike the research FEA code utilized for this study, WARP3D,[18] most commercial finite element codes do not natively support the LPPL model for plasticity analysis. Therefore, to make the analysis methods used in this study more universally repeatable in other analysis codes, the smooth LPPL representation of the material response for $\varepsilon > \varepsilon_{ys}$ was discretized into 20 line segments for use in the commonly available, multilinear stress-strain curve representation. In this way, the common and convenient way of describing the plastic hardening behavior through the hardening exponent, n, could be retained but the analysis performed in a way that is not dependent on the availability of a native LPPL model. The plastic strain, ε_{pl}, increments for each multilinear line segment were gradated from initially fine increments of 0.001 for eight line segments, to 0.005 for four line segments and then to 0.01 for the remaining seven line segments to ensure a smooth transition from linear-elastic to nonlinear behavior and to smoothly capture the power law hardening behavior. Figure 2 illustrates the multilinear representation of the LPPL plastic response for a material with a yield strain, $\varepsilon_{ys} = 0.00\overline{3}$ (normalized elastic modulus of E/σ_{ys}=300) and various n values.

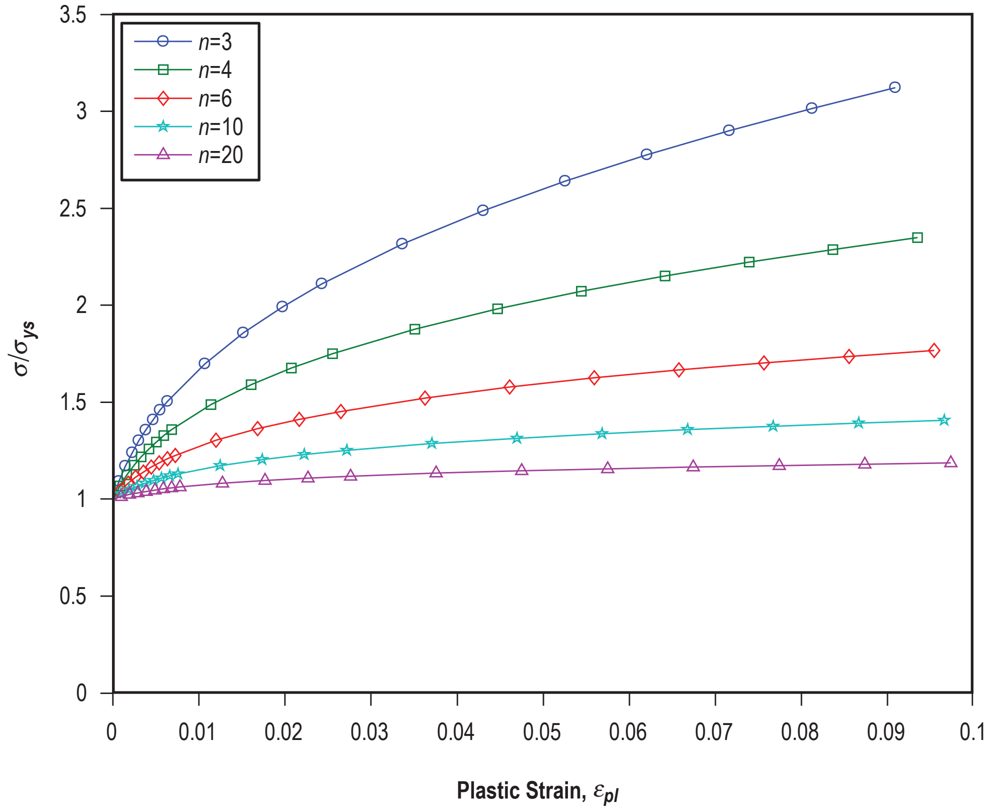

Figure 2. Multilinear representation of the LPPL material for $E/\sigma_{ys} = 300$ and various values of n.

2.2 Solution Space

The solution space for this array of models is four-dimensional. Two dimensions are used to describe surface crack geometric variation, and two dimensions are used to describe material property variation. The inclusion of nonlinear materials uniquely separates this work from previous surface crack solutions for K_I, the material independent linear-elastic stress intensity factor. The material and geometric spaces must be carefully crafted to provide sufficient coverage for most common engineering problems without becoming so large as to be intractable. The following sections discuss the choices and reasoning for the material and geometric dimensions of the solution space.

2.2.1 Material Space

As discussed above, the LPPL model for the stress-strain curve is fully defined by just three parameters. If the yield strength is normalized to unity for all materials ($\sigma_{ys} = 1$), then only ε_{ys} and n are required to define the shape of the stress-strain curve throughout the space. For convenience of eliminating small fractional numbers, the reciprocal of the yield strain is commonly used, E/σ_{ys}.

Figure 3 illustrates the material space for the study described in terms of the six E/σ_{ys} and five n values resulting in 30 different material combinations. In all cases, $\sigma_{ys}=1$ and Poisson's ratio, $\nu=0.3$. The names of several common engineering materials are overlaid on the material matrix in figure 3 to illustrate how some common materials are represented in the material matrix. The low E/σ_{ys} values of 100 to 200 are materials capable of high values of elastic strain, thus they have low elastic modulus and relatively high yield strength, such as many high-performance titanium and aluminum alloys. The opposite end of the E/σ_{ys} space with values of E/σ_{ys}=1,000 have very little elastic strain capability due to high elastic modulus and low yield strength. Austenitic stainless steels are a common example of this material class. To practitioners not accustomed to considering materials based on the E/σ_{ys} ratio, it is important to realize that, for a fixed hardening exponent, n, the nonlinear material response is governed by this ratio. Materials that may not seem alike from an engineering perspective are actually equivalent in their nonlinear response. For example, consider three materials with similar n and equivalent yield strains such that $E/\sigma_{ys}=400$ in each case. This could easily be an aluminum alloy with yield strength around 180 MPa, a titanium alloy with yield strength around 275 MPa, or a steel alloy with yield strength around 500 MPa. The normalized nonlinear response is the same in each case. This will be discussed further in a following section on normalization schemes. The effect of E/σ_{ys} on the load, P, versus $CMOD$ behavior (and the resulting J-integral values) is strongest for lower values of E/σ_{ys}; therefore, the authors chose smaller increments of E/σ_{ys} for $E/\sigma_{ys}\leq 300$ to provide more uniform coverage over the solution space.

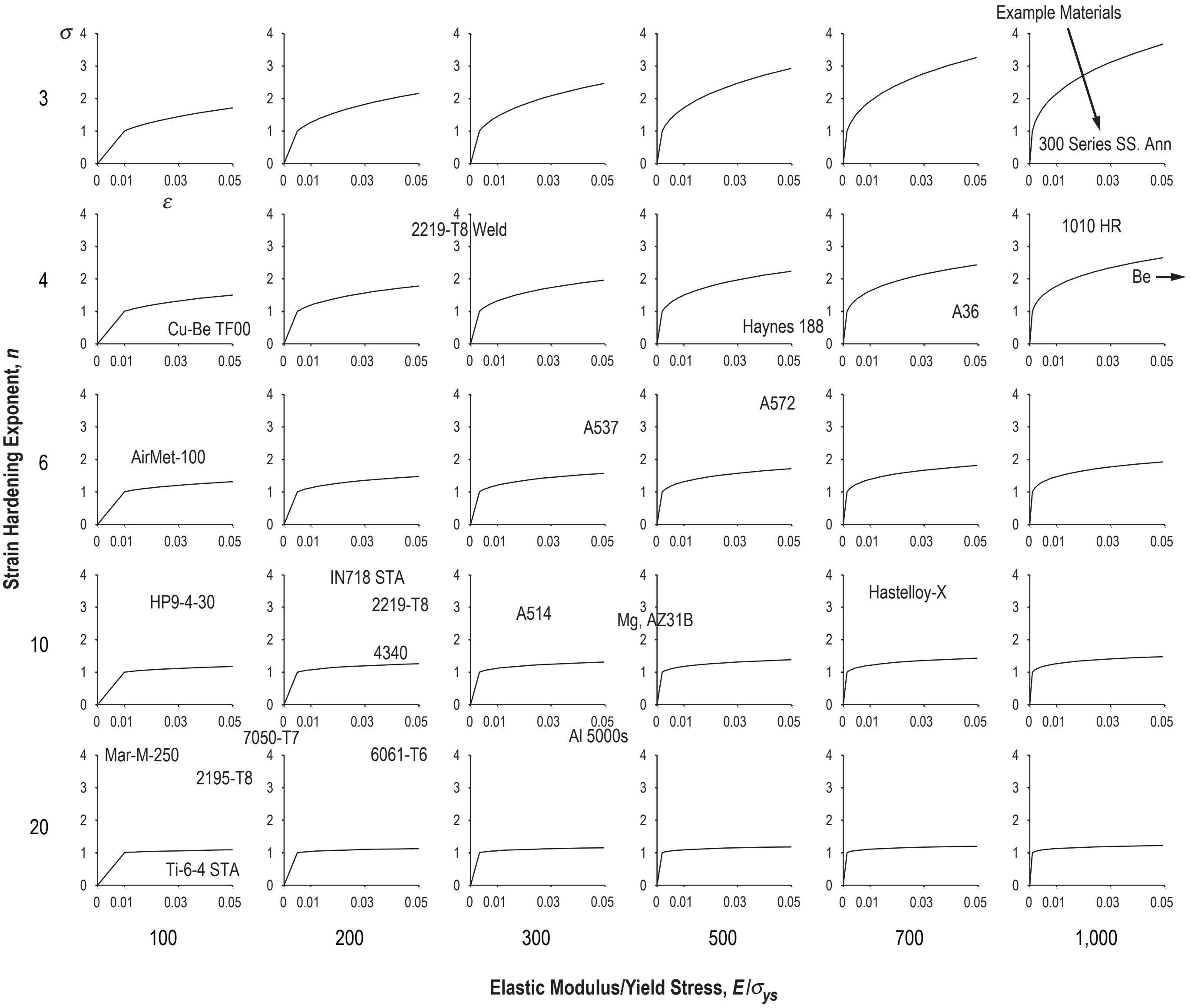

Figure 3. Material space.

The other dimension of the material space is the strain hardening exponent, n. The values of n range from 3 to 20, spanning the hardening characteristics of most all structural metals from very high strain hardening ($n=3$) to almost elasticly perfect plastic behavior ($n=20$). The specific values of n for this study were chosen to uniformly divide the strain hardening response in the σ versus ε_{pl} space as shown in figure 2.

2.2.2 Geometric Space

Figure 4 illustrates the geometric space for this study as sketches of cross sections through the crack plane arranged in terms of crack depth-to-thickness ratio (a/B) and crack depth-to-half-length ratio (a/c) with $0.2 \le a/c \le 1$ and $0.2 \le a/B \le 0.8$ for a total of 20 different geometries. For each a/B and

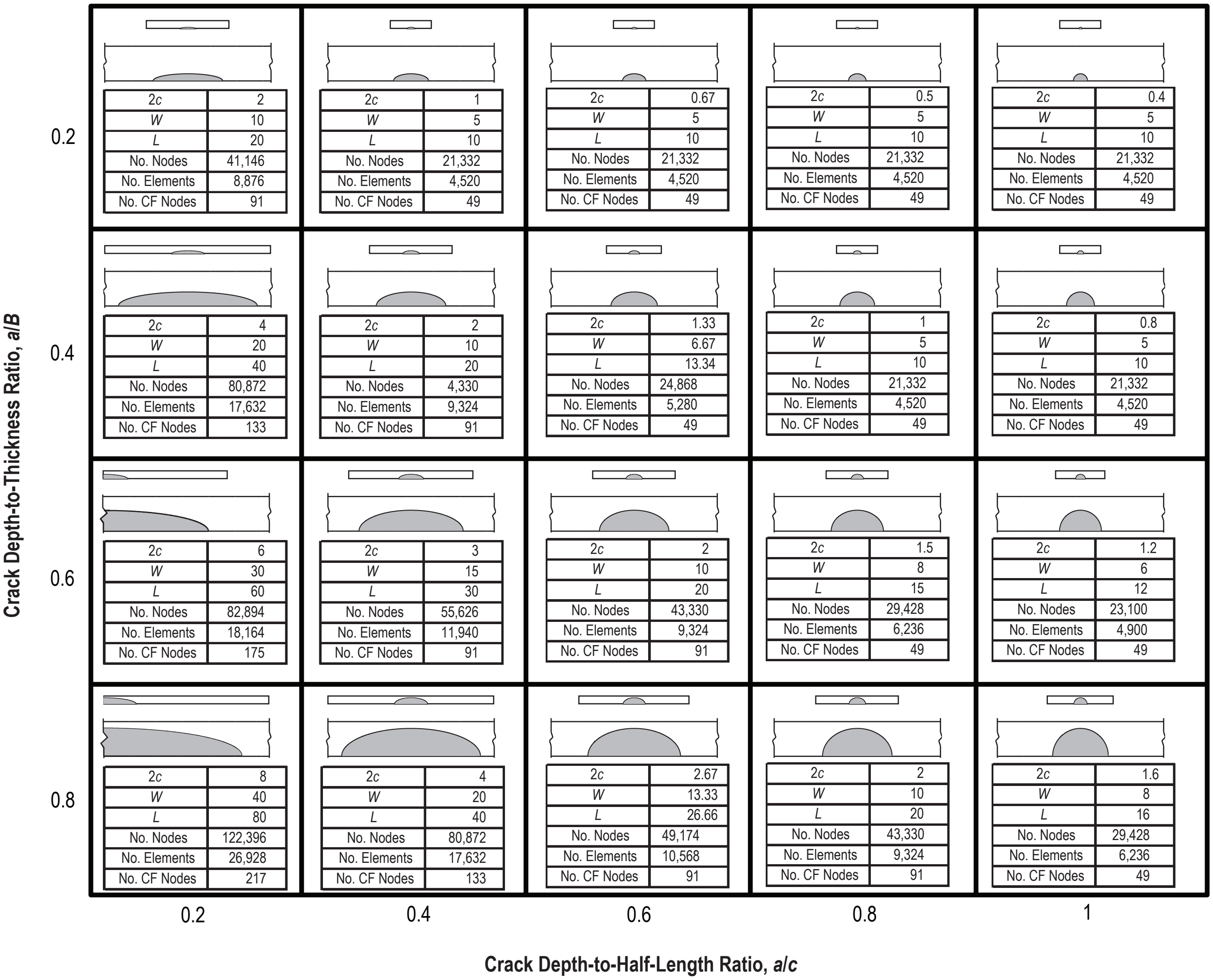

2*c*	2
W	10
L	20
No. Nodes	41,146
No. Elements	8,876
No. CF Nodes	91

2*c*	1
W	5
L	10
No. Nodes	21,332
No. Elements	4,520
No. CF Nodes	49

2*c*	0.67
W	5
L	10
No. Nodes	21,332
No. Elements	4,520
No. CF Nodes	49

2*c*	0.5
W	5
L	10
No. Nodes	21,332
No. Elements	4,520
No. CF Nodes	49

2*c*	0.4
W	5
L	10
No. Nodes	21,332
No. Elements	4,520
No. CF Nodes	49

2*c*	4
W	20
L	40
No. Nodes	80,872
No. Elements	17,632
No. CF Nodes	133

2*c*	2
W	10
L	20
No. Nodes	4,330
No. Elements	9,324
No. CF Nodes	91

2*c*	1.33
W	6.67
L	13.34
No. Nodes	24,868
No. Elements	5,280
No. CF Nodes	49

2*c*	1
W	5
L	10
No. Nodes	21,332
No. Elements	4,520
No. CF Nodes	49

2*c*	0.8
W	5
L	10
No. Nodes	21,332
No. Elements	4,520
No. CF Nodes	49

2*c*	6
W	30
L	60
No. Nodes	82,894
No. Elements	18,164
No. CF Nodes	175

2*c*	3
W	15
L	30
No. Nodes	55,626
No. Elements	11,940
No. CF Nodes	91

2*c*	2
W	10
L	20
No. Nodes	43,330
No. Elements	9,324
No. CF Nodes	91

2*c*	1.5
W	8
L	15
No. Nodes	29,428
No. Elements	6,236
No. CF Nodes	49

2*c*	1.2
W	6
L	12
No. Nodes	23,100
No. Elements	4,900
No. CF Nodes	49

2*c*	8
W	40
L	80
No. Nodes	122,396
No. Elements	26,928
No. CF Nodes	217

2*c*	4
W	20
L	40
No. Nodes	80,872
No. Elements	17,632
No. CF Nodes	133

2*c*	2.67
W	13.33
L	26.66
No. Nodes	49,174
No. Elements	10,568
No. CF Nodes	91

2*c*	2
W	10
L	20
No. Nodes	43,330
No. Elements	9,324
No. CF Nodes	91

2*c*	1.6
W	8
L	16
No. Nodes	29,428
No. Elements	6,236
No. CF Nodes	49

Figure 4. Geometric space.

a/c combination in figure 4, the smaller, upper illustration is a sketch of the crack plane cross section drawn in proportion to the other geometries. (The illustrations for $a/c=0.2$, $a/B=0.6$, and $a/c=0.2$, $a/B=0.8$ are half-symmetry drawings to allow space for the proportional sketches.) These sketches allow the reader to visualize the difference in overall cross section size for each geometry. For each a/B and a/c combination in figure 4, the lower illustration is a close-up view of the crack plane cross section with the thickness held constant for all geometries. The close-up sketches allow one to better see the semielliptical crack shape in relation to the specimen thickness. For all of the geometries, $B=1$ and $L/W=2$. Figure 4 lists the $2c$, W, and L values for all the geometries. The plate widths were set equal to the greater of $W=5*2c$ or $W=5*B$ to minimize width effects on the J-integral solutions and to ensure that the plates maintained a 'plate like' width-to-thickness aspect ratio for small cracks. Utilizing these minimum width criteria precludes the need to include the $W/2c$ ratio as a third variable in the geometric space. The rationale for the width criteria is discussed in appendix A.

2.3 Finite Element Models

A total of 600 nonlinear finite element analyses were required to perform the analysis of the 30 material and 20 geometric combinations. All of the finite element models were created using the commercial finite element mesh creation and post-processing tool, FEACrack,[1] and the analyses were performed using the freely available research code, WARP3D version 16.3.1.[18]

2.3.1 Finite Element Model Details

All of the surface cracked plates are modeled with 3D quarter-symmetric FEMs using 20-node reduced integration isoparametric elements (element type q3disop in WARP3D). A typical FEM mesh is shown in figure 5. The number of elements range from 4,520 to 26,928, and the number of nodes vary from 21,332 to 122,396 as listed in figure 4. The crack fronts are surrounded with ten rings of elements forming the domains for calculation of the *J*-integral. The innermost ring of elements incident on the crack front contains 20-node hexahedrons collapsed into wedges with initially coincident nodes along the crack front left unconstrained to permit blunting deformations. The number of nodes in the ϕ direction along the crack front varies from 49 to 217 as listed in figure 4 (CF nodes). The *J*-integral is evaluated numerically using the domain integral method as implemented in WARP3D over each of the ten concentric element domains at each crack front node location. The result at the outermost domain (domain 10) is used for the *J*-integral values in this study, and the domain convergence is discussed later in section 3. The reported *CMOD* values are the displacements of the node on the crack mouth on the outer surface centerline of the plate as shown in figure 5.

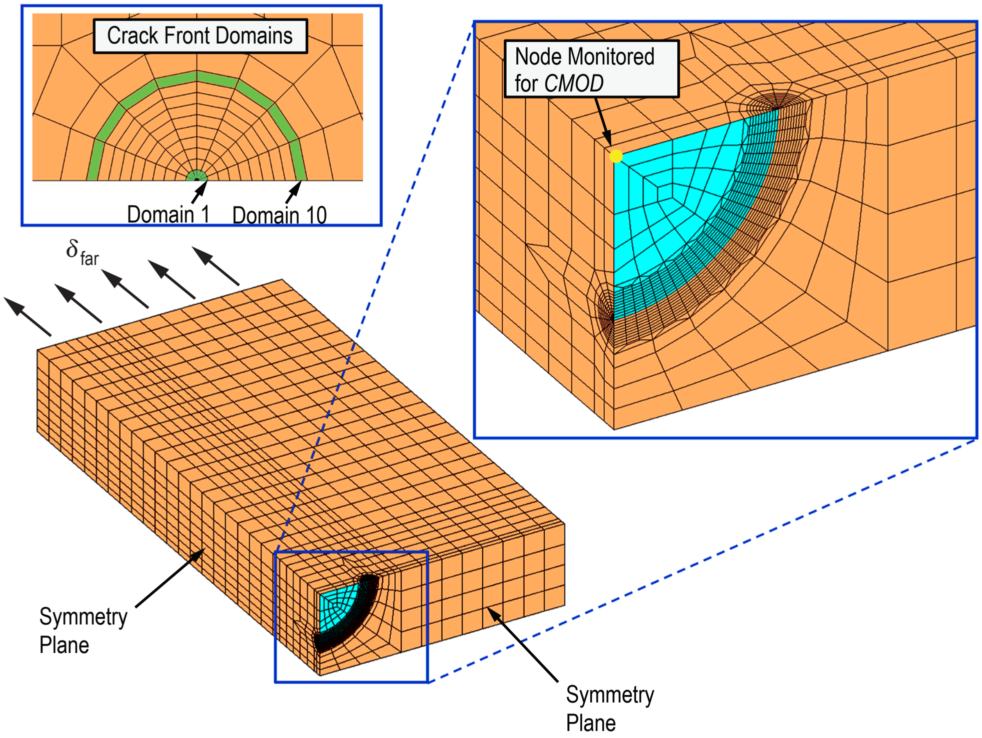

Figure 5. Typical ¼ symmetric surface crack finite element mesh.

2.3.2 Boundary Conditions and Loading

The FEMs are loaded with 20 to 30 uniform load steps with an average of 2 to 5 Newton iterations for convergence within each step to a tight tolerance on residual nodal forces. Symmetry planes are enforced through setting the normal nodal displacements on the plane equal to zero. Uniform axial displacements, δ_{far}, are applied to all of the nodes on the top surface of the plate to apply tension. The intent was to apply sufficient displacement to deform the models far into an elastic-plastic regime, but not so much that the models would fail to converge on the last analysis step. Since hundreds of nonlinear models were run, it was not practical to 'hand pick' a unique value for each displacement boundary condition—an automated method had to be employed.

The δ_{far} boundary conditions for the FEMs are applied in a two-step process. First, the LPPL equation is used to calculate the net section stress, σ_{net}, corresponding to $\varepsilon_{pl}=0.1\%$. This stress is then used to calculate a linear approximation of the far-field displacement using the equation

$$\delta_{\text{far}} = \frac{\sigma_{\text{net}} L}{2E} \quad , \tag{2}$$

where the factor of ½ is due to symmetry. All of the FEMs were successfully run with the δ_{far} values from equation (2) applied, and the models were checked for the deformation level, M, where M is defined as

$$M = \frac{r_\phi \sigma_{ys}}{J_\phi} \quad . \tag{3}$$

In equation (3) J_ϕ is the J-integral value at a given parametric crack front angle, ϕ, and r_ϕ is the characteristic length for a given ϕ. For the surface crack problem, two characteristic lengths at any ϕ location are defined as $r_{\phi a}$ and $r_{\phi b}$ as shown in figure 6. Considering a 2D slice through the specimen along a path defined by $r_{\phi a}$ and $r_{\phi b}$, then $r_{\phi a}$ is analogous to a crack length measurement and $r_{\phi b}$ relates to a remaining ligament measurement.

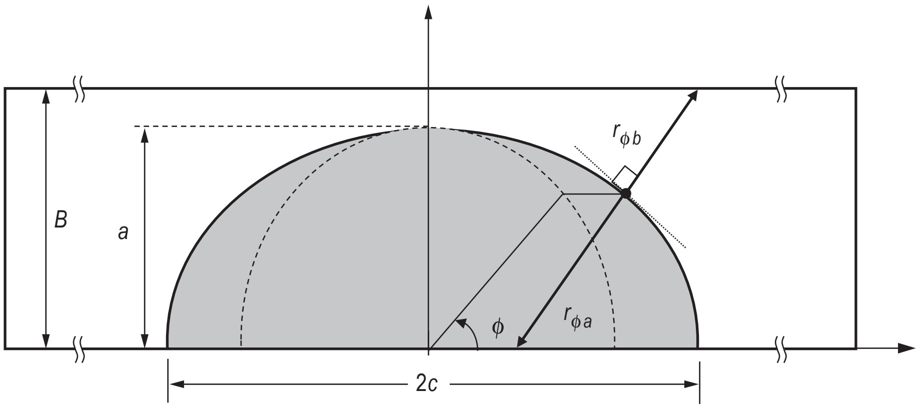

Figure 6. Cross section through the crack plane illustrating the characteristic lengths, $r_{\phi a}$ and $r_{\phi b}$.

The authors desired that $M \approx 20$ or less at the final load step (note that M decreases as deformation increases). The M-values were checked at $\phi = 30°$ and $\phi = 90°$ for both $r_{\phi a}$ and $r_{\phi b}$ for all FEMs. For the next step in refining the δ_{far} boundary condition, the FEMs that did not reach the desired deformation level are identified, and their M and δ_{far} data are used to predict a new δ_{far} required to reach $M \approx 20$. The method for predicting the new δ_{far} is illustrated for one of the FEMs ($a/B = 0.4$, $a/c = 0.6$, $n = 6$, and $E/\sigma_{ys} = 500$) in figure 7 wherein $\log_{10}(M)$ is plotted against the normalized far-field displacements, $2\delta_{\mathrm{far}}/L$, at $\phi = 30°$ and $\phi = 90°$ for both $r_{\phi a}$ and $r_{\phi b}$. In figure 7, deformation increases from right to left in the plot. A straight line is fit to the last three data points in the result set, and the δ_{far} required to reach $M = 20$ is estimated for each location from the linear prediction. The minimum estimated δ_{far} for each model was applied as a new boundary condition, and this subset of FEMs was reanalyzed. The final set of solutions was then collected into a Matlab[19] data structure for use in the interpolation routines.

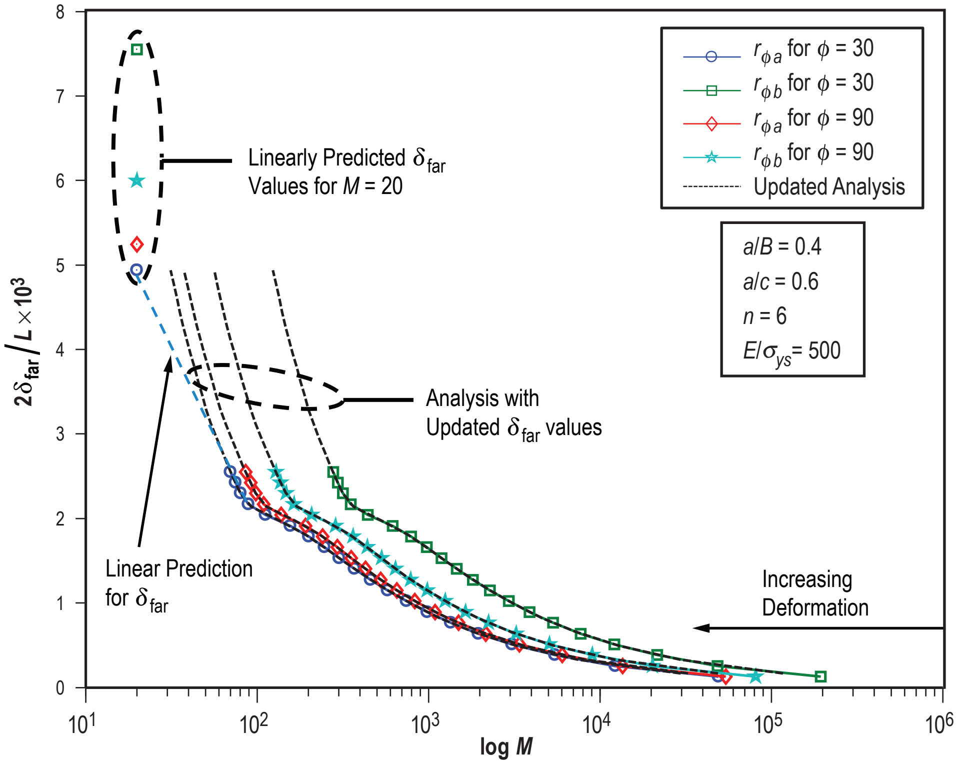

Figure 7. Method to choose far-field displacement values for FEMs based on a desired deformation level, M.

2.4 Automation Methods

Handling this large array of nonlinear models was made practical by computer routines that automate the process of building the FEMs, running the nonlinear analyses, post-processing model results, and organizing the solution results into multidimensional arrays. Computer routines were written in Matlab to create the file storage directory structure and serve as the overall controller for the model building, execution, and post-processing procedure.

The FEMs were built using FEACrack in batch control mode on a 64-bit Windows XP computer. FEACrack uses a text-based input file to control all the model parameters for a given FEM. The authors developed Matlab scripts that read in a 'baseline' FEACrack input file for a surface crack plate and modified the file to include the desired plate dimensions, crack dimensions, material properties, and boundary conditions. The script then executes FEACrack in batch mode to build the appropriate input file for WARP3D and saves the file with an appropriate filename in the desired directory. This process was automated to prepare the required 600 input files for analysis. The WARP3D input files were then moved to a 64-bit Linux server for efficient parallel processing analysis. Once the FEAs were complete, the WARP3D binary packet result files were transferred to the 64-bit Windows XP computer and were post-processed in batch mode with FEACrack using another set of Matlab generated scripts. These post-processing steps resulted in a set of 600 text-based result files from FEACrack that contained all of the pertinent model result data. A set of Matlab scripts were then used to consolidate the full data set into arrays of J-integral versus ϕ values, far-field stresses, and $CMOD$ values in an easily indexed Matlab data structure.

2.5 Interpolation Methodology

The interpolation methods developed and implemented in this study involve a normalization scheme used to scale the solutions. This scheme is described below along with a brief exemplar case study. The interpolation process takes place in this dimensionless, normalized space. The interpolation methods are described on a step-by-step basis.

2.5.1 Normalization Scheme

To derive useful results from the solution space, interpolation within the geometry and material dimensions is necessary, but scaling of the solutions with respect to geometry and material is also required. To simplify scaling of the solution space, it is advantageous, but not required, to have the solution space normalized to a dimensionless state. In this fashion, once interpolation is complete within the space, the resulting dimensionless interpolated solution can be easily scaled by to a dimensioned state by multiplying by representative length and stress scaling factors for the actual geometry. There are three primary results in the solution set that need to be normalized: J, $CMOD$, and far-field stress, σ. By dimensional analysis, it is clear that the J-integral is conveniently normalized by a product of stress and length, therefore the normalized J-integral value, J_n, can be written as

$$J_n = \frac{J}{\sigma_{ys} B} \quad . \tag{4}$$

In this case, the normalizing stress is chosen to be the material yield strength (proportional limit) represented in the LPPL stress-strain curve model, and the normalizing length is chosen to be the plate thickness, B. These are particularly convenient normalizing factors because, as discussed previously, both σ_{ys} and B were defined to have unit value in the model space. Thus, the J-integral value from the analysis does not change when normalized. The same follows for the $CMOD$ and far-field stress results where

$$CMOD_n = \frac{CMOD}{B} \quad , \tag{5}$$

and the normalized far-field stress, σ_n, is

$$\sigma_n = \frac{\sigma}{\sigma_{ys}} \quad . \tag{6}$$

Starting from this normalized space, a dimensional result is easily obtained by reversing the normalization by multiplying by the appropriate dimensional factors, B_D and σ_{ysD}, the thickness and yield strength, respectively, of the actual specimen or structure. Letting J_D, $CMOD_D$, and σ_D represent the dimensional results;

$$J_D = J_n * \sigma_{ysD} * B_D \quad , \tag{7}$$

$$CMOD_D = CMOD_n * B_D \quad , \tag{8}$$

and

$$\sigma_D = \sigma_n * \sigma_{ysD} \quad . \tag{9}$$

The dimensional force, P_D, associated with the far stress, σ_D, can be obtained by simple mechanics following similar form:

$$P_D = \sigma_n * W_D * B_D \quad , \tag{10}$$

where W_D is the dimensional width of the plate.

2.5.2 Normalization Case Study

To illustrate the ability to scale nonlinear surface crack solutions across proportional geometry changes and differing yield strength values, two surface crack FEMs were analyzed. The first, model 1, resides near the center of the geometric and material dimensions of the solution space: $a/B=0.6$, $a/c=0.6$, $n=6$, $E/\sigma_{ys}=300$ with $\nu=0.3$. The normalizing dimensional factors for model 1 are also set to render a ‘normalized’ solution: $\sigma_{ys}=1$, $B=1$. As was the case for other models in the space, W is set to $5\times 2c$, so $W=10$, and $L=2\times W$, so $L=20$.

The second model, model 2, has a proportional geometric scale three times model 1 ($B=3$, $2c=6$, $W=30$, $L=60$). The material properties for model 2 (E/σ_{ys}, ν, n) are also identical to model 1 with the exception of $\sigma_{ys}=50$. Note that since $E/\sigma_{ys}=300$, the modulus in model 2 is also scaled with σ_{ys}. Any choice of consistent units may be assumed, and the authors chose the SI units (mm for length and MPa for stress) for this example. Figure 8 shows a half-symmetric sketch of the two models drawn in proportion to one another. Model 2 was run in displacement control to three times the far-field displacement, δ_{far}, of model 1. The model 1 results were then scaled using equations (7)–(10) with $\sigma_{ysD}=50$, B_D=3, and $W_D=30$ to predict the model 2 result. Model 2 and

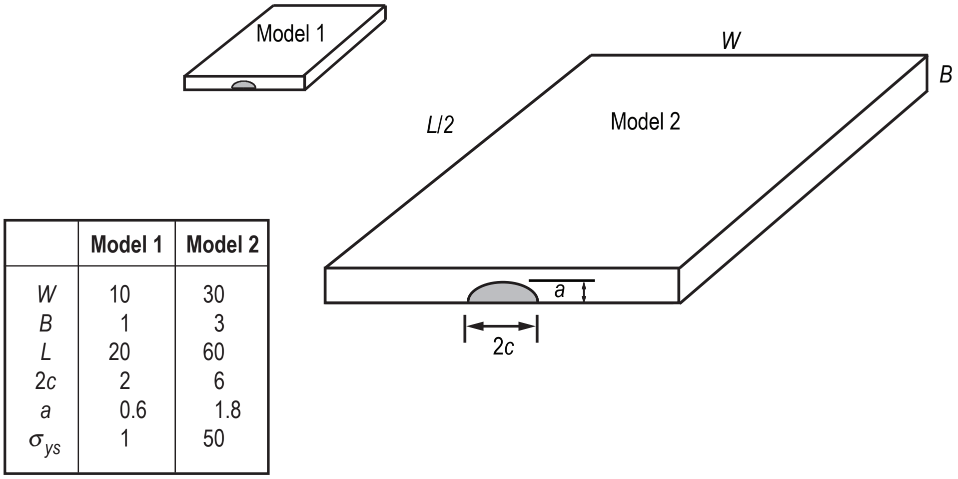

	Model 1	Model 2
W	10	30
B	1	3
L	20	60
$2c$	2	6
a	0.6	1.8
σ_{ys}	1	50

Figure 8. Cross section through the crack plane for two surface crack geometries with different physical dimensions but the same geometric proportions.

scaled model 1 results for P versus $CMOD$, J_{total}, and J_{el} (linear-elastic portion of J_{total}) versus $CMOD$, and J_{total} and J_{el} versus ϕ at the last load step are compared in figures 9–11 illustrating perfect agreement for each variable.

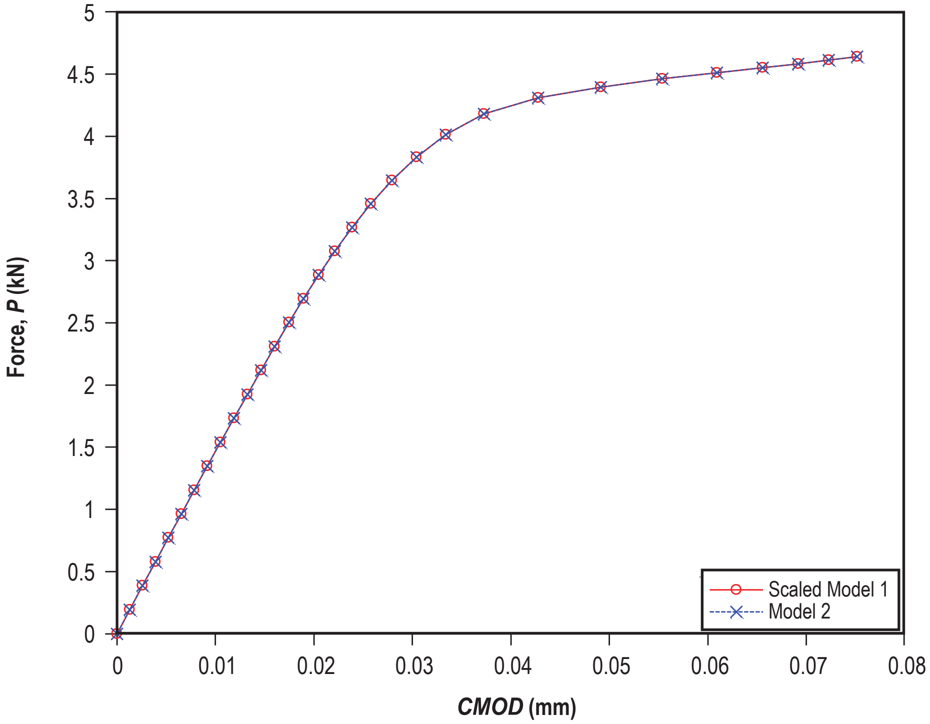

Figure 9. Comparison of the force versus $CMOD$ response for models 1 and 2.

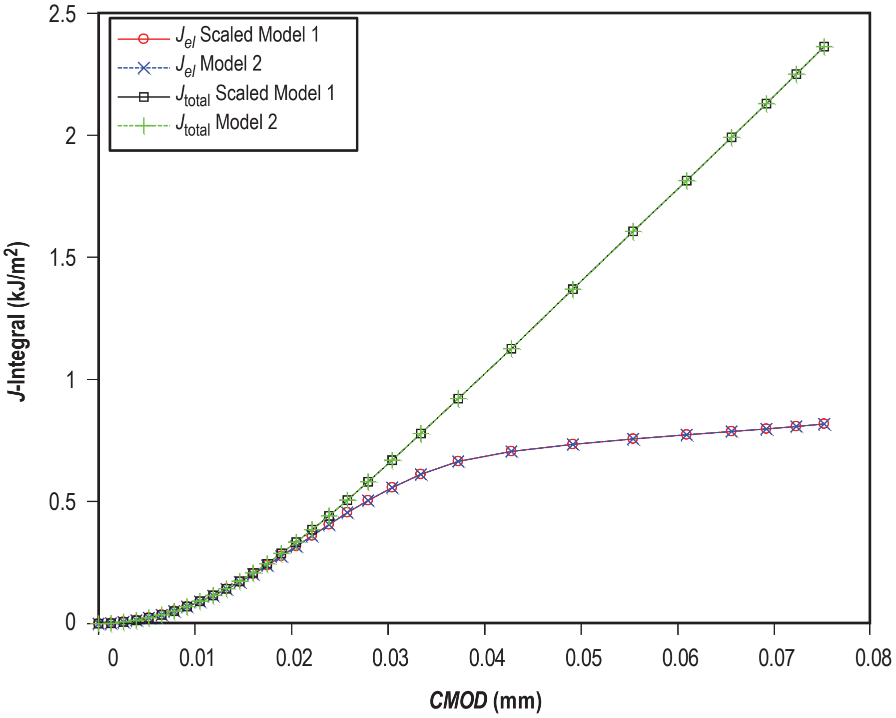

Figure 10. Comparison of J_{total} and J_{el} versus $CMOD$ for models 1 and 2.

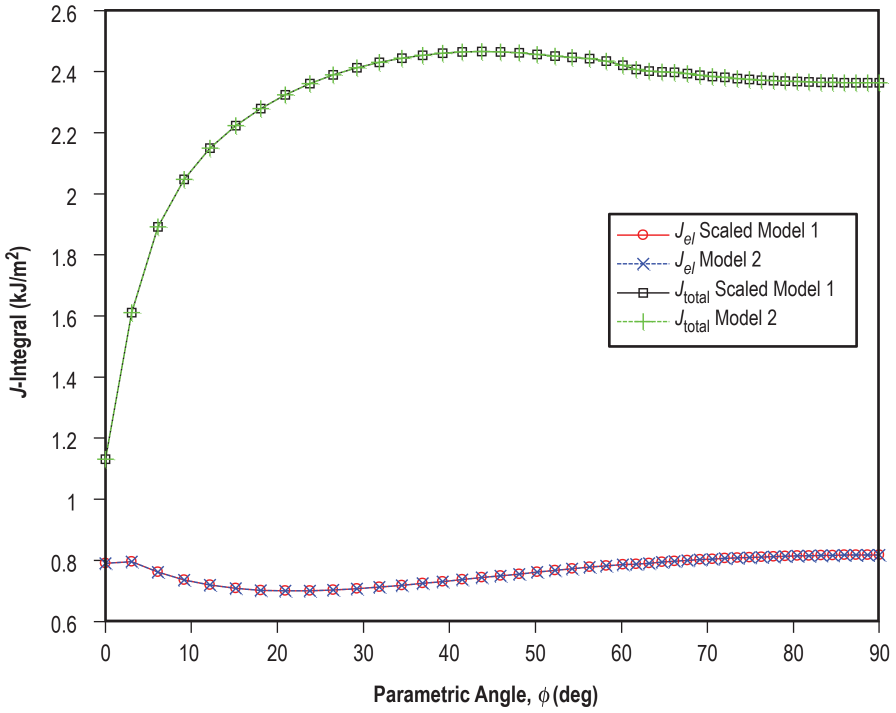

Figure 11. Comparison of J_{total} and J_{el} versus ϕ for models 1 and 2.

2.6 Solution Space Interpolation

Having established the basis for the nondimensional solution space and procedures for scaling proportional geometry and material yield strength to dimensioned values, consideration turns to interpolation within the space, which provides an estimated solution at any crack shape and depth within the geometric space and at any modulus of elasticity and strain hardening exponent within the material space. The quantity of interest is the J_n value as a function of ϕ around the crack perimeter, $J_n(\phi)$. For each of the 600 models in the space, $J_n(\phi)$ is calculated as a function of increasing load. The state of the load can be described by either the models' far-field stress, σ_n, or displacement at the crack mouth, $CMOD_n$. Though σ_n (or force) is an intuitive descriptor of the load, for elastic-plastic analysis, the $CMOD$ is a more reliable predictor of J (J is nearly a linear function of $CMOD$ in the plastic regime);[7,17,20] so the authors chose to use $CMOD$ as the quantifier of the loading condition in the interpolation methodology. Figure 12 shows a plot of $J_n(\phi)$ versus $CMOD_n$ for a solution with 30 load increments. Open symbols are placed at the $\phi = 30°$ location to help visualize the J_n versus $CMOD$ trajectory for a given ϕ location. In the solution space, the relationship between σ_n and $CMOD_n$ is maintained, thus by dividing σ_n by the final dimensioned area, a prediction of the P versus $CMOD$ trace is available. This trace is particularly useful for interpretation of experimental surface crack test results.

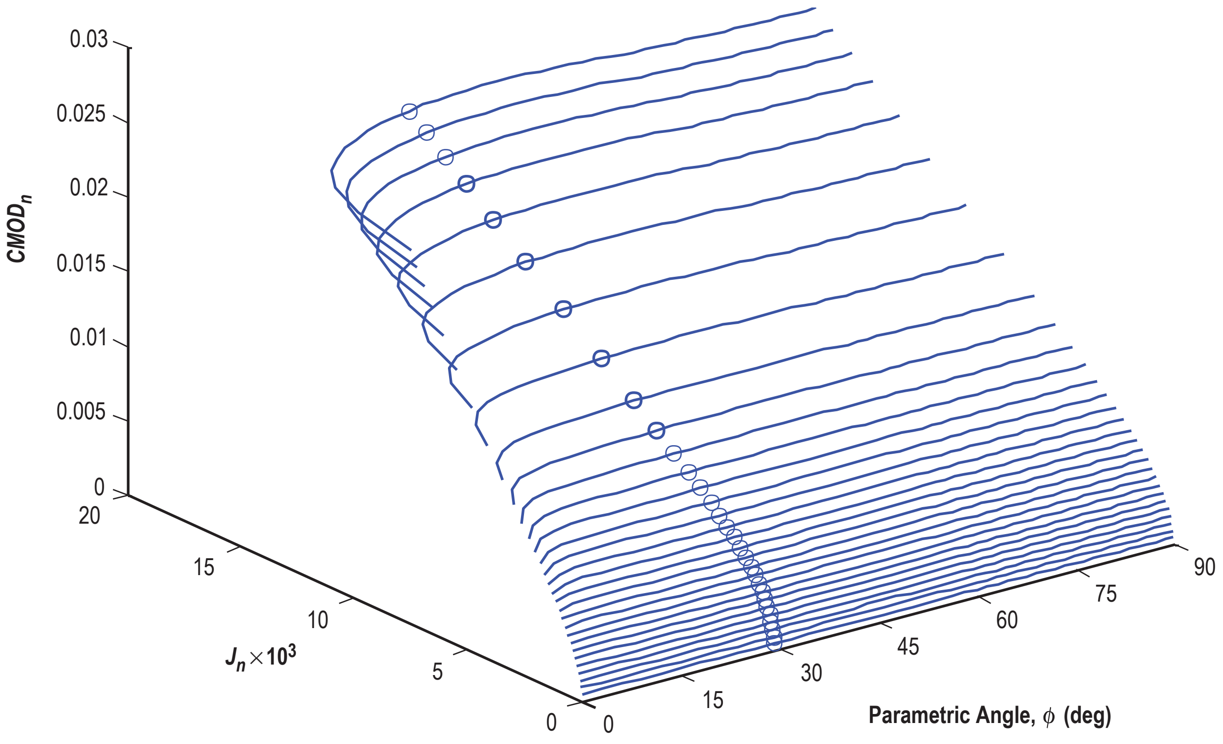

Figure 12. $J(\phi)$ versus $CMOD_n$ space.

The solution space consists of 600 result data sets, each containing $J_n(\phi)$ versus $CMOD_n$ and σ_n versus $CMOD_n$ data. The space is structured in a four-dimensional array that is most easily visualized by considering a 4×5 geometry matrix with four rows of a/B ratios and five columns of a/c ratios. Within each of the 20 geometric combinations, there exist 30 material solutions described by a 5×6 matrix of material solutions, five values of n and six values of E/σ_{ys}. The solution space is readily indexed by these four dimensions. For a given model result, R, the solution is given by the notation: $R(a/B, a/c, n, E/\sigma_{ys})$. Figure 13 shows a conceptual illustration of the $R(a/B, a/c, n, E/\sigma_{ys})$ solution space with the geometric space at the highest level and the entire material space existing at the next level repeated within each geometric combination followed by the $J_n(\phi)$ versus $CMOD_n$ and σ_n versus $CMOD_n$ data for each of the 600 models at the lowest level.

In general, the actual surface crack geometry and material of interest will not fall directly on an existing solution and interpolation is necessary. To interpolate to a new solution, $\bar{R}\left(a/B,\ a/c,\ n,\ E/\sigma_{ys}\right)$,the first step is to identify the subset of the 600 model space that will be active in the interpolation process by determining the location of $\bar{R}$ in the geometry and material matrices. For illustration, consider a choice of $\bar{R}\left(a/B = 0.5, a/c = 0.5, n = 8, E/\sigma_{ys} = 400\right)$ that is located between the cells labeled g_1–g_4 in the geometry matrix of figure 13. The four 'nearest neighbor' subset solutions are the geometry combinations designated as g_1–g_4. For each of the g_1–g_4 geometries, a point for $\bar{R}$ can be placed in the material matrix resulting in materials m_1–m_4. Identifying the sets g_1–g_4 and their associated m_1–m_4 sets provides the 16 nearest neighbor data sets for use in the interpolation of the $\bar{R}$ solution.

The 16 subsets represent different geometry and material combinations, so there is no expectation that the data sets will have the same nodal ϕ spacing, number of load increments, spacing of load increments, or final deformation values. Therefore, to simplify the interpolation process, the ϕ locations and load increments are adjusted to be uniform across the 16 subset solutions. Even spacing in ϕ is easily created by linear interpolation of the existing $J_n(\phi)$ data at standard ϕ locations for each load increment in every model. In this study, the J_n values are calculated in 2° increments for $0° \leq \phi \leq 90°$ for a total of 46 $J_n(\phi)$ values at each load increment.

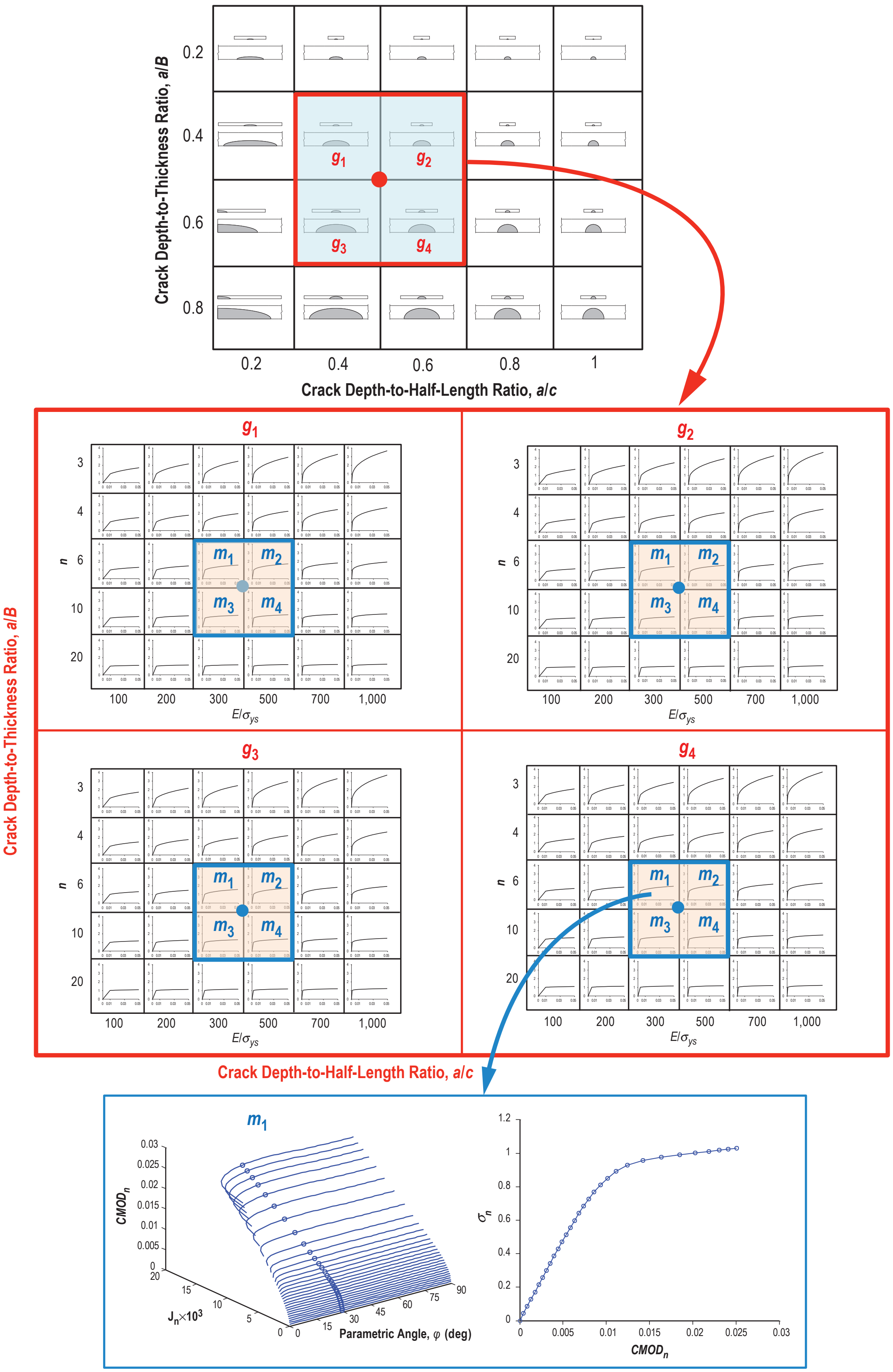

Figure 13. Conceptual illustration of the interpolation space.

The methodology for setting uniform spacing and magnitude for loading conditions across the 16 subset solutions is not as straightforward. Since the FEMs are run to different levels of σ_n and $CMOD_n$, several choices must be made concerning how to divide the solutions into load increments including: the measure used for parsing (σ_n or $CMOD_n$), the load increment spacing, and a method to either truncate or extend the solutions. As stated above, the authors chose to use $CMOD_n$ as the parsing measure of loading condition, thus a common maximum value of $CMOD_n$ across all 16 sets is needed. Figure 14(a) plots σ_n versus $CMOD_n$ for the 16 subset solutions and illustrates the challenge in determining the maximum allowed $CMOD_n$ value for the solution set. The minimum, maximum, and average $CMOD_n$ values are designated by vertical lines in figure 14(a). Truncating all of the data sets to the minimum $CMOD_n$ of the 16 sets severely limits the extent of the solutions. In turn, extrapolating all of the data sets out to the maximum $CMOD_n$ value requires extending some solutions to $CMOD_n$ values far beyond their final converged load increment. Instead, the authors chose to set the maximum common loading condition equal to the average $CMOD_n$ of the 16 data sets. Solutions that extend beyond the average $CMOD_n$ are truncated. Solutions with maximum $CMOD_n$ values less than the average are extrapolated out to the average $CMOD_n$ by fitting a power law of the form $\sigma_n = \alpha * (CMOD_n)^{\beta} + \gamma$ to the last five σ_n versus $CMOD_n$ data points in the set, where α, β, and γ are fitting constants. Once the 16 data sets have all been either truncated or extrapolated to the same maximum $CMOD_n$, each set is divided into 20 even $CMOD_n$ increments common across all sets. Linear interpolation is used to determine the values of σ_n for the 20 $CMOD_n$ increments. Figure 14(b) illustrates the 16 σ_n versus $CMOD_n$ data sets with 20 even $CMOD_n$ increments out to the average $CMOD_n$.

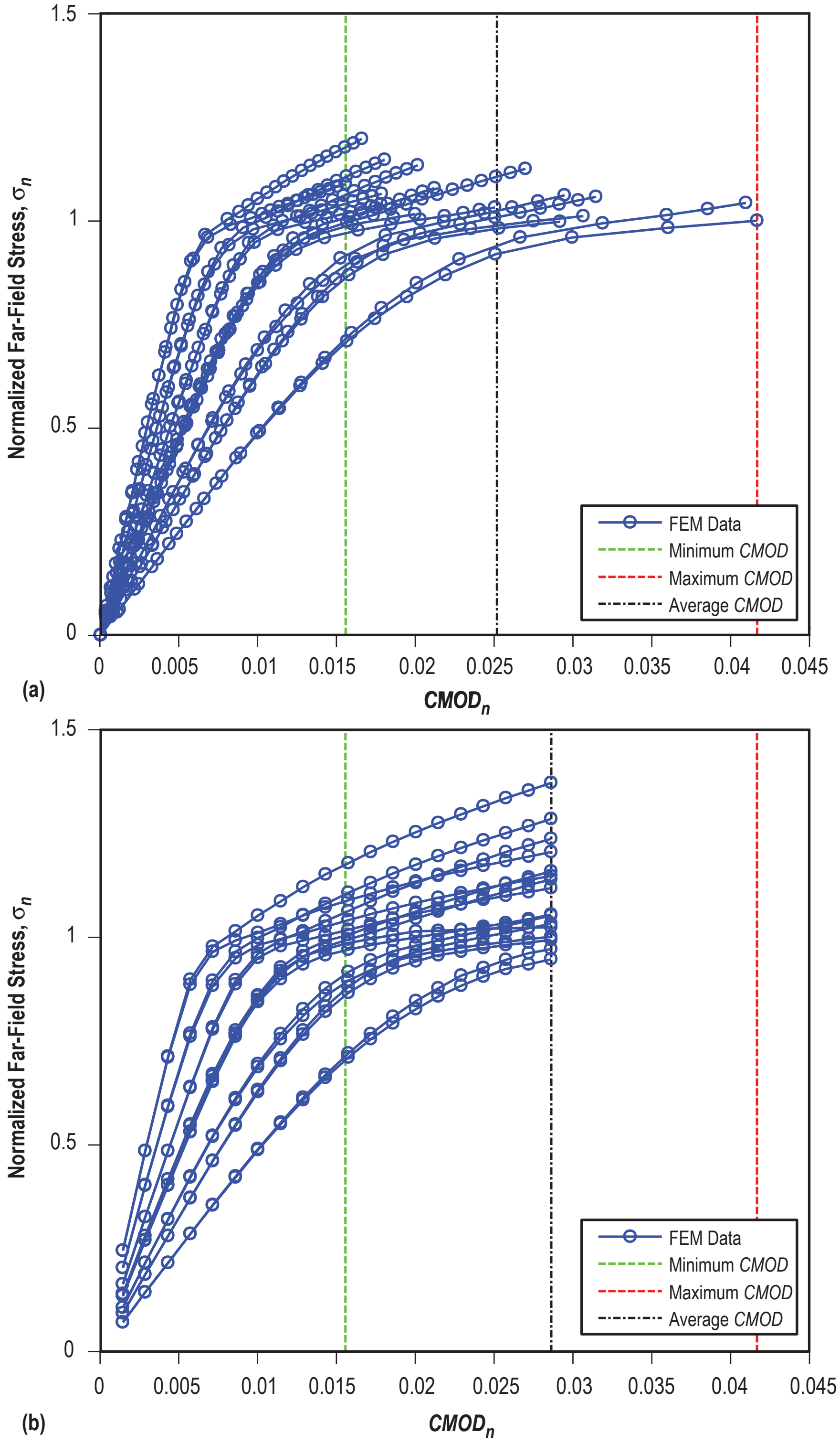

Figure 14. Illustration of (a) effect of truncating the solution space based on the average of the maximum $CMOD_n$ values on the σ_n versus $CMOD_n$ results, and (b) dividing the $CMOD_n$ into even increments for σ_n versus $CMOD_n$ interpolation.

With each of the 16 subset solutions adjusted to common increments of $CMOD_n$, the $J_n(\phi)$ values for the new load increments must be interpolated. Figure 15(a) shows $J_n(\phi = 90°)$ versus $CMOD_n$ for the same 16 subsets shown in figure 14. The J_n versus $CMOD_n$ solutions that extended beyond the average $CMOD_n$ are truncated while the solutions that are less than the average $CMOD_n$ are extrapolated using linear extrapolation. Linear extrapolation works well for these data because the J_n versus $CMOD_n$ response becomes approximately linear once into the elastic-plastic regime. Figure 15(b) illustrates $J_n(\phi = 90°)$ versus $CMOD_n$ data sets with 20 even $CMOD_n$ increments out to the average $CMOD_n$.

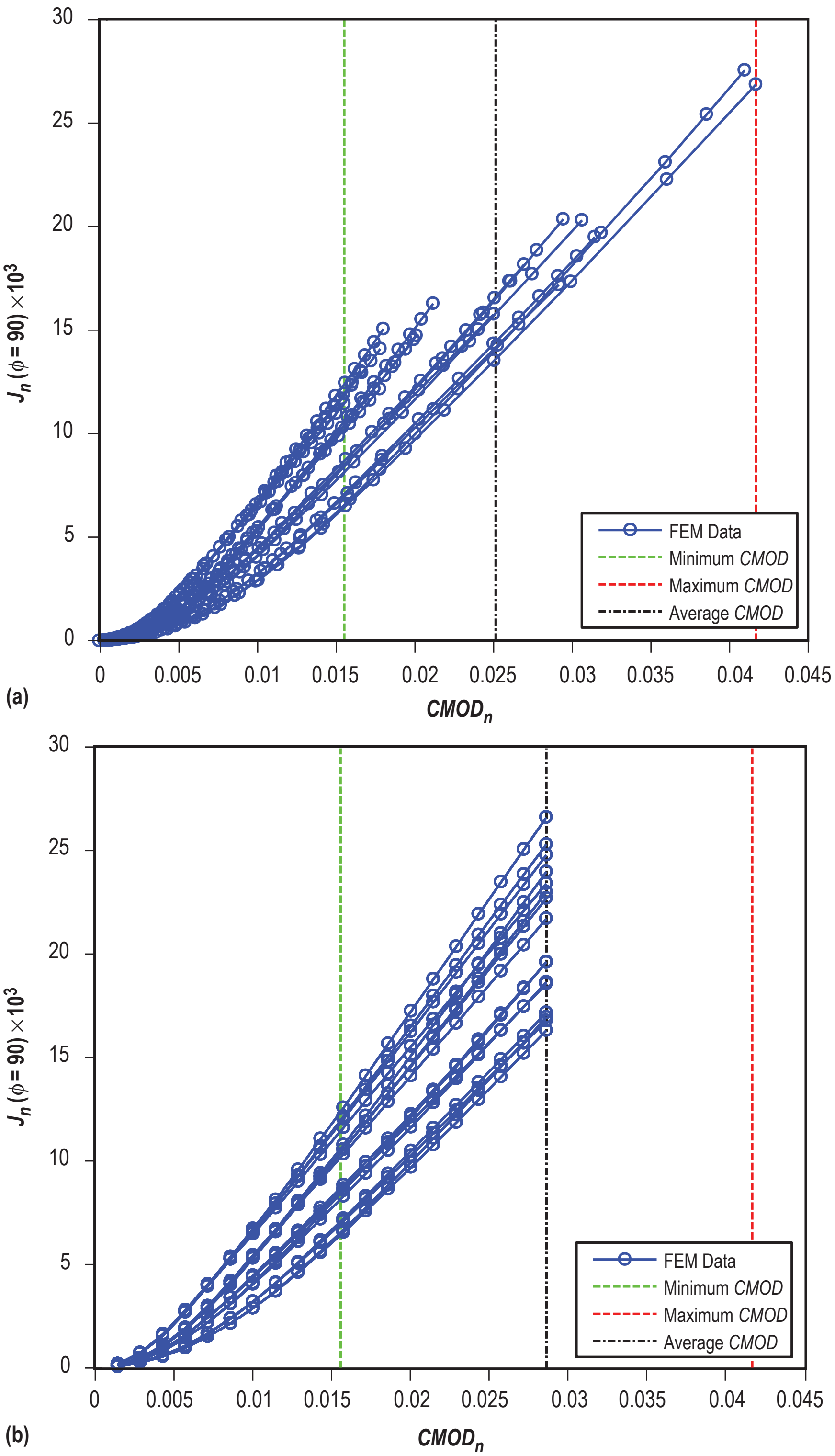

Figure 15. Illustration of (a) effect of truncating the solution space based on the average of the maximum $CMOD_n$ values on the J_n versus $CMOD_n$ results, and (b) dividing the $CMOD_n$ into even increments for J_n versus $CMOD_n$ interpolation.

Once the 16 subset solutions are prepared with even ϕ spacing and load increments, the step-by-step interpolation process to the final $\bar{R}$ can proceed. Figure 16 illustrates the four-step interpolation process used by the authors. Each of the steps are indicated by the Roman numerals I through IV. At each interpolation step I through IV, J_n is interpolated at each ϕ location for each $CMOD_n$ increment to determine a new $J_n(\phi)$ versus $CMOD_n$. A second interpolation process evaluates σ_n for each $CMOD_n$ increment. Step I in the interpolation process begins with the 16 prepared subset solutions for linear interpolation based on crack shape ratio, a/c. Within the 16 solutions, there are eight pairs of solutions that differ only by a/c. Linear interpolation occurs between these pairs based on the target a/c value, resulting in eight new solutions, all with the same a/c value but different combinations of a/B, n, and E/σ_{ys}. In step II, linear interpolation is performed on the four pairs of solutions that differ only by crack depth, a/B, to the chosen a/B value for $\bar{R}$. This results in four new solutions with the same geometric values but different material values. In step III, two pairs of solutions are linearly interpolated in terms of n to the chosen n value for $\bar{R}$ resulting in two new solutions differing only in their E/σ_{ys} values. Finally, in step IV, the remaining two solutions are interpolated to the chosen E/σ_{ys}, resulting in the final $\bar{R}$ interpolated solution. As will be shown in section 3, the $J_n(\phi)$ and σ_n values have nonlinear spacing with E/σ_{ys}; therefore, for the step IV interpolation, linear interpolation was performed in terms of $\log_{10}(E/\sigma_{ys})$ and the $\log_{10}$ of the chosen E/σ_{ys} for $\bar{R}$ value.

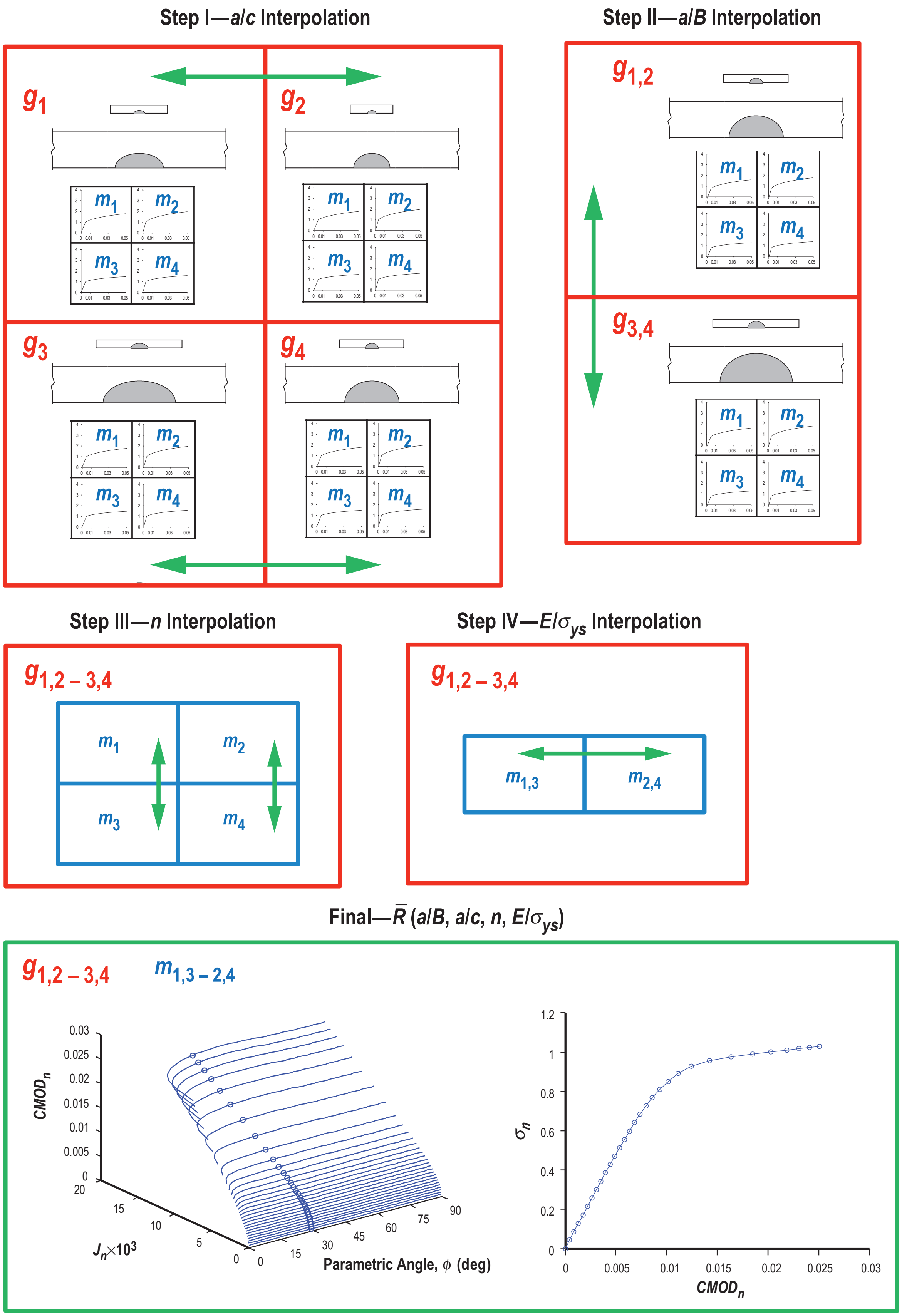

Figure 16. Conceptual illustration of the interpolation process. Arrow indicates interpolation direction.

Figures 17–20 illustrate the interpolation steps I through IV, respectively, for the example interpolated solution, $\bar{R}\left(a/B, a/c, n, E/\sigma_{ys}\right) = \bar{R}(0.5, 0.5, 8, 400)$. Each figure shows a comparison of results for: (1) σ_n versus $CMOD_n$, (2) $J_n(\phi = 90°)$ versus $CMOD_n$, and (3) $J_n(\phi)$ for the final common loading condition of the nearest neighbor solution subsets along with the final interpolated result, $\bar{R}$. The solution subset results are plotted as solid lines with open symbols; the open symbols represent specific materials (m_1–m_4 in figs. 13 and 16) while the colors represent specific geometry choices (g_1–g_4 in figs. 13 and 16). The final interpolated results are plotted with a solid line with filled star-shaped symbols. Figure 17 represents the original 16 subsets prior to step I interpolation process on a/c. Figure 18 shows the resulting eight solutions of step I prior to the step II interpolation for a/B. Figure 19 shows the resulting four solutions of step II prior to step III interpolation on the n value. Lastly, figure 20 shows the final two solutions to be interpolated by E/σ_{ys} in step IV.

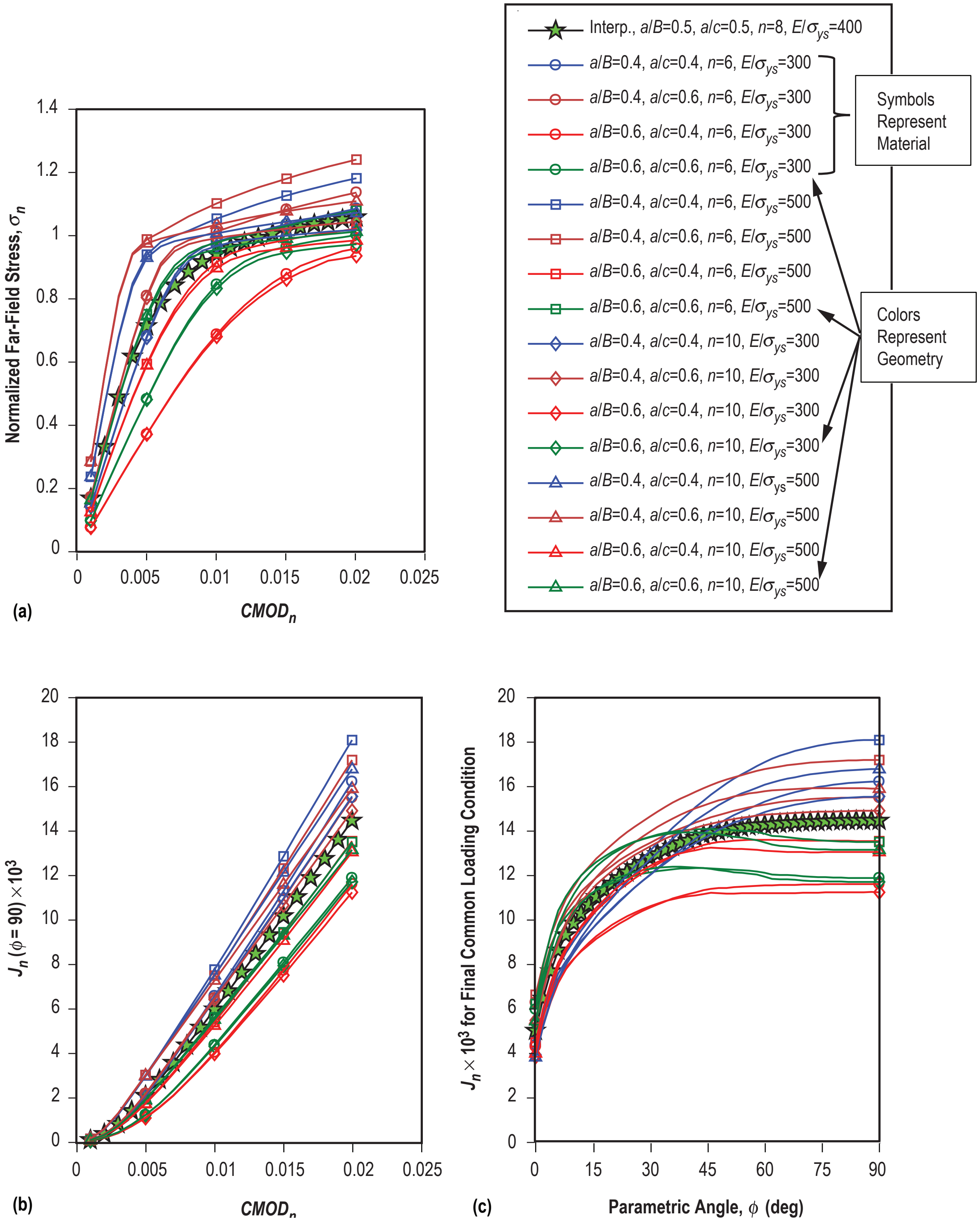

Figure 17. Comparison of results for (a) σ_n versus $CMOD_n$, (b) $J_n(\phi = 90°)$ versus $CMOD_n$, and (c) J_n versus ϕ for the final common loading condition for the 16 solution subsets and the final interpolated result prior to interpolation step I to the desired a/c value.

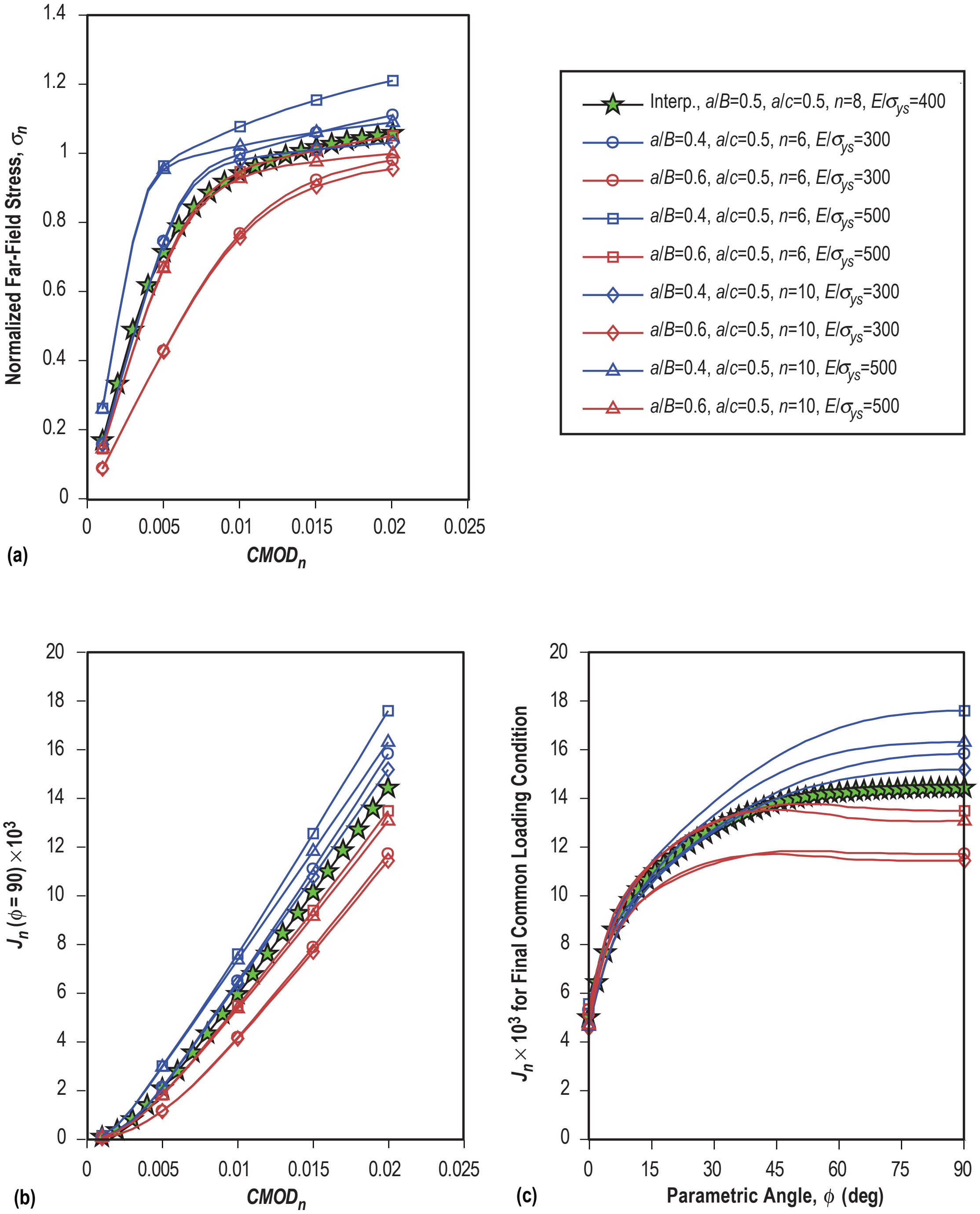

Figure 18. Comparison of results for (a) σ_n versus $CMOD_n$, (b) $J_n(\phi = 90°)$ versus $CMOD_n$, and (c) J_n versus ϕ for the final common loading condition for the eight solution subsets and the final interpolated result prior to interpolation step II to the desired a/B value.

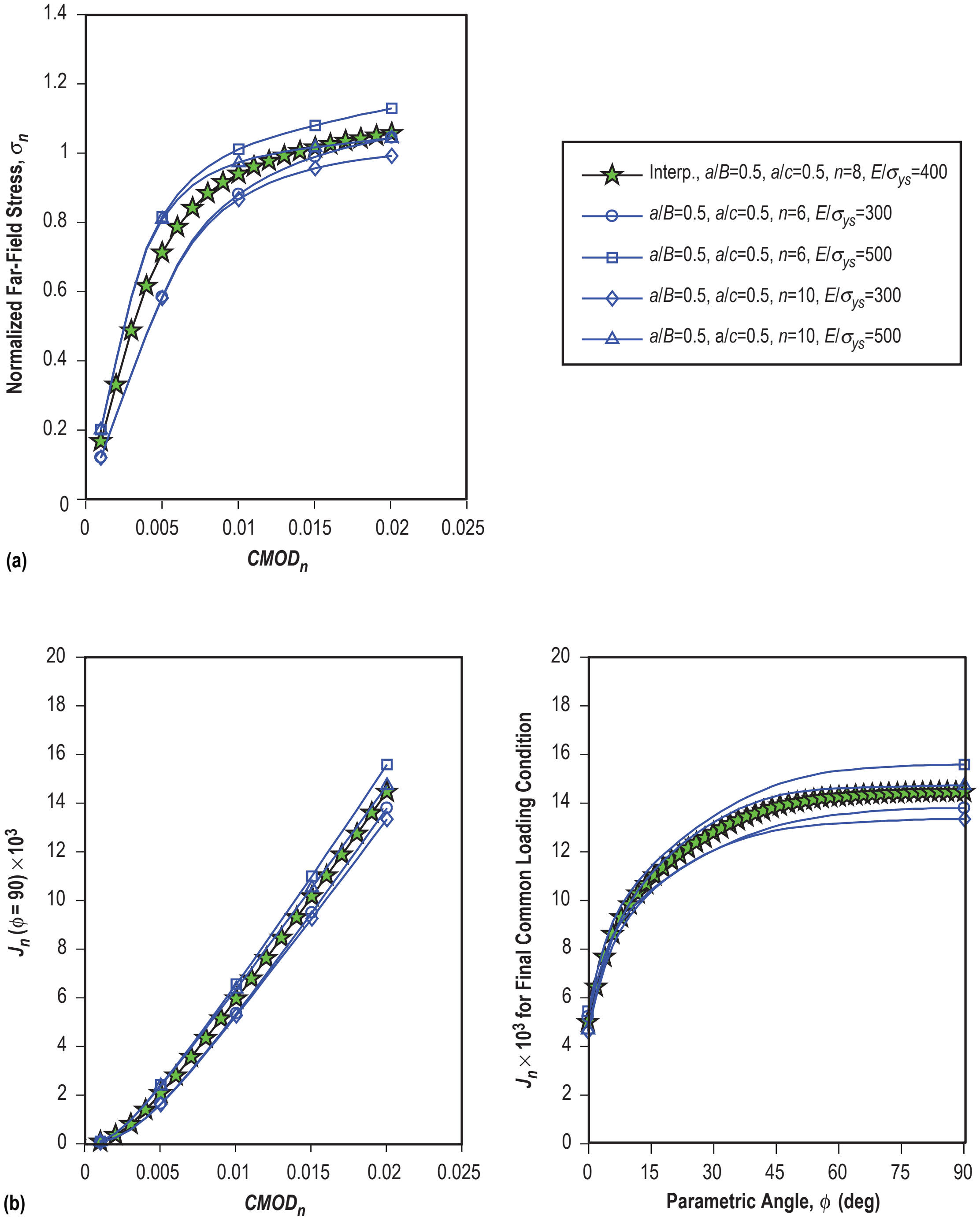

Figure 19. Comparison of results for (a) σ_n versus $CMOD_n$, (b) $J_n(\phi = 90°)$ versus $CMOD_n$, and (c) J_n versus ϕ for the final common loading condition for the four solution subsets and the final interpolated result prior to interpolation step III to the desired n value.

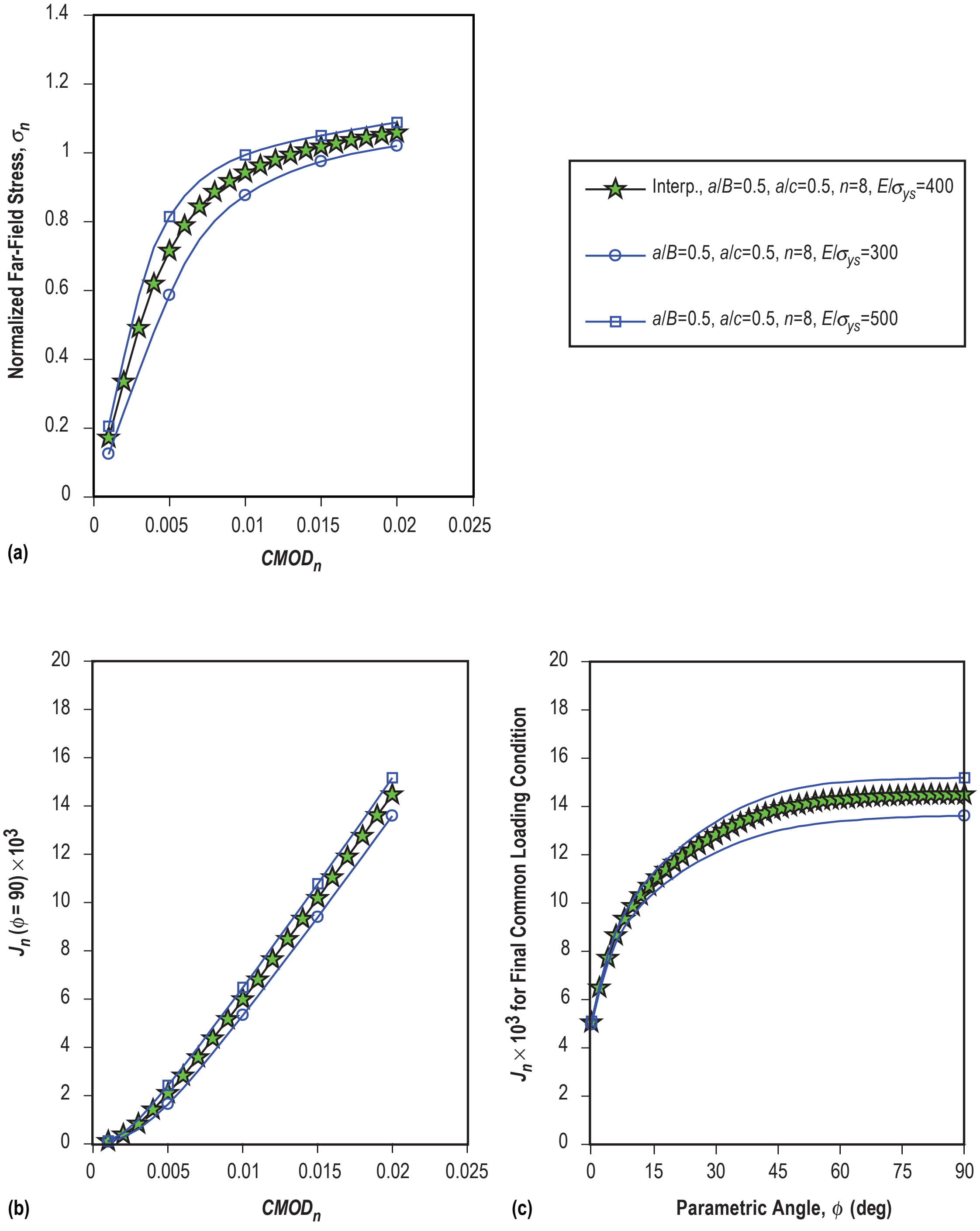

Figure 20. Comparison of results for (a) σ_n versus $CMOD_n$, (b) $J_n(\phi = 90°)$ versus $CMOD_n$, and (c) J_n versus ϕ for the final common loading condition for the two solution subsets and the final interpolated result prior to interpolation step IV to the desired E/σ_{ys} value.

3. REVIEW AND VERIFICATION

The solution space described herein is too broad for detailed review; however, a brief parametric review of the space is warranted to convey to the reader the influence of the four parameters of the space. Following this brief review, the authors present the results of the verification process used to ensure the reliability of the solution space and the interpolation routines. The verification process also serves to establish the expected error in the interpolated solutions relative to direct modeling results. The verification process included four steps: (1) a review of the linear-elastic stress intensity solutions at the first model load increment, (2) confirmation of elastic-plastic model convergence through domain integral independence at the final model load increment, (3) comparison of interpolated solutions against a 25 model benchmark solution set, and (4) review of an existing round robin (RR) on elastic-plastic surface crack analysis and a comparison of an interpolated solution relative to the population of independent RR solutions.

3.1 Representative Model Results

The following parametric study provides a brief review to help visualize the influence of the parameters in the interpolation space. The same model used in section 2.5.2 with $a/B = 0.6$, $a/c = 0.6$, $n = 6$, and $E/\sigma_{ys} = 300$ was chosen as a representative result set from near the center of the geometry and material matrices. As discussed in the case study, these parameters fall directly on a model within the space requiring no interpolation. Each of the parametric variations described also fall directly on existing solutions. By holding the representative model parameters constant and individually varying a/B, a/c, n, and E/σ_{ys} across their respective matrix values, useful figures can be made demonstrating the effects of varying geometry and material values. Each of the figures 21–24 has three subplots for the representative model and various choices of a/B, a/c, n, and E/σ_{ys}: (a) σ_n versus $CMOD_n$, (b) $J_n(\phi = 90°)$ versus $CMOD_n$, and (c) $J_n(\phi)$. In figures 21–24, the maximum common $CMOD_n$ value for all of the FEMs being compared is designated with a vertical line in parts (a) and (b) of the figures. The $J_n(\phi)$ results plotted in part (c) correspond to the maximum common $CMOD_n$. It is also important to note that the results presented in figures 21–24 are data directly from the FEM; they have not yet been interpolated into uniform ϕ or load increments.

Figure 21 illustrates the effect of varying crack depth, a/B, with a/c, n, and E/σ_{ys} held constant for the representative geometry. Changes in a/B have a nearly uniform effect on σ_n versus $CMOD_n$, $J_n(\phi = 90°)$ versus $CMOD_n$, and $J_n(\phi)$. In figure 21(c), the magnitude and shape of the J_n-ϕ curves differ primarily because at the maximum common $CMOD_n$ point, the $a/B = 0.2$ and 0.4 analyses are nonlinear in their global response, while the other a/B results are still linear-elastic.

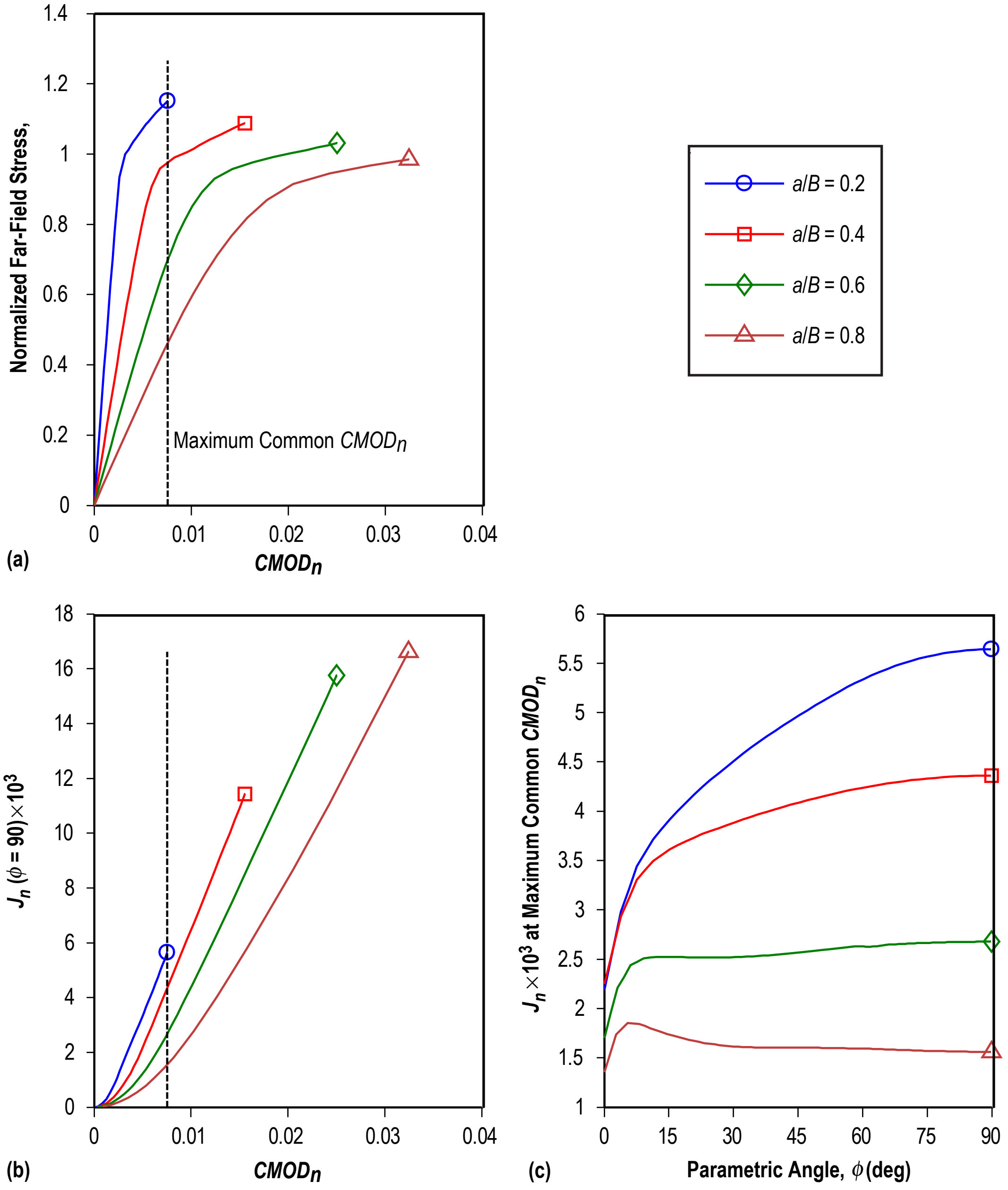

Figure 21. Comparison of results for (a) σ_n versus $CMOD_n$, (b) $J_n(\phi = 90°)$ versus $CMOD_n$, and (c) J_n versus ϕ for various a/B values, $a/c = 0.6$, $n = 6$, and $E/\sigma_{ys} = 300$.

Figure 22 illustrates the effect of varying crack aspect ratio, a/c, with a/B, n, and E/σ_{ys} held constant. Changing a/c does not have a uniform effect on σ_n versus $CMOD_n$. There is a significantly different response for the $a/c=0.2$ and $a/c=0.4$, σ_n versus $CMOD_n$ curves indicating that perhaps a set of results at $a/c=0.3$ would be useful to improve interpolation between these curves. Parts (b) and (c) of figure 22 confirm that J_n versus $CMOD_n$ at $\phi=90°$ is controlled primarily by crack depth, a/B. The crack aspect ratio drives J_n variations for other ϕ locations.

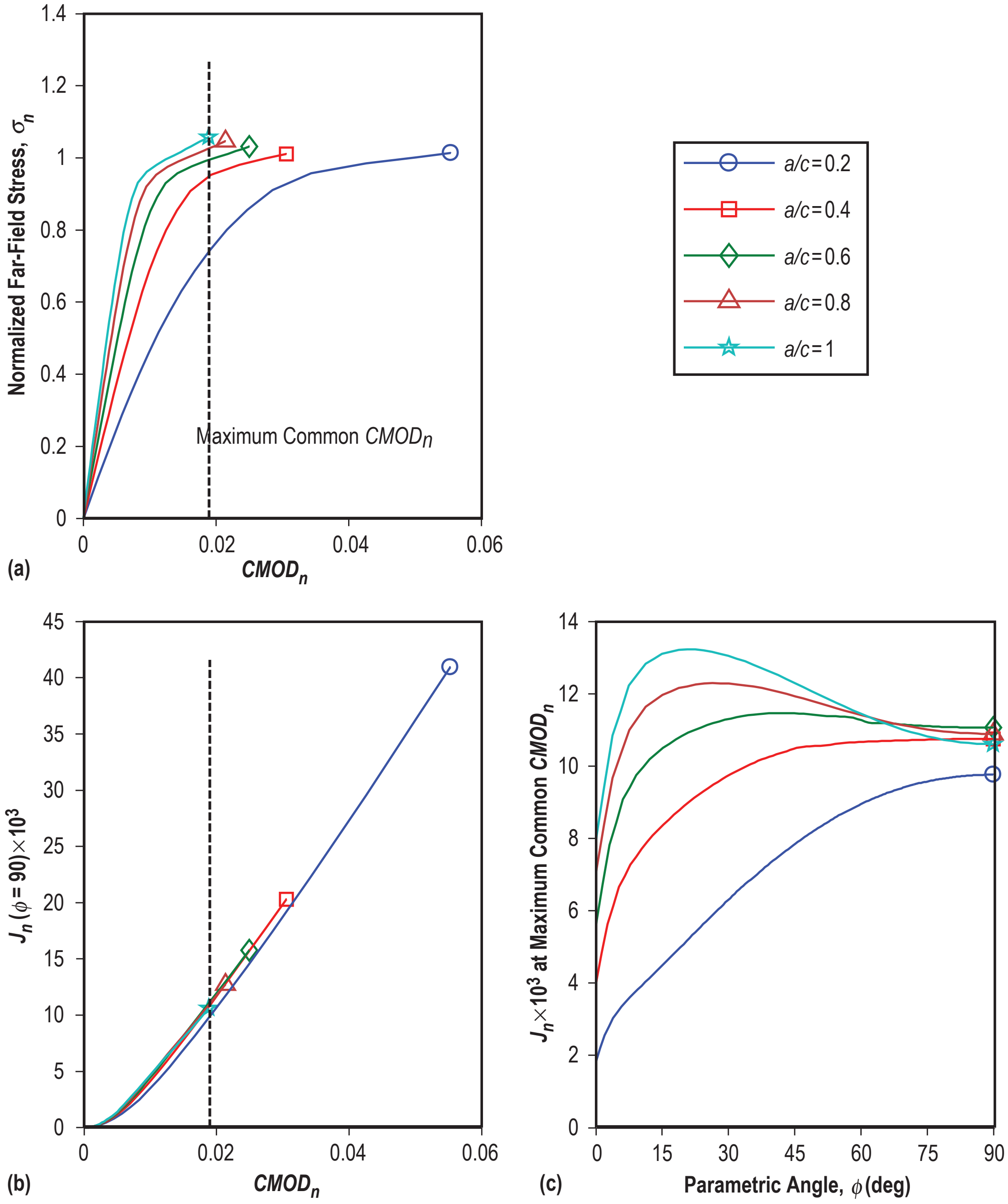

Figure 22. Comparison of results for (a) σ_n versus $CMOD_n$, (b) $J_n(\phi=90°)$ versus $CMOD_n$, and (c) J_n versus ϕ for $a/B=0.6$, various a/c values, $n=6$, and $E/\sigma_{ys}=300$.

Figure 23 illustrates the effect of varying strain hardening exponent, *n,* with a/B, a/c, and E/σ_{ys} held constant. As expected, changes in n have no effect on the linear portion of the σ_n versus $CMOD_n$ response but do affect the curve once nonlinear. Following directly from the LPPL tensile response, the $n=3$ model has the highest σ_n for a given $CMOD_n$ while the $n=20$ nonlinear response is almost flat and has the lowest σ_n for a given $CMOD_n$. In figure 23(b), the $J_n(\phi=90°)$ versus $CMOD_n$ results are identical for all n values for low deformations in the LEFM regime and then begin to diverge for higher deformations as plasticity increases. Compared to the other parameters, the strain hardening exponent has the weakest effect on the solution space.

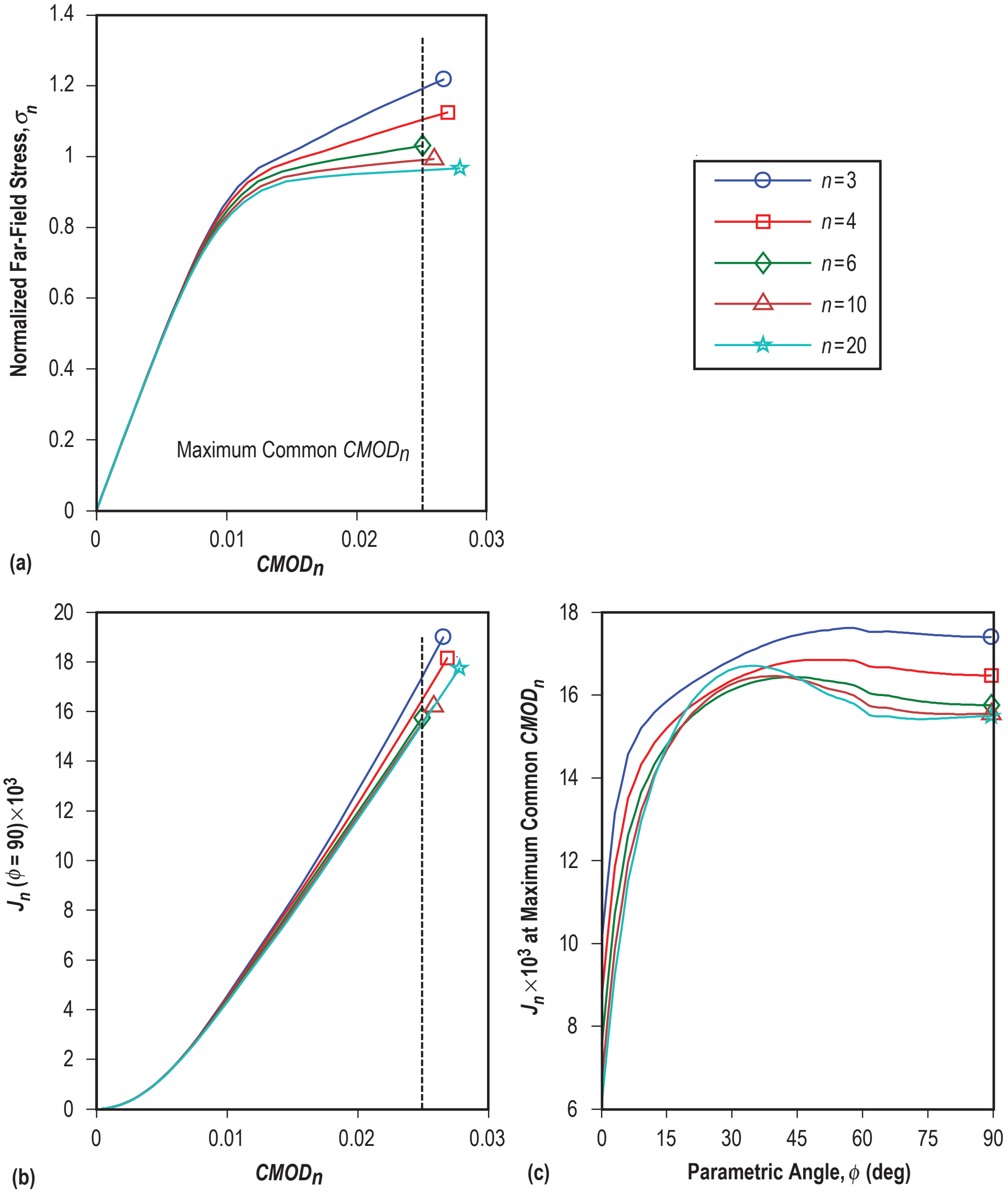

Figure 23. Comparison of results for (a) σ_n versus $CMOD_n$, (b) $J_n(\phi=90°)$ versus $CMOD_n$, and (c) J_n versus ϕ for $a/B=0.6$, various n values, and $E/\sigma_{ys}=300$.

Figure 24 illustrates the effect of varying the reciprocal of the yield strain, $E/\sigma_{ys} = 1/\varepsilon_{ys}$, with a/B, a/c, and n held constant. In figure 24(a), the σ_n versus $CMOD_n$ response is very sensitive to the E/σ_{ys} value and is not a linear function of E/σ_{ys}. The J_n-ϕ results in figure 24(c) also appear to be a nonlinear function of E/σ_{ys}. These observations led to the choice of linear interpolation for E/σ_{ys} being performed in terms of $\log_{10}(E/\sigma_{ys})$ as discussed previously in section 2.5. Interpolation in terms of ε_{ys} would also be a potential option for future investigation. These observations also suggest that a set of results at $E/\sigma_{ys} = 150$ would be useful to improve interpolation between the $E/\sigma_{ys} = 100$ and 200 solutions.

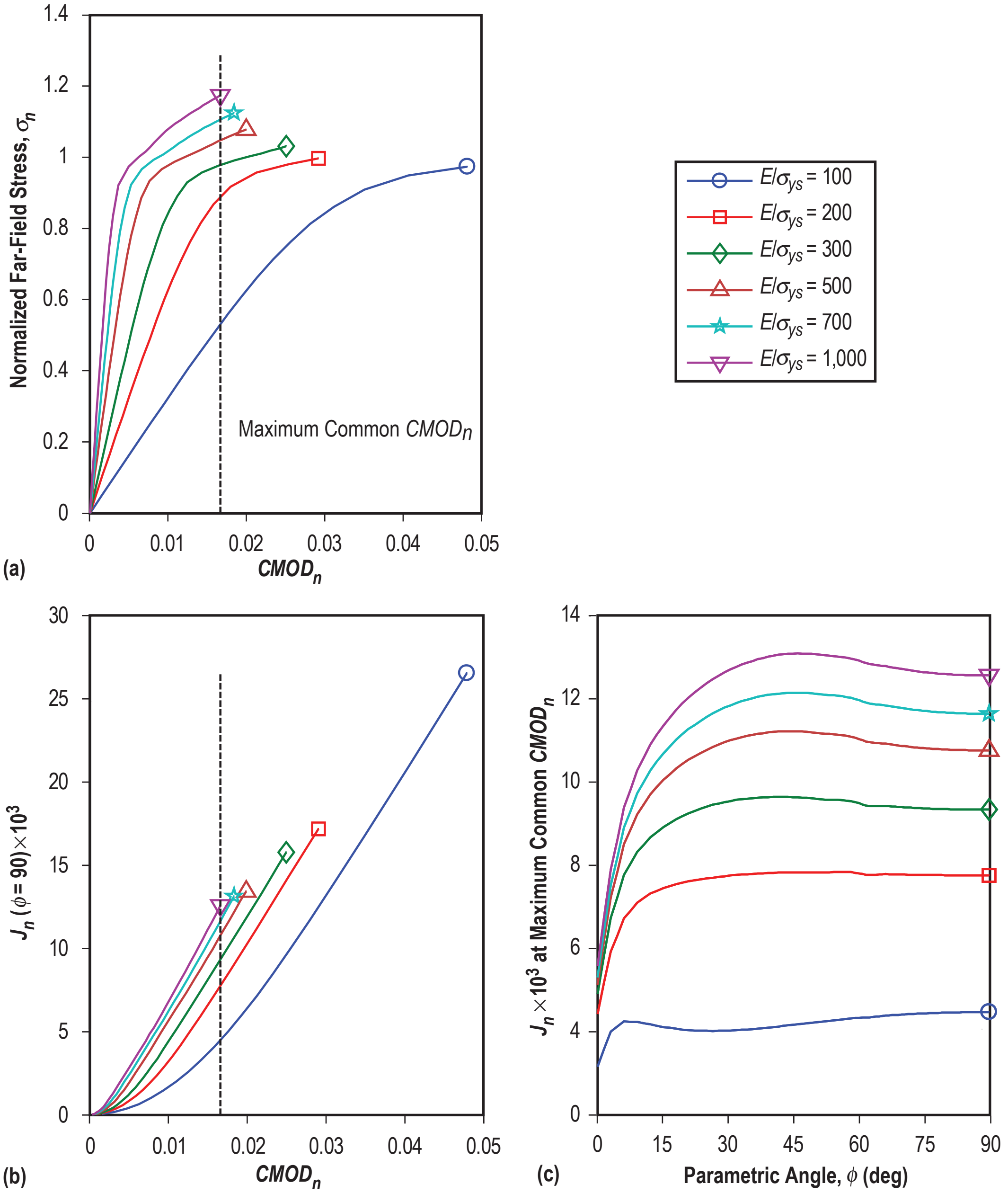

Figure 24. Comparison of results for (a) σ_n versus $CMOD_n$, (b) $J_n(\phi = 90°)$ versus $CMOD_n$, and (c) J_n versus ϕ for $a/B = 0.6$, $a/c = 0.6$, $n = 6$, and various E/σ_{ys} values.

3.2 Verification Process

3.2.1 Linear-Elastic Result Comparisons

The linear-elastic J_n results were compared with linear-elastic stress intensity results calculated using Newman-Raju equations.[4] This comparison confirms the basic quality of the 20 FEM geometries used in this study by reaffirming the well-established NR solutions for surface cracks in tension. To establish a basis for comparison, the $J_n(\phi)$ results from the first load increment for each of the 20 geometries were converted to the mode I linear-elastic stress intensity factor, K_I, through the plane strain equation:

$$K_I = \sqrt{\frac{JE}{\left(1-\nu^2\right)}} \quad . \tag{11}$$

The specific material combination used for this comparison is not important because K_I is independent of material properties, and J_n can be considered completely elastic at the first load increment in each analysis. A geometry correction factor, λ, was then calculated for each of the 20 configurations using the equation

$$\lambda = \frac{K_I}{\sigma\sqrt{\pi a}} \quad . \tag{12}$$

The specific stress and geometry of each FEM was input into the NR equations to calculate λ_{NR} for each ϕ location along the crack front using equation (12). Figure 25 shows the results of the comparison between the linear-elastic FEM results and the NR equations by plotting the ratio $\lambda_{FEM}/\lambda_{NR}$ versus ϕ. A solid, heavy horizontal line is drawn at a ratio value of 1, indicating perfect agreement for all ϕ locations, and dashed horizontal lines are drawn above and below to indicate 5% deviation. The symbols in figure 25 represent a/B values and the colors represent a/c values. Newman and Raju[3] report that their surface crack stress intensity equation was within ±5% of their FEM results for $a/B<0.8$, but the accuracy of the equation is unknown for $a/B>0.8$. Overall, the FEMs and the NR solutions are in excellent agreement with only two models with $a/B=0.8$ deviating by more than 5% at the depth location for deep cracks. In general the λ_{FEM} values are marginally less than the λ_{NR} values, confirming the slightly conservative nature of the NR equations for K_I calculations.

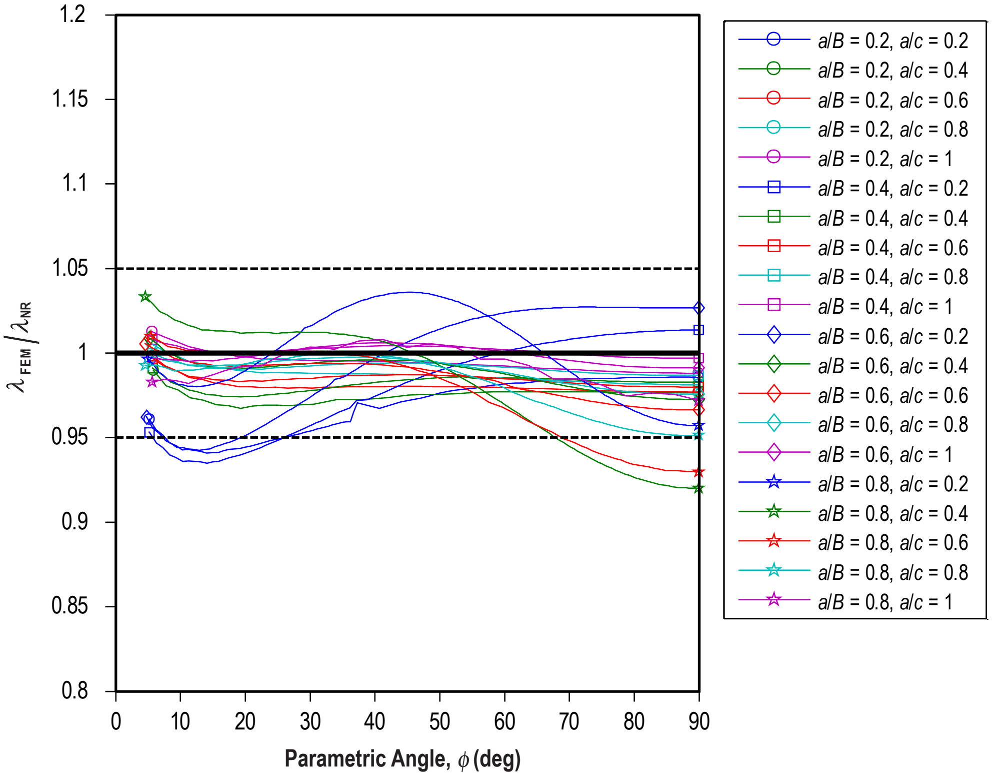

Figure 25. Comparison of linear-elastic stress intensity correction factors from the NR equations to the values calculated from the 20 geometries in this study.

3.2.2 J-Integral Solution Convergence Checks

The next step in the verification process is to confirm the quality of the elastic-plastic *J*-integral solution at the final load increment of each model as indicated by the path independence of the *J*-integral. All 600 FEMs used in the study are confirmed to have converged *J*-integral values based on this metric. *J*-integral convergence becomes more difficult with increasing plasticity, thus checking convergence at the final load increment confirms the quality of the complete analysis. Figure 26 demonstrates the path dependence of the J_n values at $\phi = 90°$ for the last analysis step in all 600 models. In this figure, the horizontal axis is the domain integral number with 1 being the innermost domain nearest the crack tip and 10 being the outermost domain. The vertical axis represents the J_n values at $\phi = 90°$ for the last load increment normalized by the maximum J_n domain value for that FEM at $\phi = 90°$; therefore, each domain location in figure 26 contains 600 data points. As expected, the largest deviation from the outermost domain value is nearest the crack tip at domain 1, and the J_n values rapidly converge towards the outermost domain value. As a check of domain convergence, the percent difference between the domain 9 and 10 J_n values is calculated for every ϕ location in all the models at the last load increment. Figure 27 illustrates the percent difference between domain 9 and 10 J_n values at every ϕ across the entire solution space. The FEMs demonstrate excellent J_n convergence with most of the data having 0.5% or less difference between the last two domains. Slightly higher differences exist at the free surface location, but the differences still remain below 0.85%. From this plot, one concludes that the FEMs all had a sufficient number of domains and a large enough outer domain size to ensure sufficiently converged J_n values at the last load increment of every analysis.

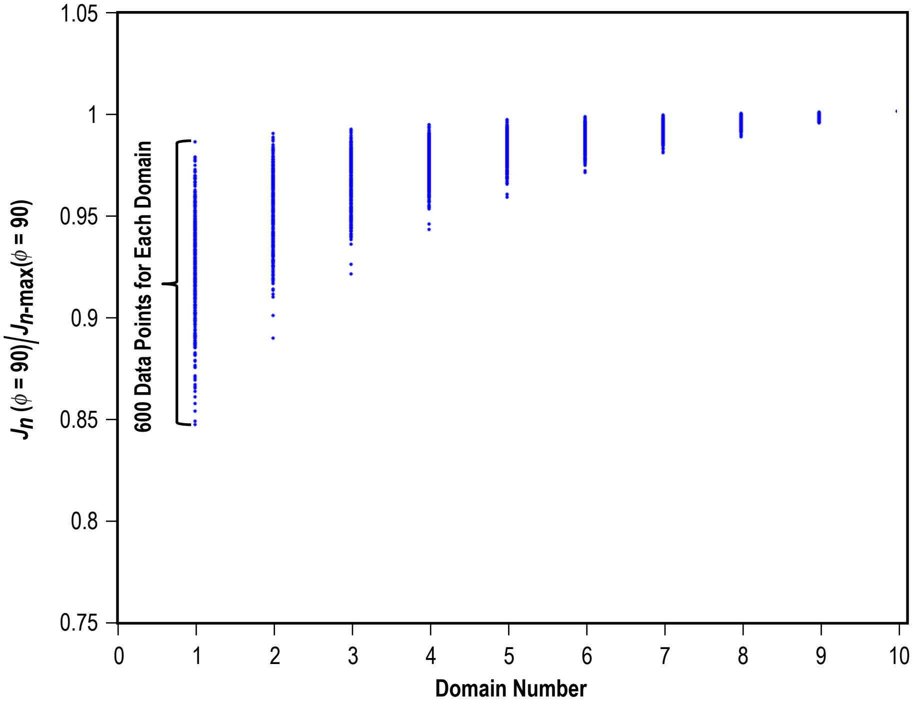

Figure 26. Normalized $J_n(\phi = 90°)$ for each domain at the final load step for all 600 solutions.

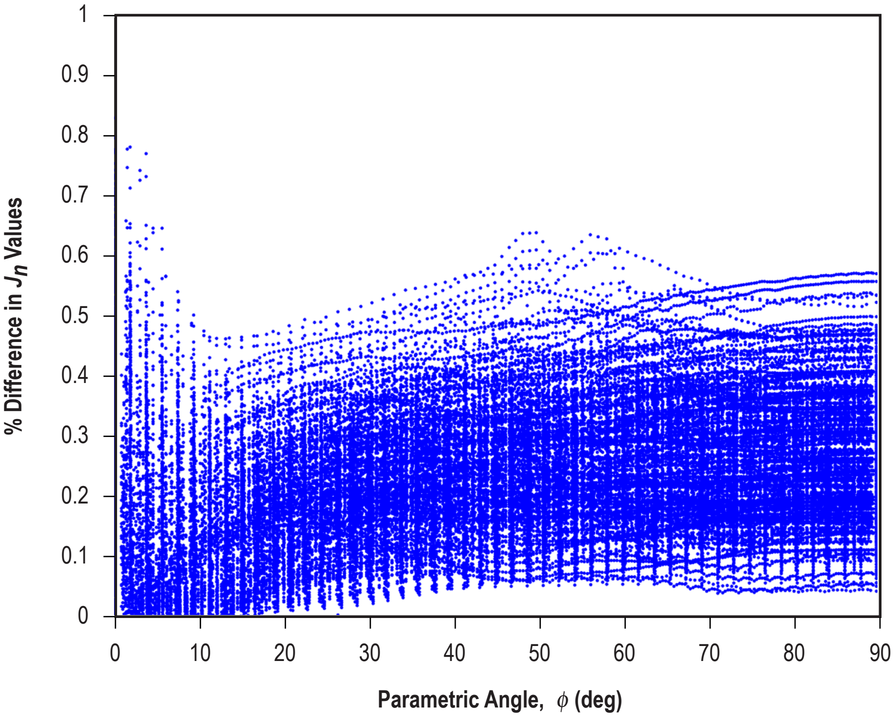

Figure 27. Percent difference in domains 9 and 10 J_n values for all ϕ locations at the final load step for all 600 solutions.

3.3 Elastic-Plastic Solution Comparison to Benchmark Data Set

3.3.1 Description of Benchmark Data Set

The quality of the linear-elastic FEM solutions was confirmed through comparison to the Newman-Raju equations. Unfortunately, no such established solution exists for comparison of the elastic-plastic J-integral results; therefore, the authors developed a set of elastic-plastic 'benchmark' solutions consisting of 25 FEMs to verify the surface crack solution interpolation methodologies. Five surface crack geometries and five materials were chosen to comprise the benchmark solutions set. The geometry and material choices are given in table 1 and were chosen to fall in the 'gaps' in the geometry and material matrices. The benchmark FEMs were built, executed, and post-processed using the same methods described in section 2. All of the benchmark FEM results were then collected in a Matlab data structure.

Table 1. Benchmark FEM geometry and material values.

Geometry Values	
a/B	a/c
0.3	0.3
0.3	0.9
0.5	0.5
0.7	0.3
0.7	0.9

Material Values	
n	E/σ_{ys}
3.5	150
3.5	850
8	400
15	150
15	850

3.3.2 Comparison of Interpolated Solutions and Benchmark Dataset

A Matlab script was written to evaluate an interpolated solution for each of the 25 benchmark solutions. The script then creates a series of plots and tables comparing the benchmark and interpolated solutions to aid in investigating the effectiveness of the interpolation methodology. Table 2 lists the a/c, a/B, n, and E/σ_{ys} values for the benchmark models and assigns a 'model No.' label to each. For each benchmark case, two values of $CMOD_n$ ($CMOD_n$ A and B) were chosen as displacement levels at which to compare the results. $CMOD_n$ A represents a point slightly past the LEFM regime, just beyond the rollover in the P versus $CMOD_n$ trace. $CMOD_n$ B is the point of highest common load increment between the benchmark FEM and the interpolated solution and represents the EPFM regime with large plasticity. The regime between $CMOD_n$ A and $CMOD_n$ B is the intended range for use of this solution set. Table 2 contains the percent difference between the benchmark solutions and the interpolated solutions for P, $J_n(\phi = 30°)$, and $J_n(\phi = 90°)$ at $CMOD_n$ A and B. Overall, the interpolated solutions are a nice match to the benchmark solutions. At $CMOD_n$ A, the average percent difference for all compared values is less than 5%, and at $CMOD_n$ B the average percent difference is less than 3%. The largest percent difference at $CMOD_n$ A is 11% for the model No. 5 $J_n(\phi = 30°)$ comparison, and the largest percent difference at $CMOD_n$ B is 6% for the model No. 19 $J_n(\phi = 30°)$ comparison.

Table 2. Benchmark model numbers, model descriptions, and interpolated result comparisons.

					% Difference at *CMOD* A			% Difference at *CMOD* B		
Model No.	a/B	a/c	n	E/σ_{ys}	P	J_n (ϕ = 30°)	J_n (ϕ = 90°)	P	J_n (ϕ = 30°)	J_n (ϕ = 90°)
1	0.3	0.3	3.5	150	4.4	5.5	1.8	–2.4	4.5	3.9
2	0.3	0.3	3.5	850	–1.0	3.6	0.8	–3.7	1.5	1.5
3	0.3	0.3	8.0	400	7.5	9.2	3.9	–1.9	3.2	3.4
4	0.3	0.3	15.0	150	9.3	8.2	4.2	2.1	3.7	4.9
5	0.3	0.3	15.0	850	6.8	11.0	3.9	–1.0	4.1	4.5
6	0.3	0.9	3.5	150	1.7	1.9	0.7	–3.3	1.4	1.3
7	0.3	0.9	3.5	850	–0.4	1.4	0.5	–3.6	–0.2	0.1
8	0.3	0.9	8.0	400	1.6	5.1	3.9	–1.7	1.5	1.5
9	0.3	0.9	15.0	150	7.5	5.8	4.2	0.2	4.0	3.7
10	0.3	0.9	15.0	850	3.8	6.5	5.4	–1.0	2.3	2.0
11	0.5	0.5	3.5	150	2.1	3.5	1.2	–1.8	2.8	2.0
12	0.5	0.5	3.5	850	–1.0	1.8	0.0	–2.0	0.5	0.4
13	0.5	0.5	8.0	400	3.1	4.8	1.8	–1.7	2.0	1.0
14	0.5	0.5	15.0	150	6.7	4.8	1.7	1.5	4.1	2.4
15	0.5	0.5	15.0	850	3.4	4.7	1.0	–1.4	2.5	1.1
16	0.7	0.3	3.5	150	4.7	5.8	–0.4	–1.6	5.4	0.7
17	0.7	0.3	3.5	850	3.0	4.6	–1.3	–1.4	2.5	–2.0
18	0.7	0.3	8.0	400	5.2	6.1	–2.3	0.8	4.0	–1.3
19	0.7	0.3	15.0	150	6.4	5.9	–1.4	1.4	6.0	0.4
20	0.7	0.3	15.0	850	4.2	5.8	–3.0	0.2	3.7	–1.2
21	0.7	0.9	3.5	150	3.1	1.9	0.5	–1.9	0.7	–1.1
22	0.7	0.9	3.5	850	1.4	1.0	–0.3	–2.0	–0.8	–2.4
23	0.7	0.9	8.0	400	3.3	1.7	–0.5	–1.1	0.7	–1.7
24	0.7	0.9	15.0	150	5.3	1.9	0.1	1.4	2.9	1.2
25	0.7	0.9	15.0	850	1.0	1.4	–0.9	–0.8	1.0	–0.8
				Max.	9.3	11.0	5.4	2.1	6.0	4.9
				Avg.	3.7	4.6	1.0	–1.1	2.6	1.0
				Min.	–1.0	1.0	–3.0	–3.7	–0.8	–2.4
				Std. Dev.	2.7	2.6	2.2	1.6	1.7	2.0

The aforementioned Matlab script creates a series of six comparison plots for each of the 25 benchmark FEMs. Figures 28 and 29 show two examples of the comparison plot series for model No. 1 and model No. 25, and the complete set of comparison plots are included in appendix B. Figures 28 and 29 each have six plots (a)–(f) that are described as follows:

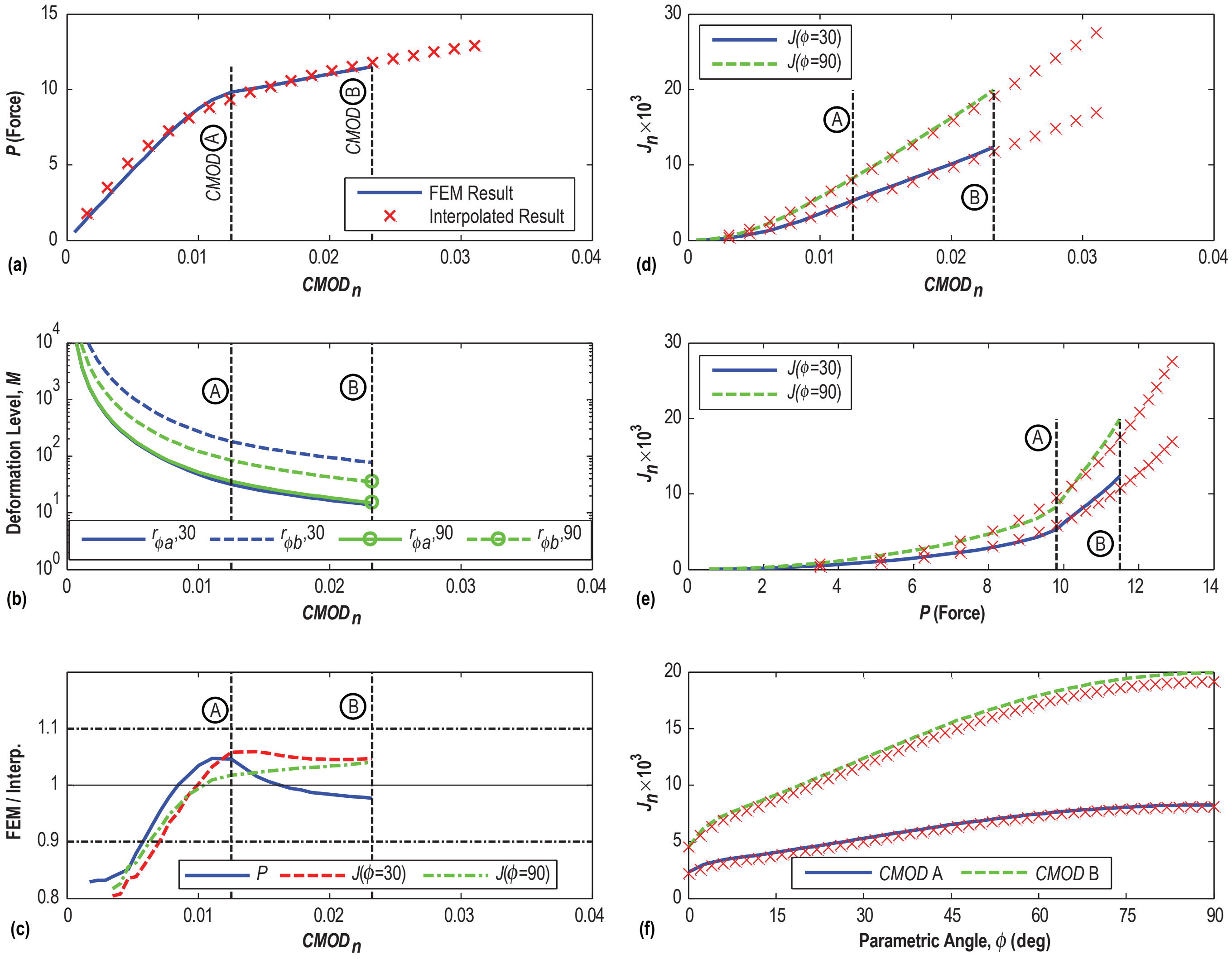

Figure 28. Comparison of benchmark model No. 1 FEM results and interpolated results for (a) P versus $CMOD_n$, (b) M versus $CMOD_n$, (c) benchmark FEM/interpolated results versus $CMOD_n$, (d) J_n versus $CMOD_n$ at $\phi = 30°$ and 90°, (e) J_n versus P at $\phi = 30°$ and 90°, and (f) J_n versus ϕ for $CMOD_n$ values A and B.

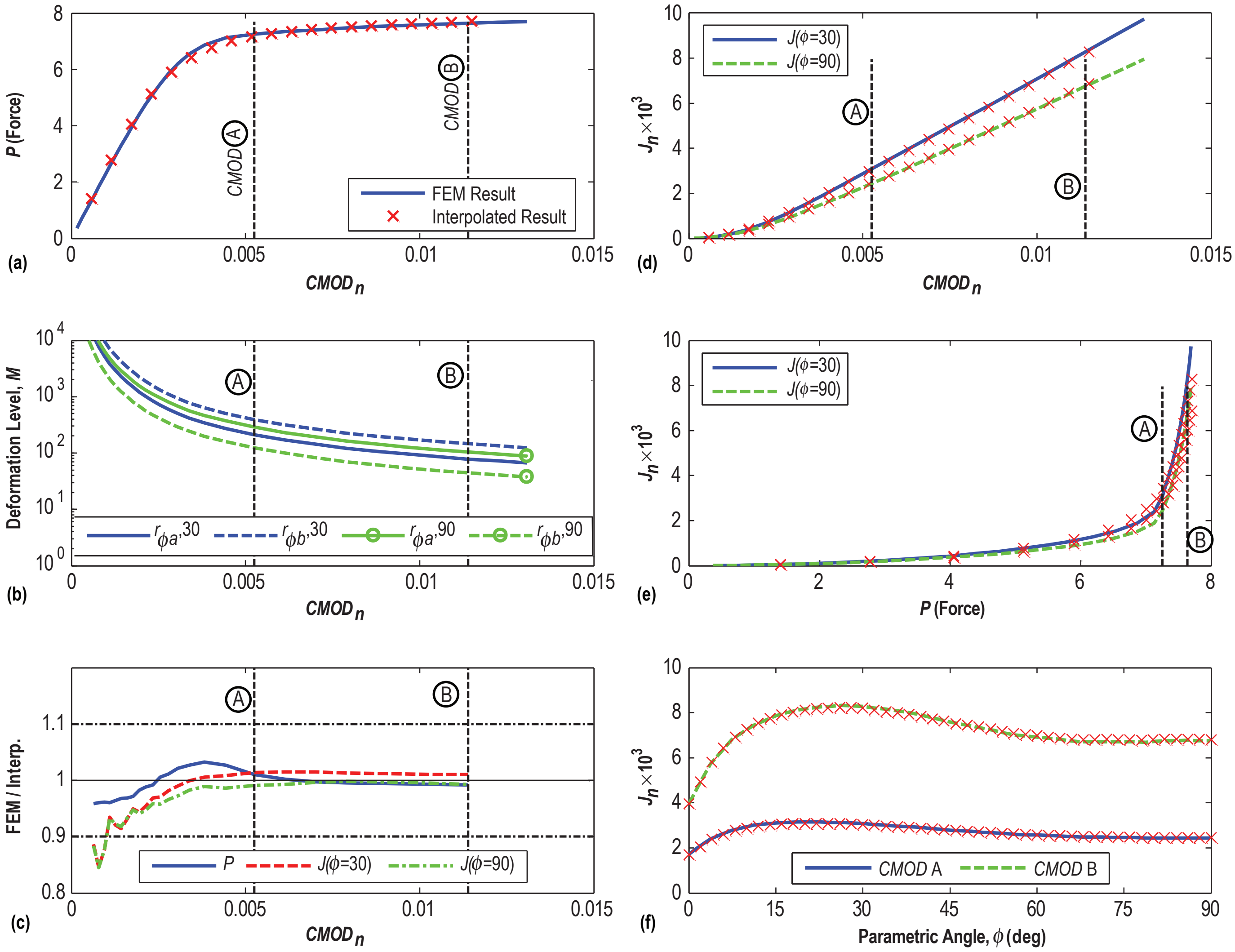

Figure 29. Comparison of benchmark model No. 25 FEM results and interpolated results for (a) P versus $CMOD_n$, (b) M versus $CMOD_n$, (c) benchmark FEM/interpolated results versus $CMOD_n$, (d) J_n versus $CMOD_n$ at $\phi = 30°$ and 90°, (e) J_n versus P at $\phi = 30°$ and 90°, and (f) J_n versus ϕ for $CMOD_n$ values A and B.

- Plot (a) compares the reaction force, P, versus $CMOD_n$ results for the benchmark FEM and corresponding interpolated solution. In this plot, the solid line represents the benchmark FEM solution and the red 'X' symbols represent the interpolated result at the 20 distinct load increments in the interpolated solution. In plots (a)–(d), vertical dashed lines are drawn at $CMOD_n$ A and $CMOD_n$ B.

- Plot (b) illustrates the deformation level, M, as a function of $CMOD_n$. The four curves represent different M-values from equation (3) where r_ϕ is $r_{\phi a}$ and $r_{\phi b}$ at $\phi = 30°$ and 90°, respectively.

- Plot (c) presents a ratio of benchmark FEM results to interpolated results for P, $J_n(\phi = 30°)$, and $J_n(\phi = 90°)$ as a function of $CMOD_n$. Perfect agreement is symbolized by the horizontal line at a ratio value of 1 while ±10% variation lines are drawn as horizontal dash-dot lines.

- Plot (d) illustrates $J_n(\phi = 30°)$ and $J_n(\phi = 90°)$ versus $CMOD_n$ for the benchmark FEM and corresponding interpolated solution. For plots (d)–(f), the solid and dashed lines represent the benchmark FEM solution and the red 'X' symbols indicate the interpolated result.

- Plot (e) shows $J_n(\phi = 30°)$ and $J_n(\phi = 90°)$ versus P for the benchmark FEM and corresponding interpolated solution. Two vertical dashed lines are drawn at the benchmark FEM reaction forces corresponding to $CMOD_n$ A and $CMOD_n$ B.

- Plot (f) compares $J_n(\phi)$ for the benchmark FEM and related interpolated solution for deformation levels corresponding to $CMOD_n$ A and $CMOD_n$ B.

3.4 Interpolated Solution of the Round Robin Surface Crack Test

The authors led an interlaboratory round robin concerning the elastic-plastic analysis of surface cracked plates with 15 participants as documented in NASA/TM—2012–217456.[17] A surface crack tension test was performed to serve as the basis for the RR work. The experiment employed a 2219-T8 aluminum specimen with $W = 88.82$ mm, $B = 9.5$ mm, $L = 177.8$ mm (uniform cross section length), $a = 6.17$ mm, and $2c = 12.7$ mm as shown in figure 30. The specimen was loaded under displacement control in tension until ductile tearing was detected. The tearing force was 252 kN corresponding to a tearing $CMOD$ of 0.114 mm. The extent of ductile tearing was then highlighted using a combination of sodium hydroxide surface staining and fatigue cycling to mark the surface, and the specimen was then loaded to failure. Figure 31 shows a picture of the fracture surface with the local location of ductile tearing shown at $\phi = 17°$.

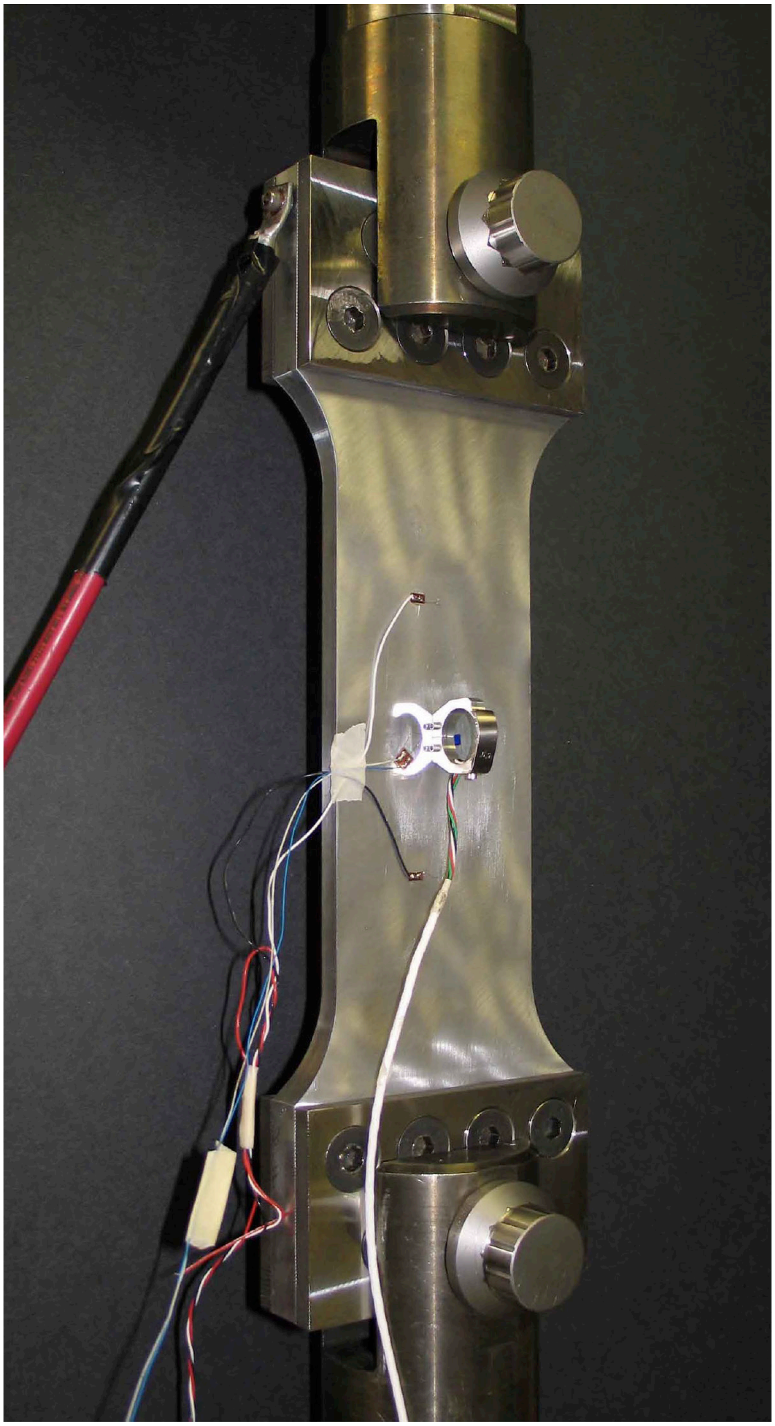

Figure 30. Round robin specimen configured for testing.

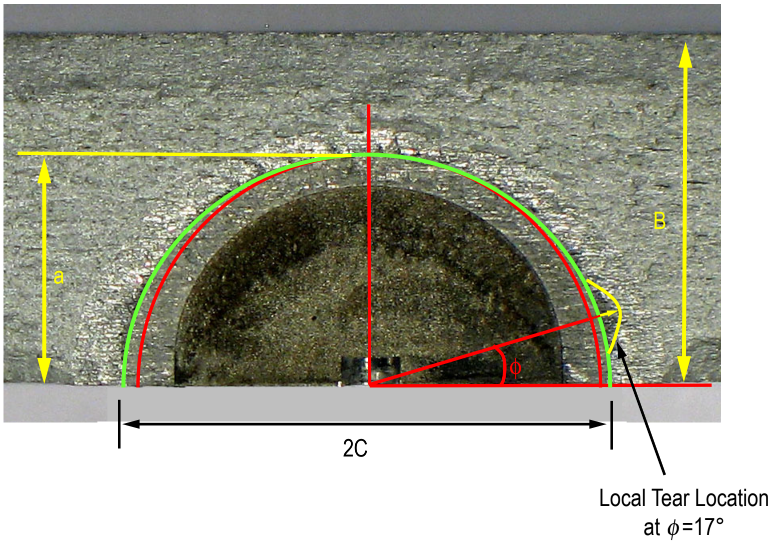

Figure 31. Round robin specimen fracture surface with tearing location indicated.

An interpolated solution was used to analyze the test and this analysis is compared to the FEAs of the RR participants. In the following section, the authors' original FEA performed for the RR is labeled 'FEA,' and the other participants' results are labeled 'labs 2–15.' An LPPL approximation of the material's stress-strain curve is required to estimate an interpolated solution to the problem. The interpolated solutions assume the same elastic properties provided to the RR participants ($E = 74.46$ GPa and $\nu = 0.33$) with the exception that ν is a fixed value of 0.3 in all of the interpolated solutions. Figure 32 illustrates the 2219-T87 engineering stress versus engineering strain test data as a dashed line. The RR participants were free to model this material behavior in any fashion. The open circle symbols in figure 32 show the authors' original RR FEA stress-strain table inputs in the form of a multilinear approximation of the uniaxial tensile test data. The first data point used in the original analysis is at a stress value close to the proportional limit and well below the 0.2% offset yield value. Using an LPPL representation of the stress-strain curve does not allow one to place the initial yield point this low and still capture the remainder of the plastic behavior, so compromises have to be made to attempt a 'best fit' of the experimental stress-strain data. For interpolated solutions, the authors chose five reasonable fits to the nonlinear portion of the stress-strain curve labeled 'int. 1' through 'int. 5' in figure 32, and table 3 lists the σ_{ys} and n values assumed for each of the five cases. Int. 1 assumes a lower value of σ_{ys} and a lower n value while int. 5 assumes a higher σ_{ys} value close to the 0.2% offset yield value and a correspondingly higher n value. All five cases were chosen to represent reasonable engineering choices for fitting the material behavior, and the sensitivity to the material choices were studied.

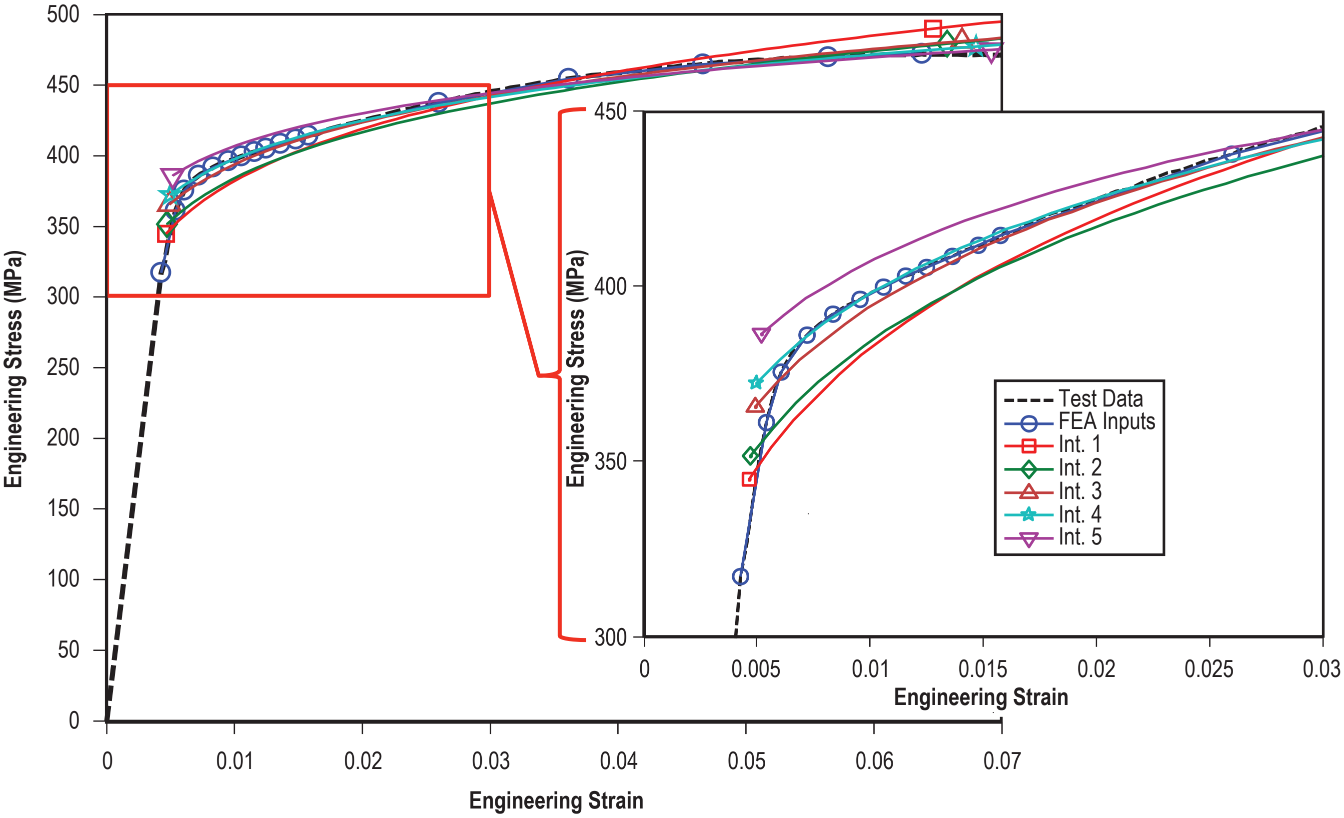

Figure 32. Round robin uniaxial tensile stress versus strain data compared with FEA and LPPL material fits.

Table 3. Round robin FEM and interpolation method sensitivity study result comparisons.

Result Name	σ_{ys} (MPa)	*n*	*J* (ϕ = 17°) (kJ/m^2)	*J* % Diff. from FEA	*P* at Tearing *CMOD* (kN)	*P* % Diff. From Test	*P* % Diff. From FEA
FEA	stress–strain table		19.75	0.00	258.9	2.81	0.00
Int. 1	344.7	7.5	19.63	–0.65	252.8	0.40	–2.35
Int. 2	351.6	8.5	19.80	0.22	255.4	1.44	–1.33
Int. 3	365.4	9.5	20.14	1.94	261.6	3.90	1.05
Int. 4	372.3	10.5	20.31	2.80	264.3	4.94	2.07
Int. 5	386.1	12.5	20.55	4.05	267.6	6.27	3.36

Figure 33 illustrates the effect of the choice of LPPL material constants on (a) P versus $CMOD$, (b) J versus $CMOD$ at $\phi = 17°$, and (c) $J(\phi)$. The figure compares the interpolated results to the authors' RR FEA results. The results are essentially identical in the linear-elastic regime and then diverge as plasticity increases. All of the interpolated solutions extend to a greater deformation level than the FEA result. Int. 4 and 5 extend to a higher deformation level than int. 1–3 because of the different 16 nearest neighbor subsets used in the solutions due to the differing choices for n. Dashed vertical lines are drawn in figures 33(a) and (b) that correspond to the test tearing $CMOD$ and the maximum $CMOD$ achieved in the FEA result. Part (c) illustrates the J versus ϕ results at these two $CMOD$ levels. The biggest effect of the change in LPPL material properties is in the nonlinear P-$CMOD$ response; the interpolated J-integral results are fairly insensitive to the given choices for plastic material properties. Table 3 gives the J-integral values for $\phi = 17°$ and the P results at the tearing $CMOD$. The percent difference between the FEA and interpolated solution J-integral results are small and range from –0.65% to 4.05%. The percent difference between the FEA and interpolated solution force values at the tearing $CMOD$ are also small and range from –2.35% to 3.36%. The percent difference between all of the solutions and the test load at tearing are also tabulated, and all but int. 5 are within 5% of the test result.

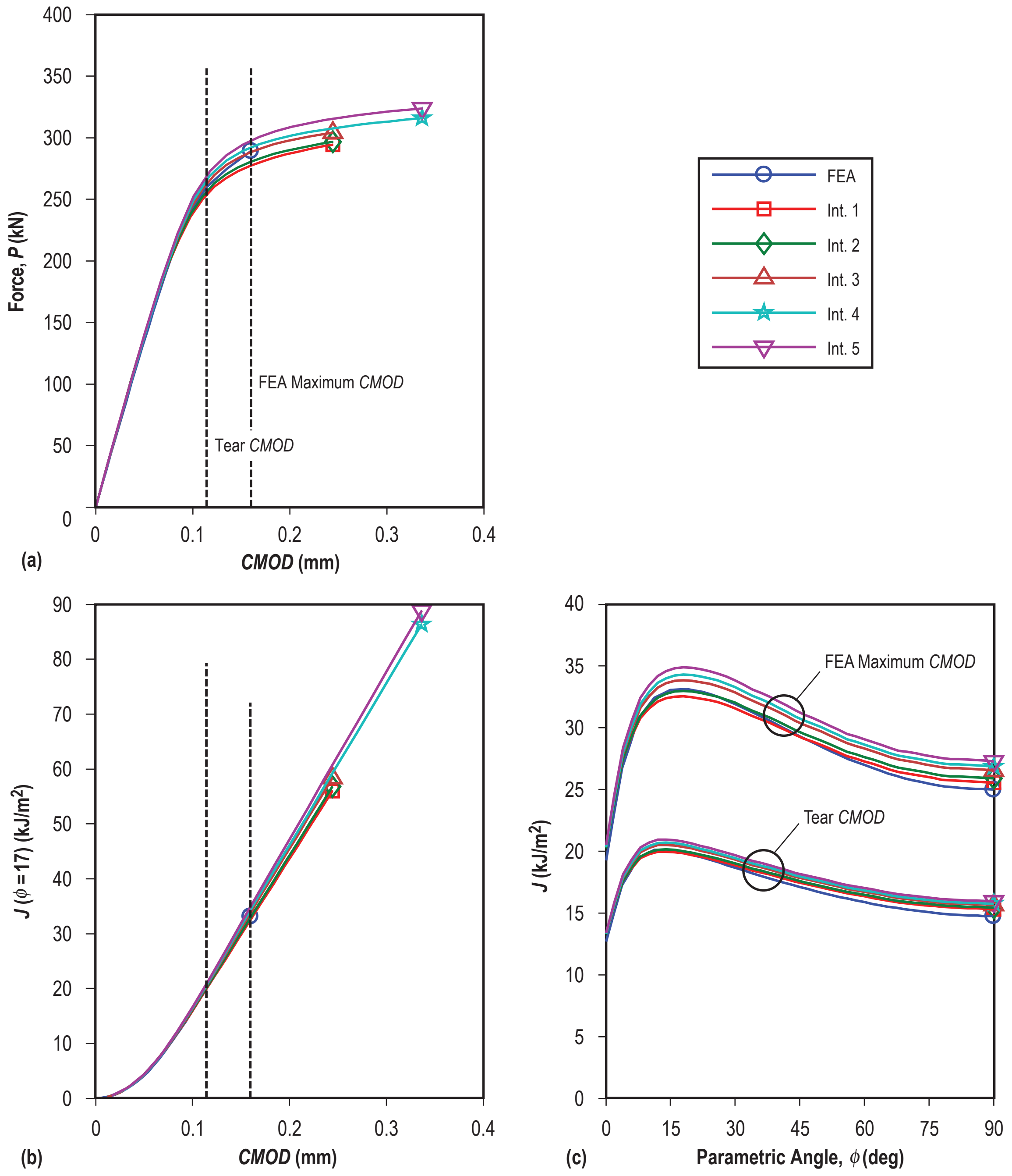

Figure 33. Influence of LPPL material choice on results for (a) P versus $CMOD$, (b) $J(\phi = 17°)$ versus $CMOD$, and (c) J versus ϕ.

Interpolation result int. 3 was chosen as representative of an 'average' choice for material properties and was then compared to the overall RR family of results for all laboratories. Figure 34 shows the comparison of the P versus $CMOD$ test data with the authors' original FEA, the interpolated solution int. 3, and the analysis results of other RR participants, labs 2–15. The interpolated solution falls within the family of the RR results. It is important to recall that the interpolated solution is generic. It provides a result out to the average $CMOD_n$ of its 16 nearest neighbors, so the final $CMOD$ of the int. 3 solution is not part of the prediction; rather, it is the P versus $CMOD$ trace up through a specified $CMOD$ value that is of interest. Figure 35 compares the J-integral values at $\phi = 17°$ versus the $CMOD$ results, the interpolated solution, and all of the labs' solutions. Again, the interpolated solution is in excellent agreement with the family of solutions represented in the RR. Figure 36 shows the same data with the trajectory lines removed for all but the interpolated solution. The RR participants were asked to provide J-integral results at three force levels (200, 252, and 289 kN) as shown by the discrete '+'-shaped data points. To illustrate the reduced error when establishing J-integral values from $CMOD$ as opposed to force, each of the RR participants' solutions was interpolated at $CMOD$ values equal to the experimental $CMOD$ at 256 kN and also at 0.15 mm. The reduced scatter in the J solutions is evident as revealed by the solid circles in figure 36. Moreover, it is clear from the trace of the interpolated solution that it passes cleanly through the family of RR results at these $CMOD$ values, providing an answer of equivalent quality to that expected from a custom finite element assessment of the test.

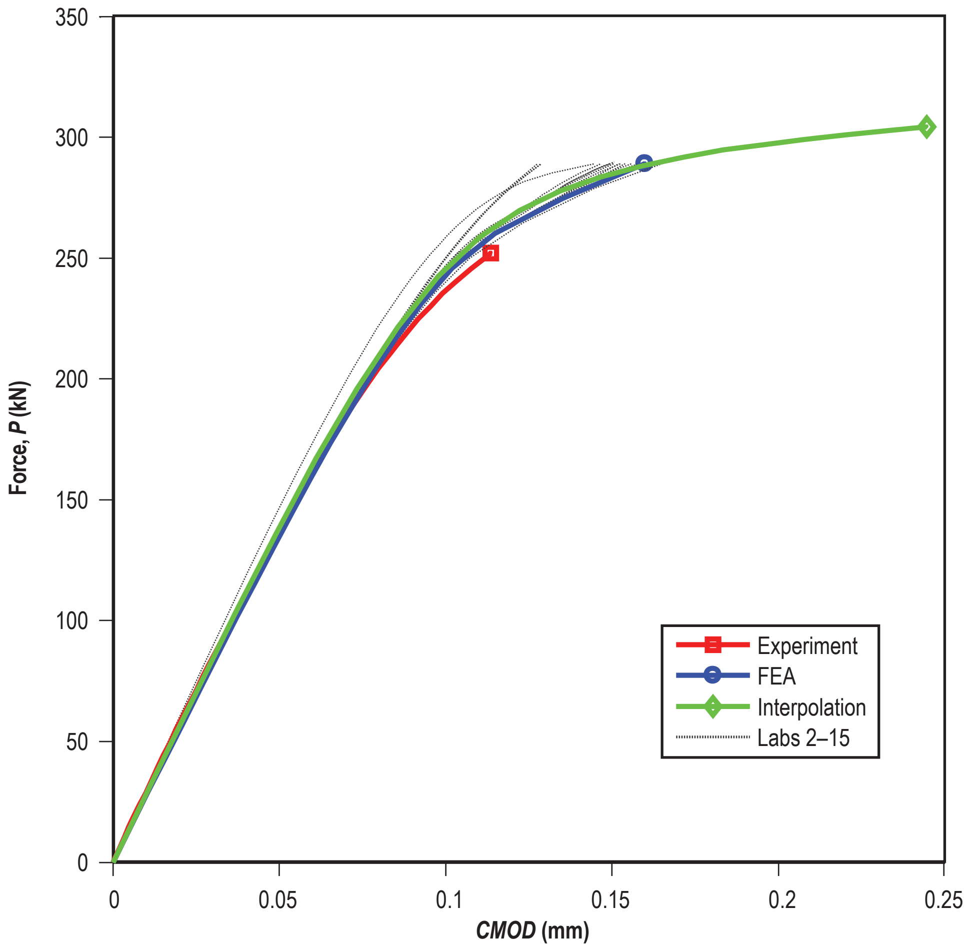

Figure 34. Interpolation, FEM, and RR participant results compared to experimental force versus *CMOD* response.

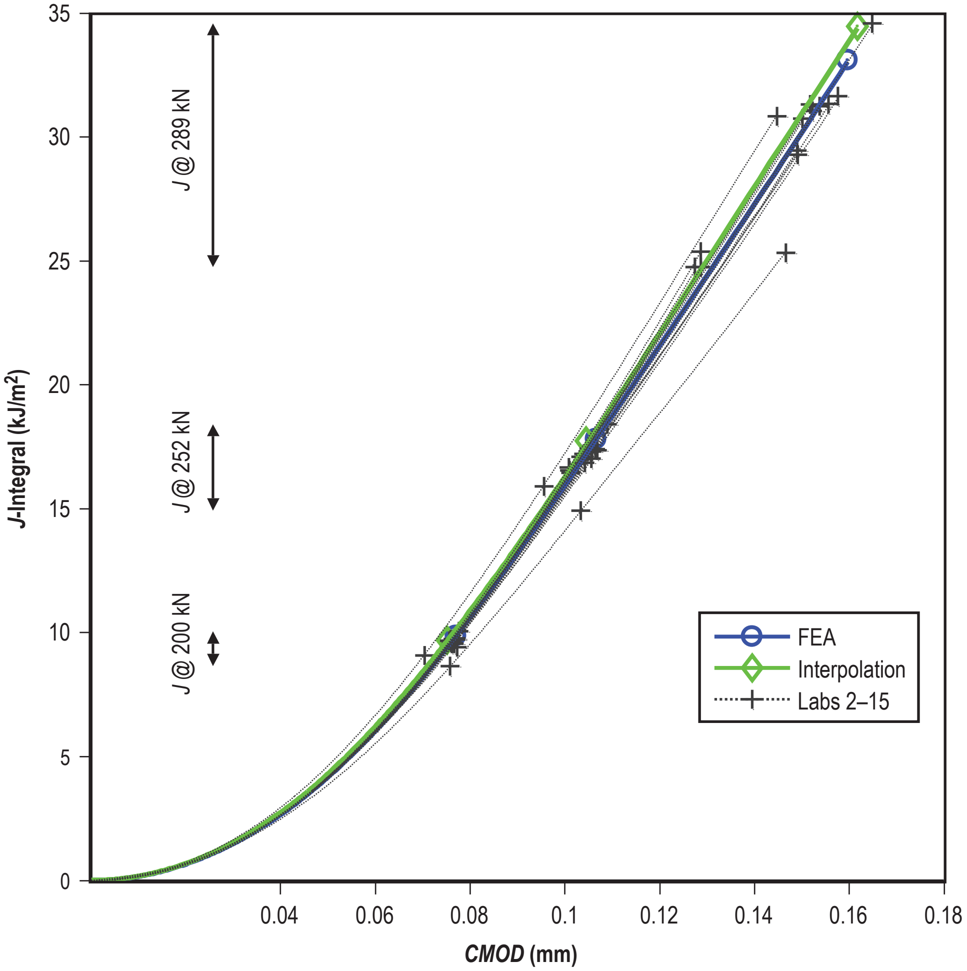

Figure 35. Comparison of interpolation, FEM, and RR participant results for J ($\phi = 17°$) versus *CMOD*.

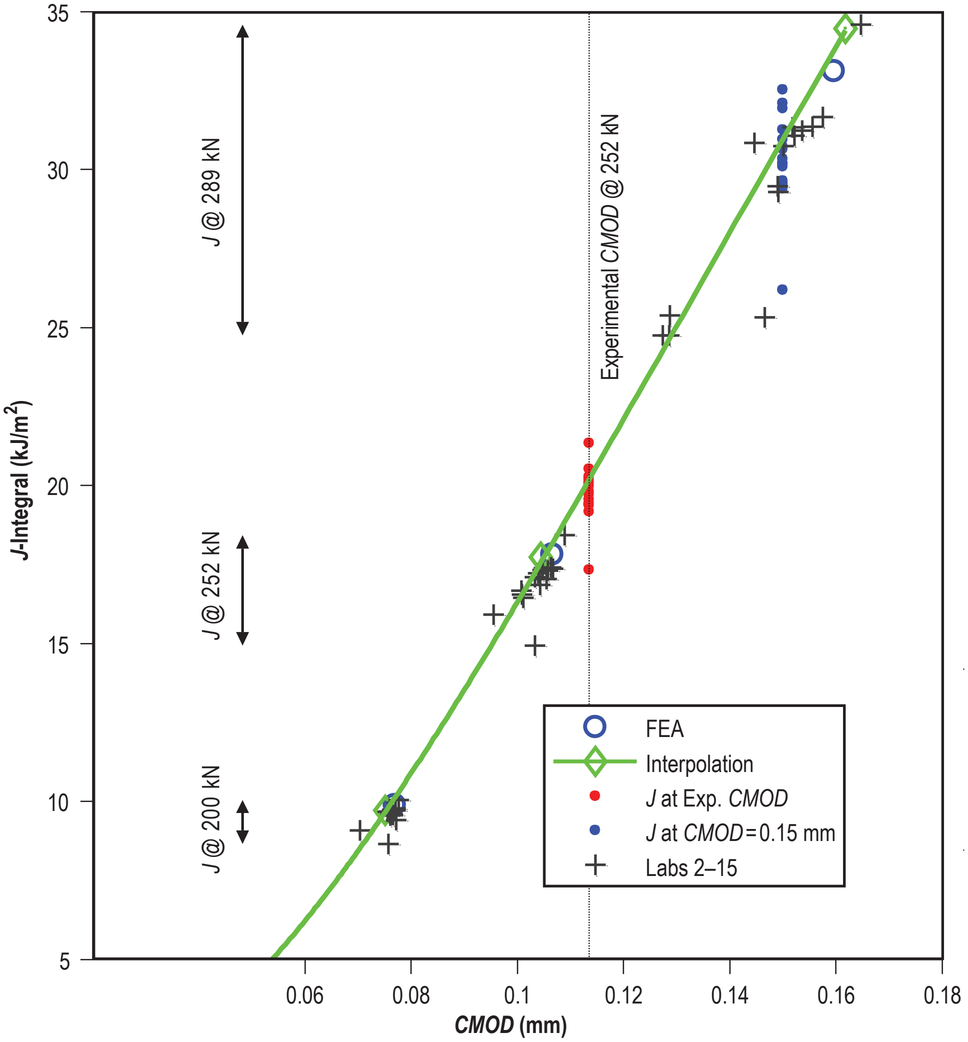

Figure 36. Additional comparison of interpolation, FEM, and RR participant results for $J(\phi = 17°)$ versus *CMOD*.

4. CONCLUSIONS

This set of elastic-plastic surface crack solutions and the interpolation methodologies developed to sew them together into a complete, functional space represents a significant bridge for the practicing engineer toward commonplace assessment of surface cracks by the *J*-integral. This is particularly true for the case of experimental evaluation of surface crack performance. The evaluation of fracture toughness in the elastic-plastic regime continues to lag significantly behind linear-elastic methods in implementation experimentally, even for common 2D geometries such as the C(T) specimen, despite the advantages in flexibility and breadth of information elastic-plastic methods reveal. Surface crack toughness testing can provide the most direct measure of material performance in structurally representative configurations; yet, the detailed working knowledge of finite element modeling required to properly assess a surface crack test in the elastic-plastic regime (as most are) has kept surface crack toughness testing reserved mainly as a domain for the specialist. The costs in modeling time and software infrastructure are largely prohibitive for most experimental labs. The interpolation methodology described herein and solution space provided in the appendices represent a new evolutional step in tools for the analyst and experimentalist alike.

Significant effort has been expended to ensure the reliability of this new tool. The authors have verified the solutions and the interpolation method through several techniques. The linear-elastic *J*-integral solutions were shown to be very similar to the Newman-Raju solutions. Domain convergence for the elastic-plastic *J*-integral values at the final load step was demonstrated for the complete set of solutions at all crack front locations. Twenty-five benchmark FEMs were created purposefully exploiting gaps in the geometry and material solution matrices to test the effectiveness of the interpolation method. The interpolated solutions were able to predict the benchmark *J*-integral and reaction force solutions for a given $CMOD$ value to within a few percent. The interpolation method was also used to estimate a solution for an interlaboratory round robin problem, and the interpolated solution had excellent agreement with the multiple laboratory results. The results of these studies indicate that the authors' surface crack solution set and interpolation method are sufficiently accurate to provide easily obtained and useful solutions for the *J*-integral and P-$CMOD$ response.

There remain a number of refinements and extensions to this work that would be equally valuable. The most obvious extension is to develop a similar solution space for surface cracks in flat plates subjected to a bending stress boundary condition. This is feasible with much of the same framework used to create the tension case. Within the existing tension space there are opportunities to fill gaps in the geometric or material variables to improve interpolation errors or to implement more sophisticated interpolation schemes. This may be a warranted investigation prior to developing the bending solutions. The solution set provides an excellent opportunity to investigate general surface crack behavior such as refining surface crack deformation limits in LEFM and EPFM, developing a robust predictor of surface crack tearing location in ϕ, or extrapolating solutions to higher deformation levels. Despite the many possibilities, the most hopeful outcome for the authors is adoption in the experimental community. Perhaps these solutions will eventually provide an impact similar to the equations of Newman and Raju.

APPENDIX A—WIDTH EFFECTS SUBSTUDY

A substudy was conducted to investigate the effects of increasing $W/2c$ on the J-integral solutions and the force versus $CMOD$ response. The same model used in the normalization case study was utilized here with $W/2c=5$, $L/W=2$, $a/B=0.6$, $a/c=0.6$, $n=6$, $\sigma_{ys}=1$, $\nu=0.3$, and $E/\sigma_{ys}=300$. Two additional FEMs were created and analyzed with $W/2c=10$ and 20 with all other geometric proportions and properties the same. In addition, interpolated solutions were estimated for all three plate geometries. Figure 37 illustrates the normalized far-field stress, σ_n, versus $CMOD_n$ for all the FEMs and interpolated solutions. All of the σ_n versus $CMOD_n$ interpolated solutions are identical and match the $W/2c=5$ FEM result, and all of the responses are essentially the same in the linear-elastic region. The wider FEM plate results require a slightly higher far-field stress to reach a given $CMOD_n$ value in the nonlinear region. Figure 38 shows the figure 37 results with the stress axis converted to applied force, P. As expected, the interpolated result and the $W/2c=5$ FEM result match exactly. The interpolated solutions of the wider plate results are a reasonable match in the linear regime, but the interpolated results slightly underpredict the force for a given $CMOD_n$ in the nonlinear region. Matching the P versus $CMOD_n$ response is not required to interpolate to a J-integral solution, but is important for a comparison to P versus $CMOD$ experimental results. Figure 39 illustrates that the $J_n(\phi=90°)$ versus $CMOD_n$ results are almost identical for the FEA and interpolated solutions showing that the J-integral as a function of $CMOD$ is essentially invariant to increasing plate width. The maximum $CMOD_n$ for the $W/2c=20$ FEM is shown as a vertical dashed line in figure 39, and figure 40 shows J_n versus ϕ results at this $CMOD_n$ level for all the FEA and interpolated solutions. Again, the J_n versus ϕ results are demonstrated to be insensitive to plate width for a given $CMOD_n$ level, and the interpolated solutions are an excellent match to the FEA solutions.

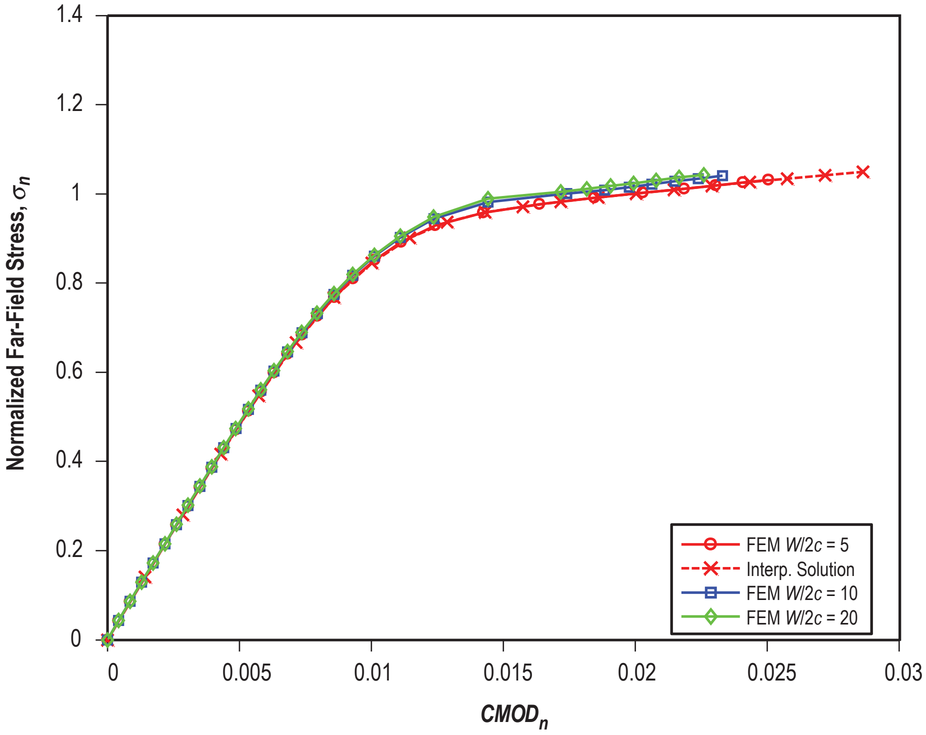

Figure 37. Comparison of the σ_n versus $CMOD_n$ results for geometries with differing $2c/W$.

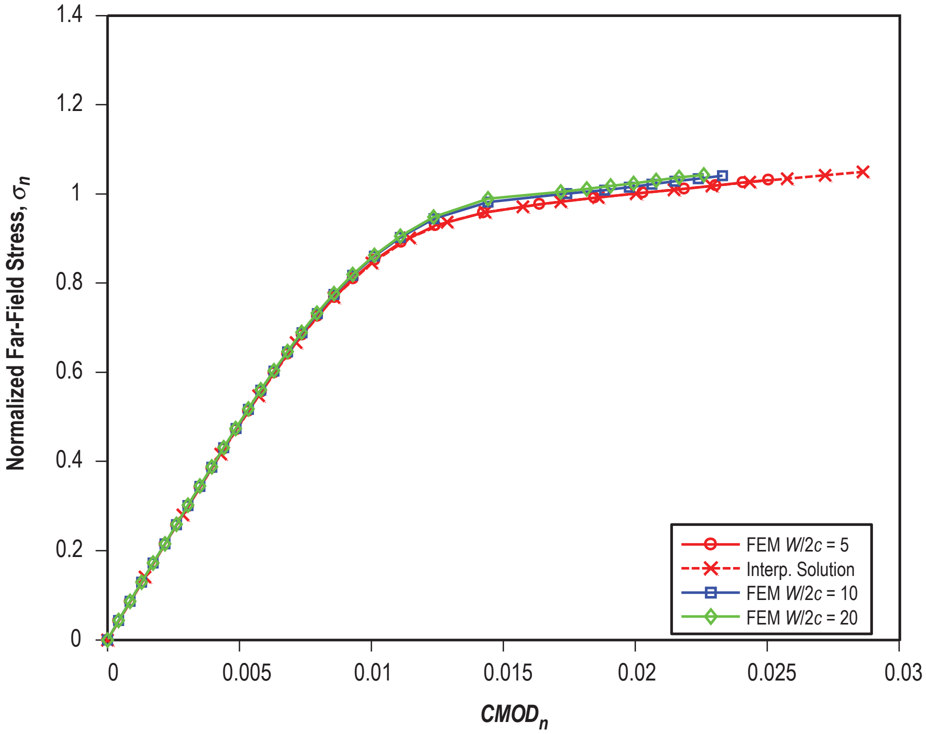

Figure 38. Comparison of the P versus $CMOD_n$ results for geometries with differing $2c/W$.

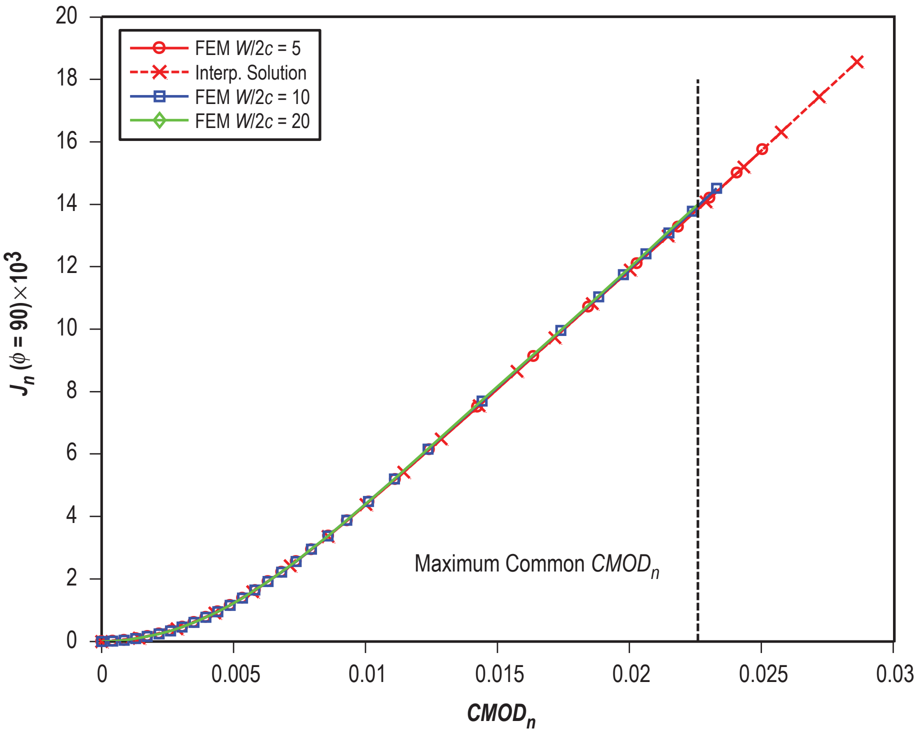

Figure 39. Comparison of the $J_n(\phi = 90°)$ versus $CMOD_n$ results for geometries with differing $2c/W$.

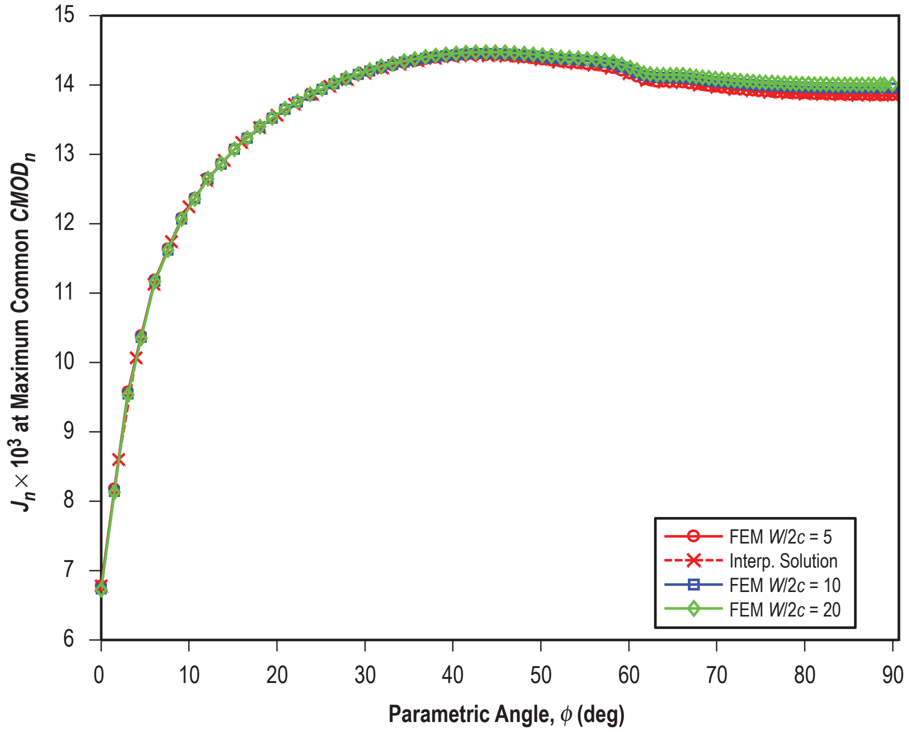

Figure 40. Comparison of the J_n versus ϕ results for geometries with differing $2c/W$ at the maximum $CMOD$ value of the $2c/W = 20$ FEM.

APPENDIX B—COLLECTION OF BENCHMARK MODELS COMPARISON PLOTS

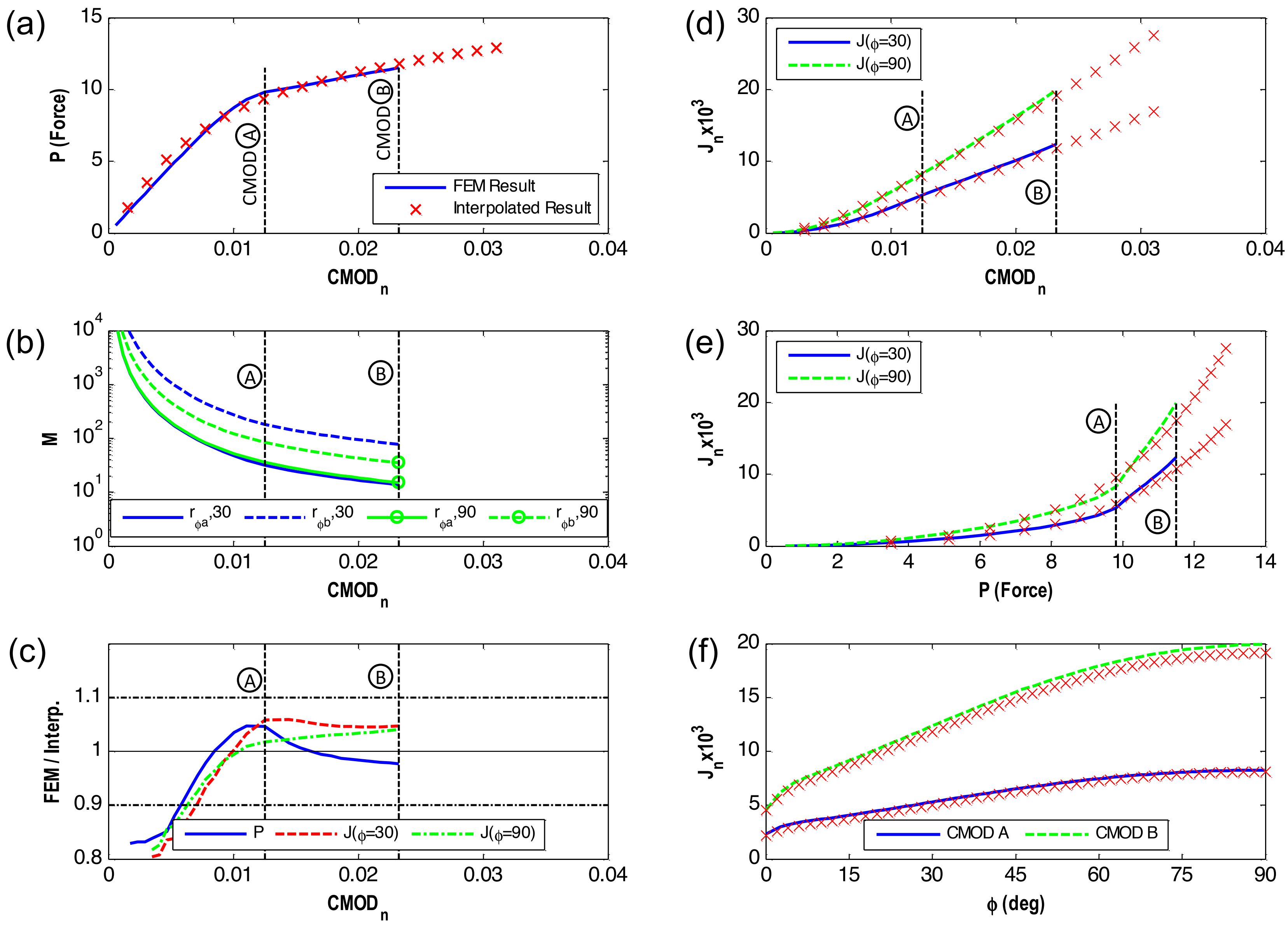

Figure B1. Comparison of benchmark model No. 1 FEM results and interpolated results for (a) P versus $CMOD_n$, (b) M versus $CMOD_n$, (c) benchmark FEM/interpolated results versus $CMOD_n$, (d) J_n versus $CMOD_n$ at $\phi = 30°$ and $90°$, (e) J_n versus P at $\phi = 30°$ and $90°$, and (f) J_n versus ϕ for $CMOD_n$ values A and B.

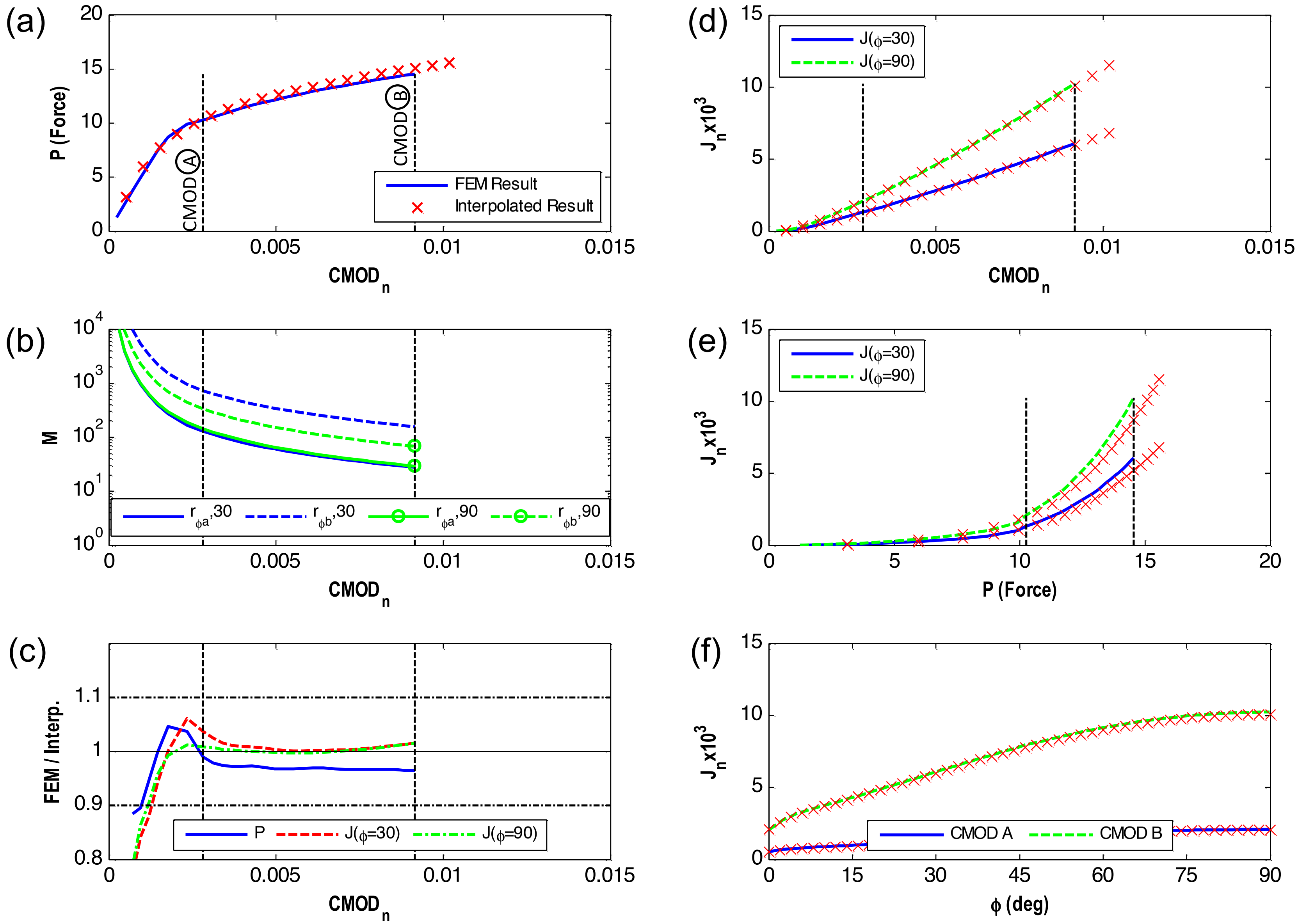

Figure B2. Comparison of benchmark model No. 2 FEM results and interpolated results for (a) P versus $CMOD_n$ (b) M versus $CMOD_n$, (c) benchmark FEM/interpolated results versus $CMOD_n$, (d) J_n versus $CMOD_n$ at $\phi = 30°$ and $90°$, (e) J_n versus P at $\phi = 30°$ and $90°$, and (f) J_n versus ϕ for $CMOD_n$ values A and B..

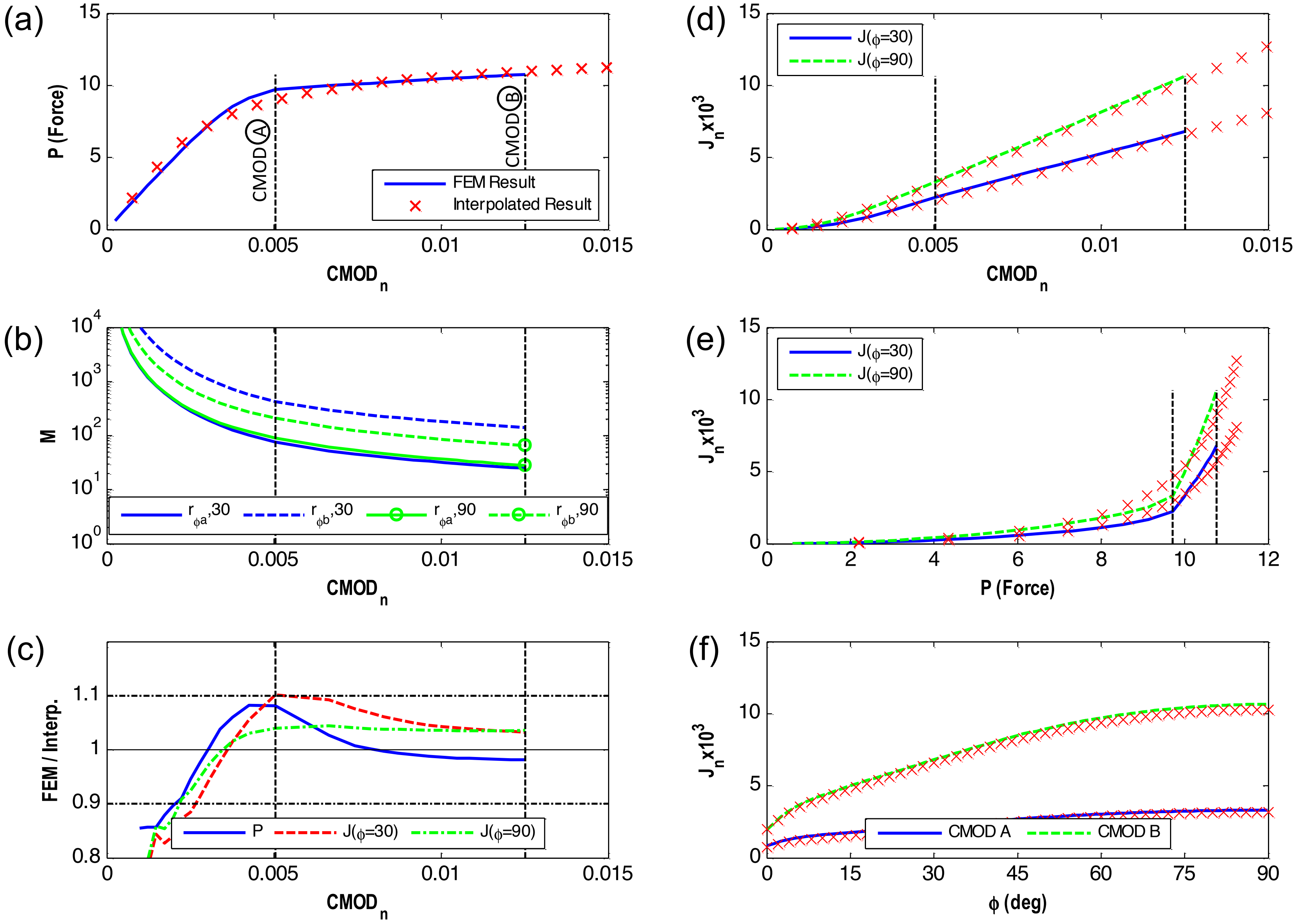

Figure B3. Comparison of benchmark model No. 3 FEM results and interpolated results for (a) P versus $CMOD_n$ (b) M versus $CMOD_n$, (c) benchmark FEM/interpolated results versus $CMOD_n$, (d) J_n versus $CMOD_n$ at $\phi = 30°$ and $90°$, (e) J_n versus P at $\phi = 30°$ and $90°$, and (f) J_n versus ϕ for $CMOD_n$ values A and B.

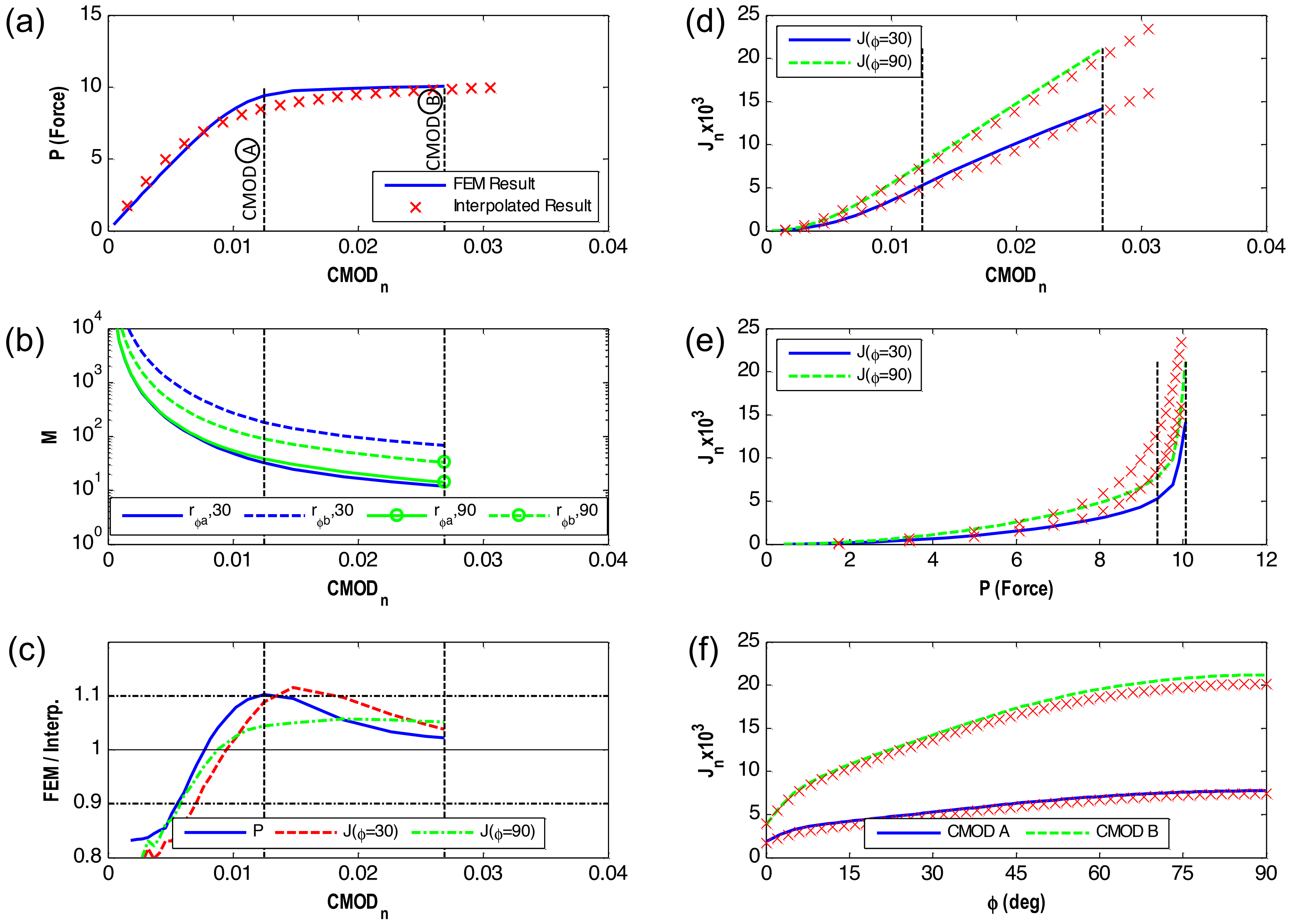

Figure B4. Comparison of benchmark model No. 4 FEM results and interpolated results for (a) P versus $CMOD_n$ (b) M versus $CMOD_n$, (c) benchmark FEM/interpolated results versus $CMOD_n$, (d) J_n versus $CMOD_n$ at $\phi = 30°$ and 90°, (e) J_n versus P at $\phi = 30°$ and 90°, and (f) J_n versus ϕ for $CMOD_n$ values A and B.

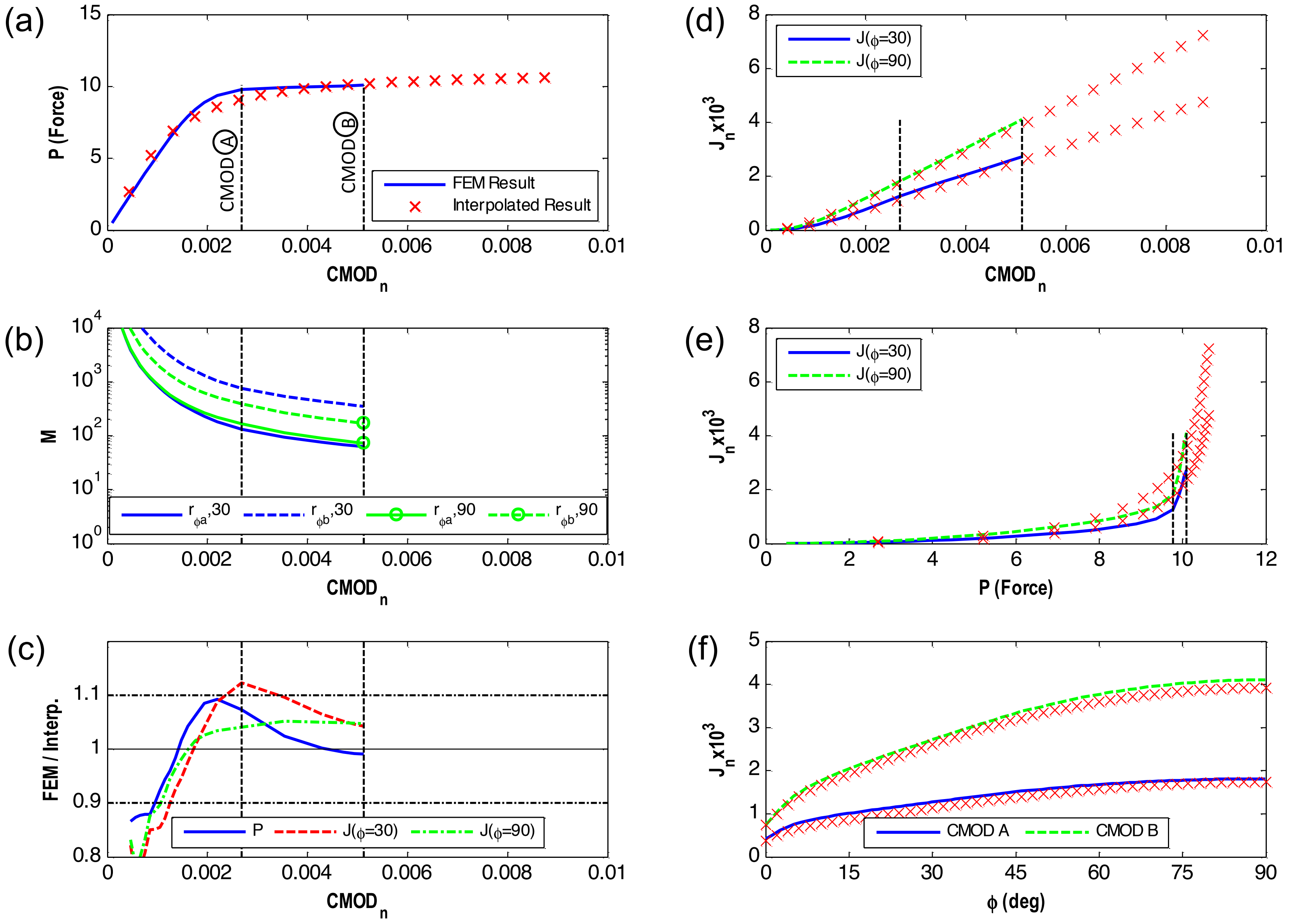

Figure B5. Comparison of benchmark model No. 5 FEM results and interpolated results for (a) P versus $CMOD_n$ (b) M versus $CMOD_n$, (c) benchmark FEM/interpolated results versus $CMOD_n$, (d) J_n versus $CMOD_n$ at $\phi = 30°$ and 90°, (e) J_n versus P at $\phi = 30°$ and 90°, and (f) J_n versus ϕ for $CMOD_n$ values A and B.

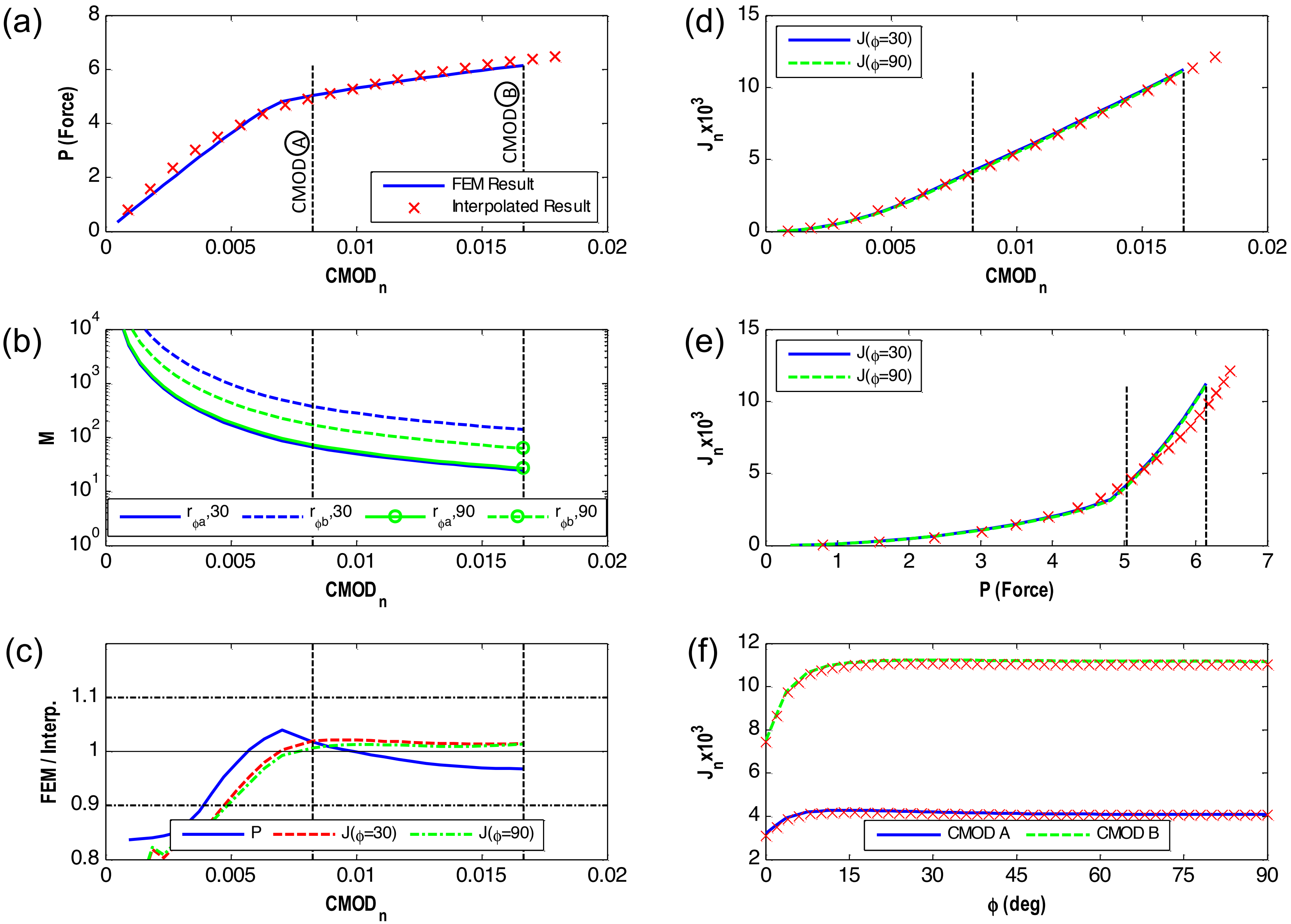

Figure B6. Comparison of benchmark model No. 6 FEM results and interpolated results for (a) P versus $CMOD_n$ (b) M versus $CMOD_n$, (c) benchmark FEM/interpolated results versus $CMOD_n$, (d) J_n versus $CMOD_n$ at $\phi = 30°$ and $90°$, (e) J_n versus P at $\phi = 30°$ and $90°$, and (f) J_n versus ϕ for $CMOD_n$ values A and B.

Fig.

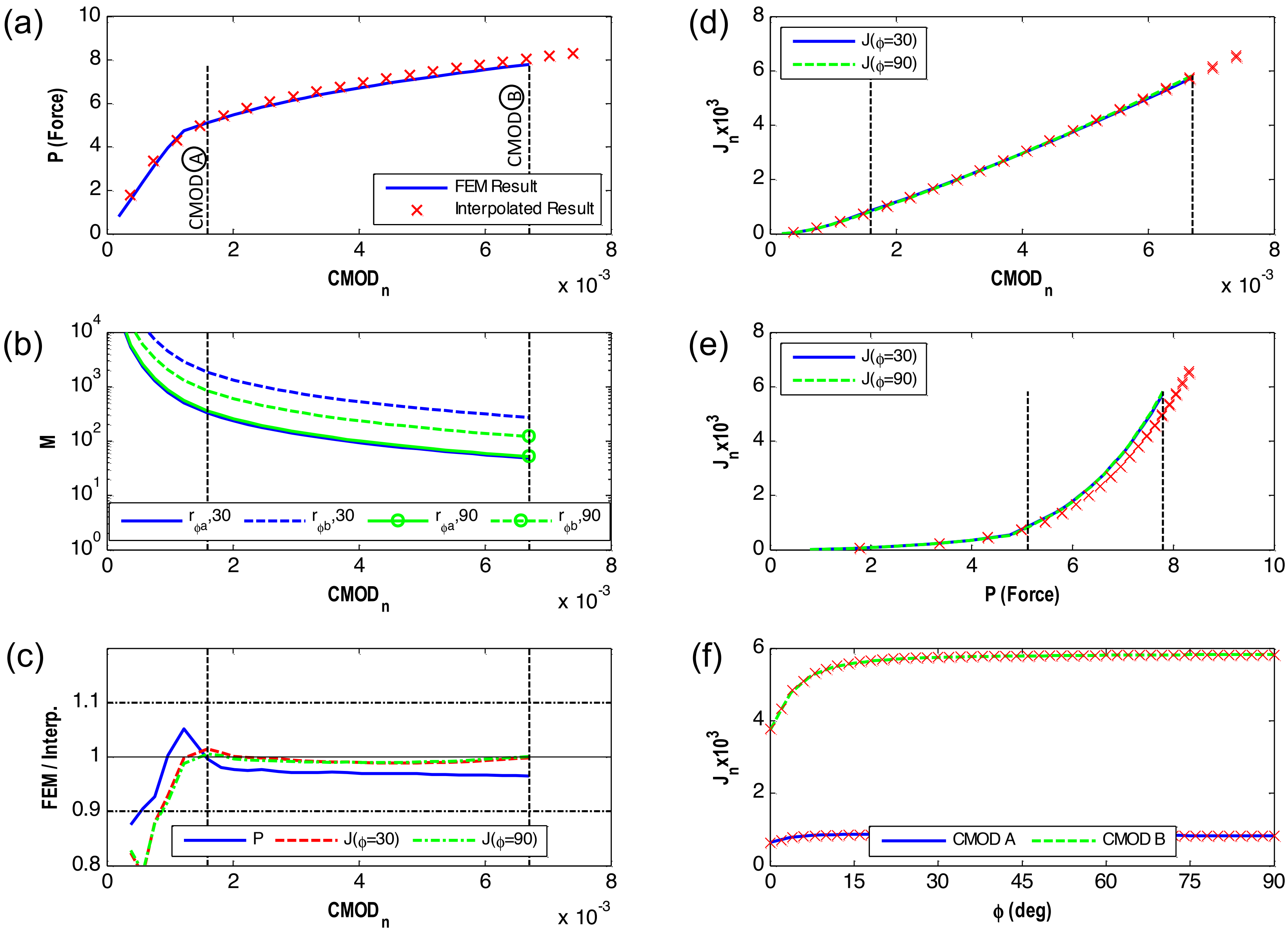

Figure B7. Comparison of benchmark model No. 7 FEM results and interpolated results for (a) P versus $CMOD_n$ (b) M versus $CMOD_n$, (c) benchmark FEM/interpolated results versus $CMOD_n$, (d) J_n versus $CMOD_n$ at $\phi = 30°$ and 90°, (e) J_n versus P at $\phi = 30°$ and 90°, and (f) J_n versus ϕ for $CMOD_n$ values A and B.

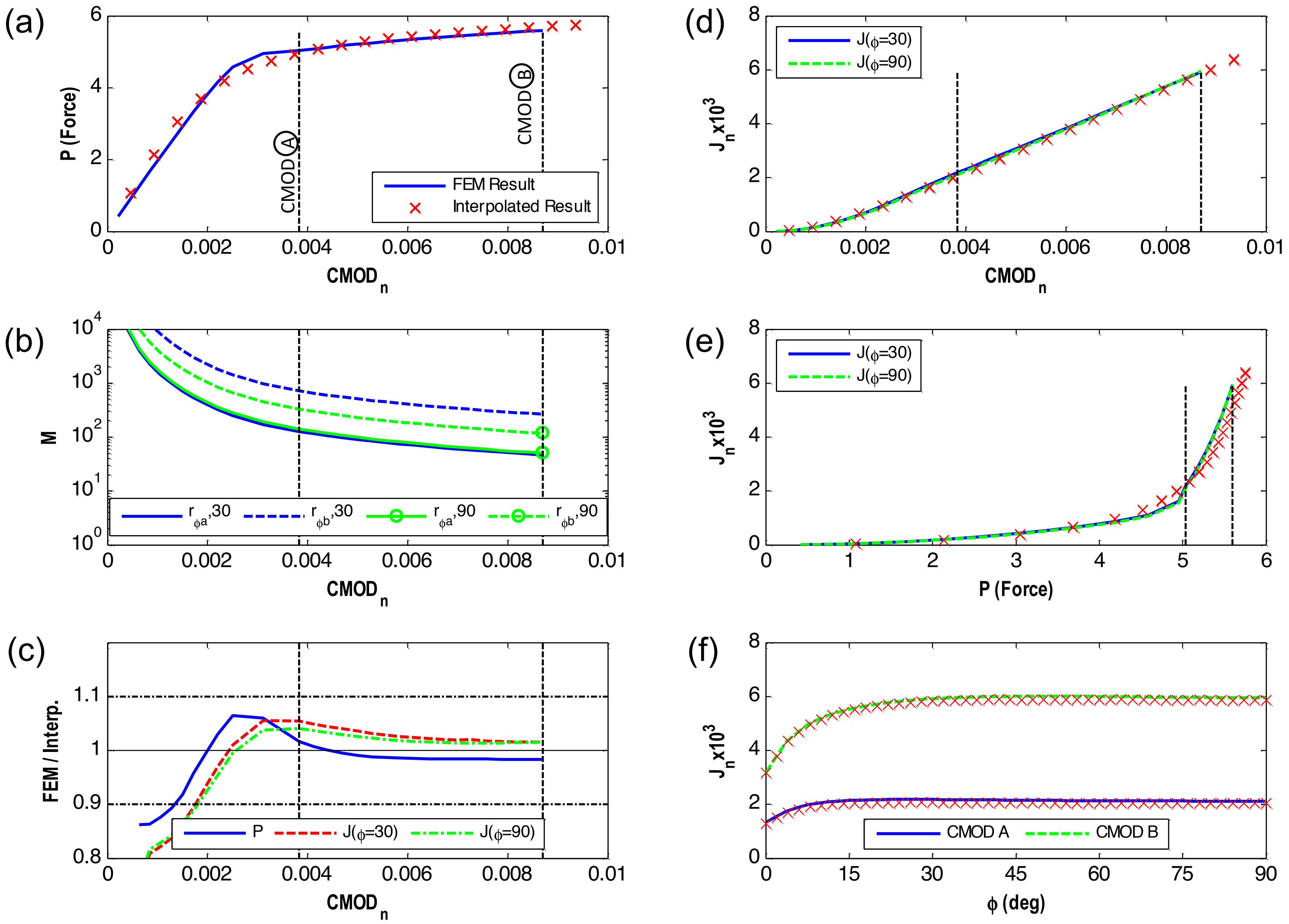

Figure B8. Comparison of benchmark model No. 8 FEM results and interpolated results for (a) P versus $CMOD_n$ (b) M versus $CMOD_n$, (c) benchmark FEM/interpolated results versus $CMOD_n$, (d) J_n versus $CMOD_n$ at $\phi = 30°$ and 90°, (e) J_n versus P at $\phi = 30°$ and 90°, and (f) J_n versus ϕ for $CMOD_n$ values A and B..

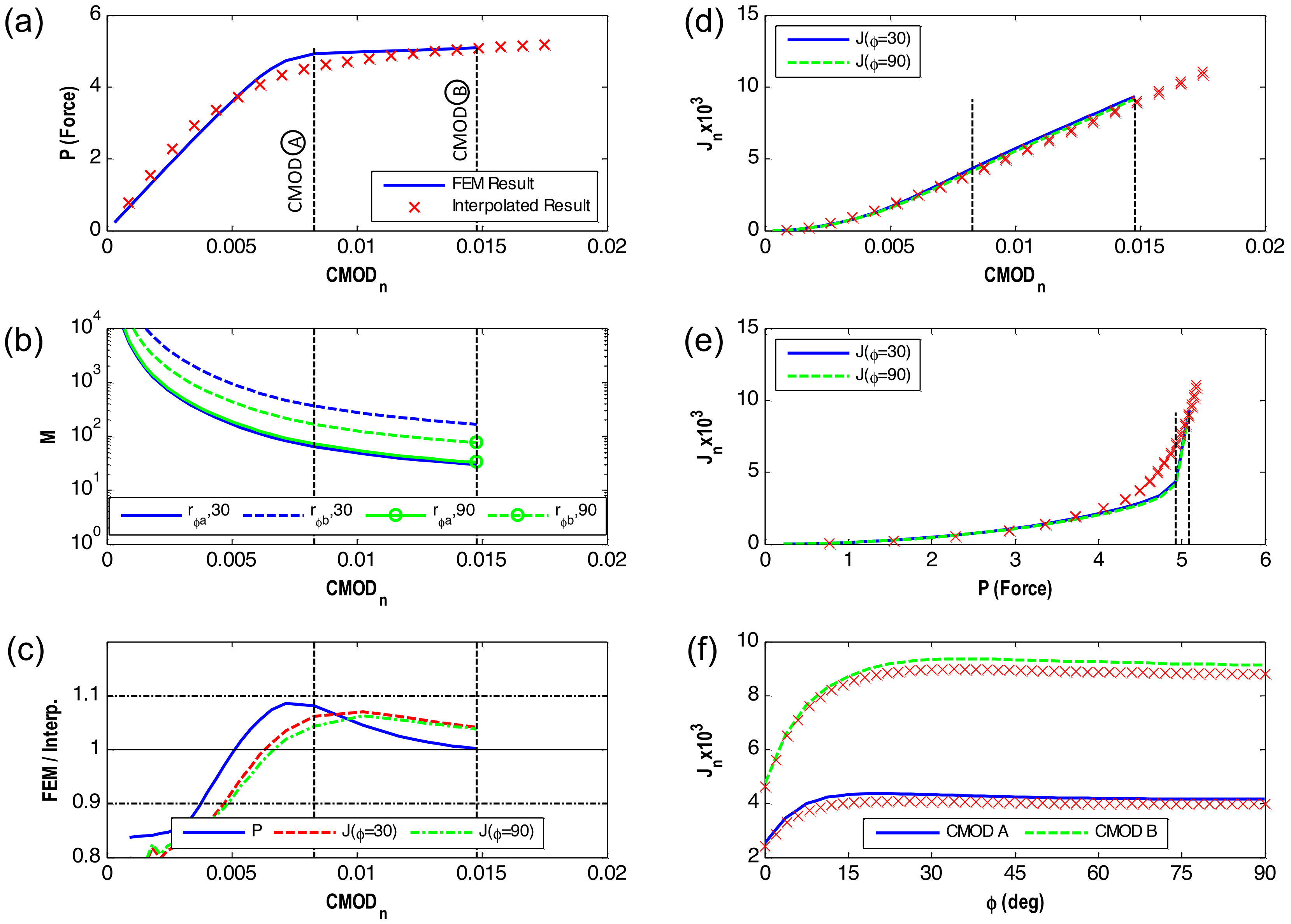

Figure B9. Comparison of benchmark model No. 9 FEM results and interpolated results for (a) P versus $CMOD_n$ (b) M versus $CMOD_n$, (c) benchmark FEM/interpolated results versus $CMOD_n$, (d) J_n versus $CMOD_n$ at $\phi = 30°$ and $90°$, (e) J_n versus P at $\phi = 30°$ and $90°$, and (f) J_n versus ϕ for $CMOD_n$ values A and B.

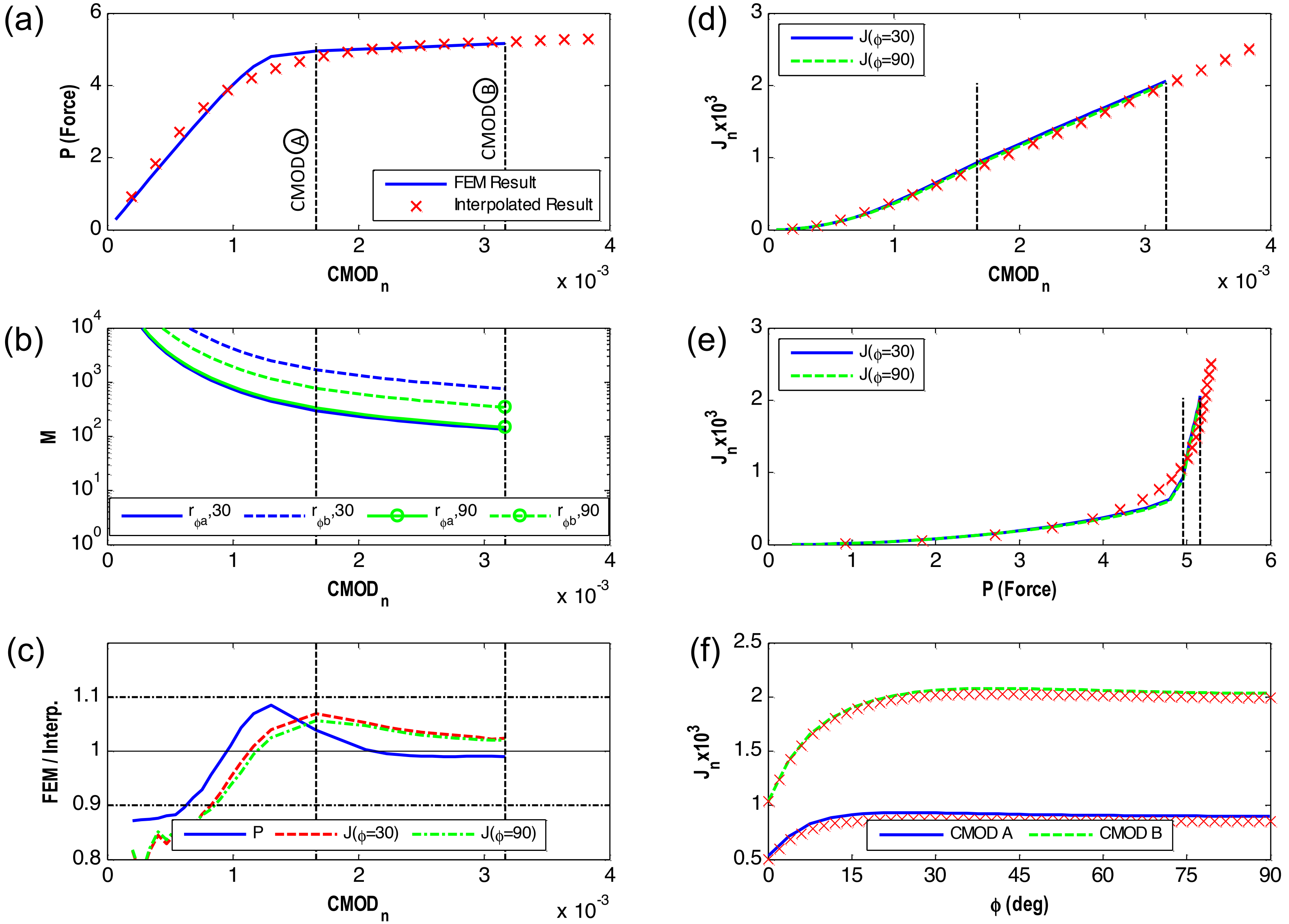

Figure B10. Comparison of benchmark model No. 10 FEM results and interpolated results for (a) P versus $CMOD_n$ (b) M versus $CMOD_n$, (c) benchmark FEM/interpolated results versus $CMOD_n$, (d) J_n versus $CMOD_n$ at $\phi = 30°$ and 90°, (e) J_n versus P at $\phi = 30°$ and 90°, and (f) J_n versus ϕ for $CMOD_n$ values A and B.

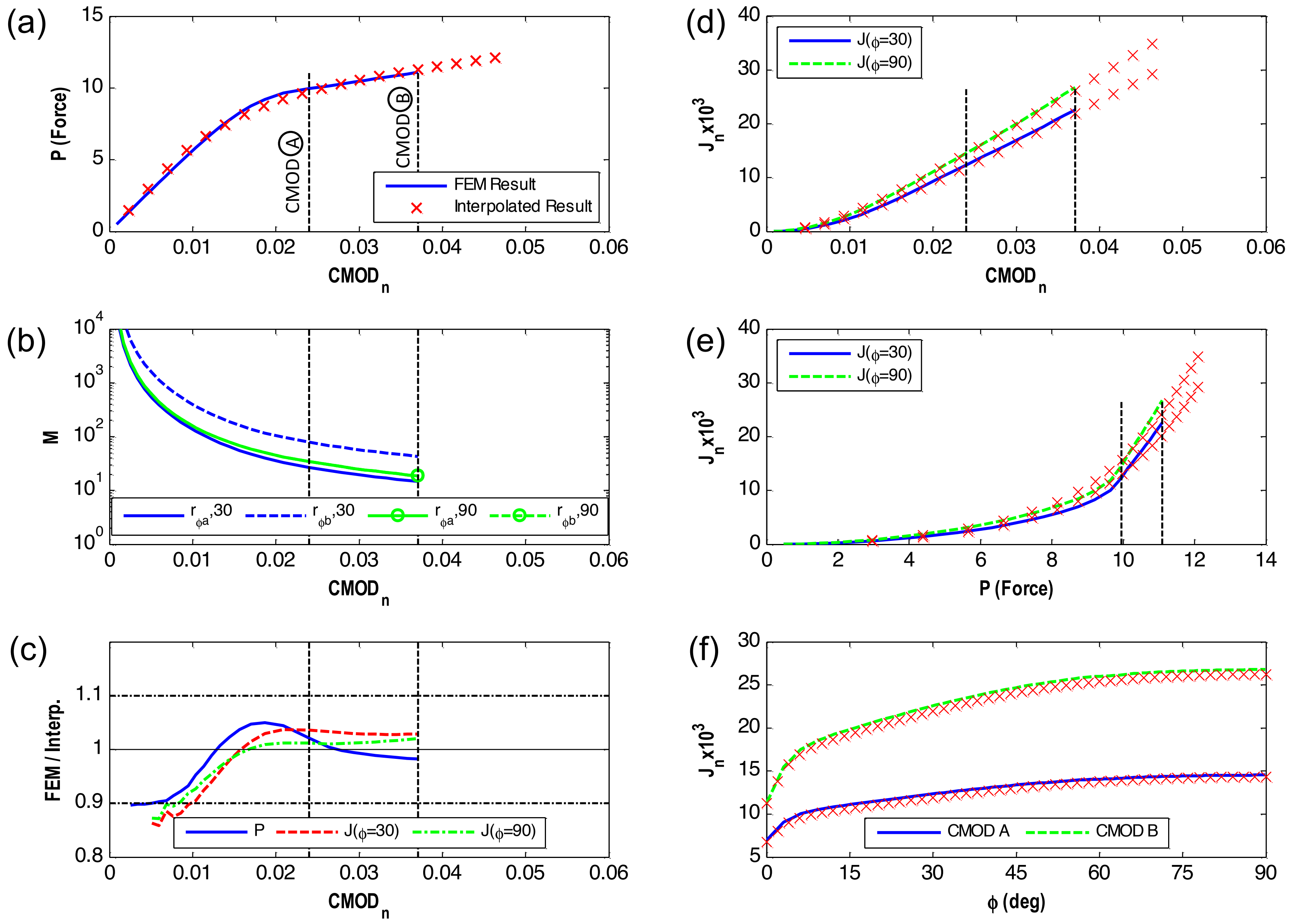

Figure B11. Comparison of benchmark model No. 11 FEM results and interpolated results for (a) P versus $CMOD_n$ (b) M versus $CMOD_n$, (c) benchmark FEM/interpolated results versus $CMOD_n$, (d) J_n versus $CMOD_n$ at $\phi = 30°$ and 90°, (e) J_n versus P at $\phi = 30°$ and 90°, and (f) J_n versus ϕ for $CMOD_n$ values A and B.

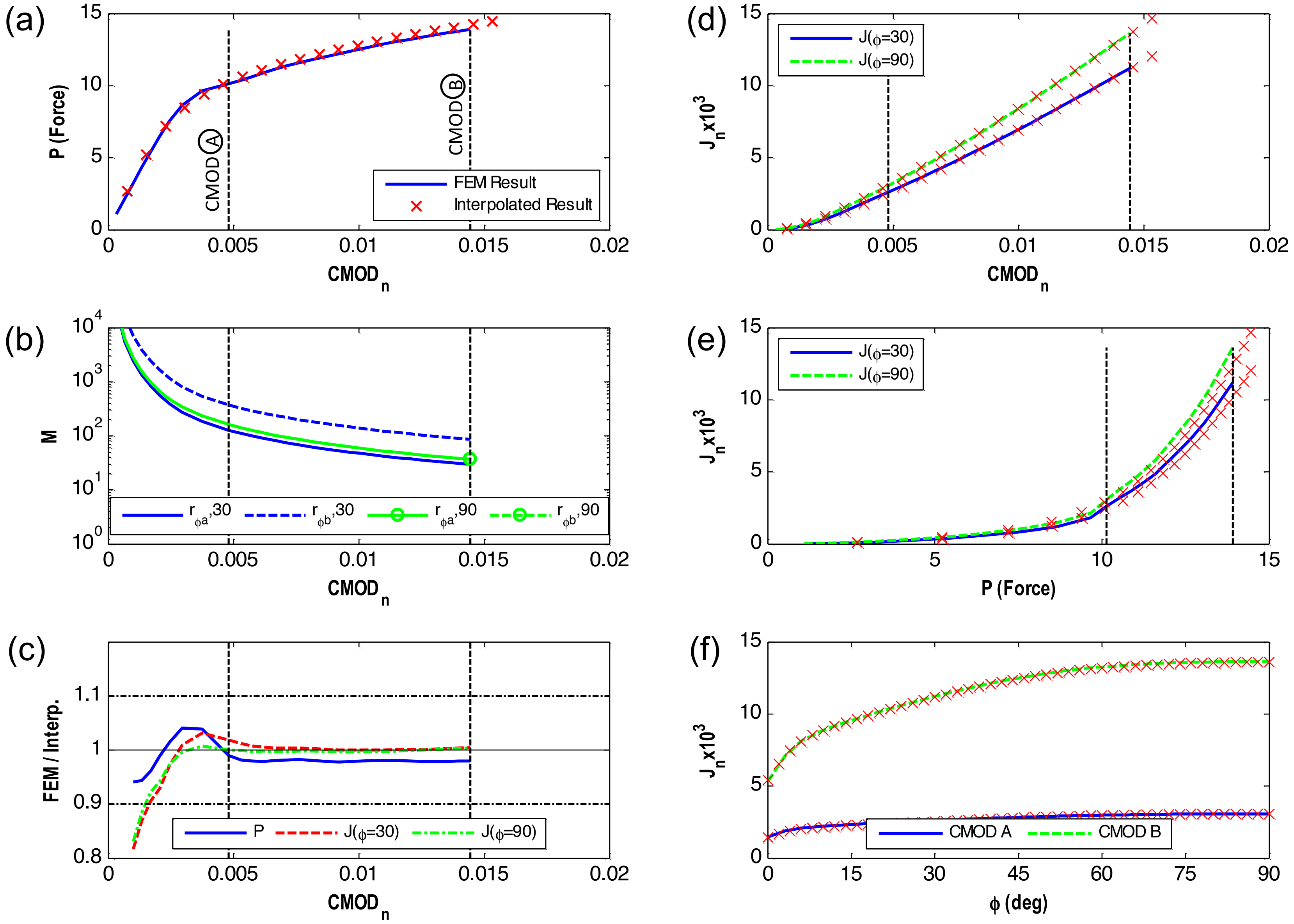

Figure B12. Comparison of benchmark model No. 12 FEM results and interpolated results for (a) P versus $CMOD_n$ (b) M versus $CMOD_n$, (c) benchmark FEM/interpolated results versus $CMOD_n$, (d) J_n versus $CMOD_n$ at $\phi = 30°$ and 90°, (e) J_n versus P at $\phi = 30°$ and 90°, and (f) J_n versus ϕ for $CMOD_n$ values A and B.

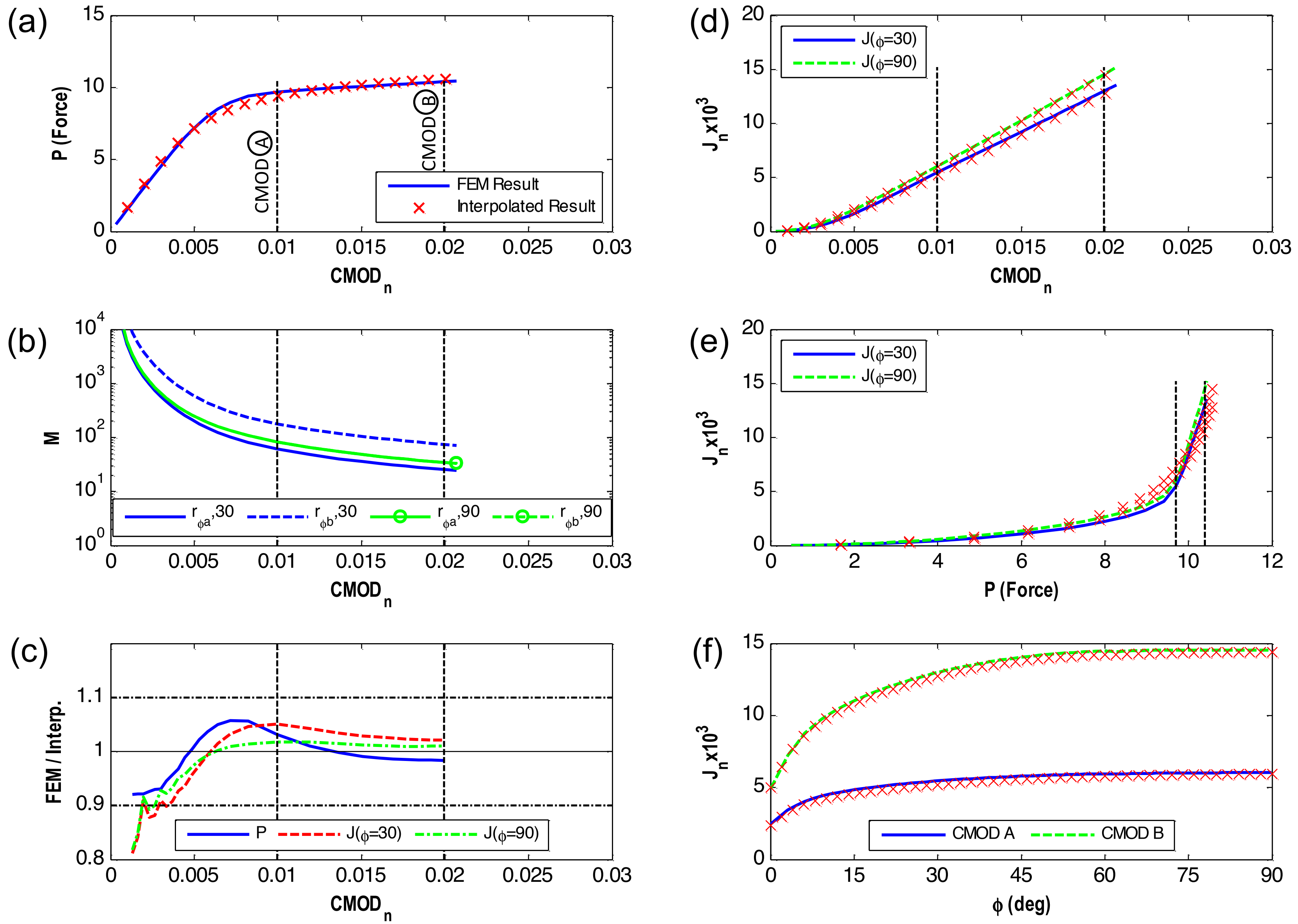

Figure B13. Comparison of benchmark model No. 13 FEM results and interpolated results for (a) P versus $CMOD_n$ (b) M versus $CMOD_n$, (c) benchmark FEM/interpolated results versus $CMOD_n$, (d) J_n versus $CMOD_n$ at $\phi = 30°$ and 90°, (e) J_n versus P at $\phi = 30°$ and 90°, and (f) J_n versus ϕ for $CMOD_n$ values A and B.

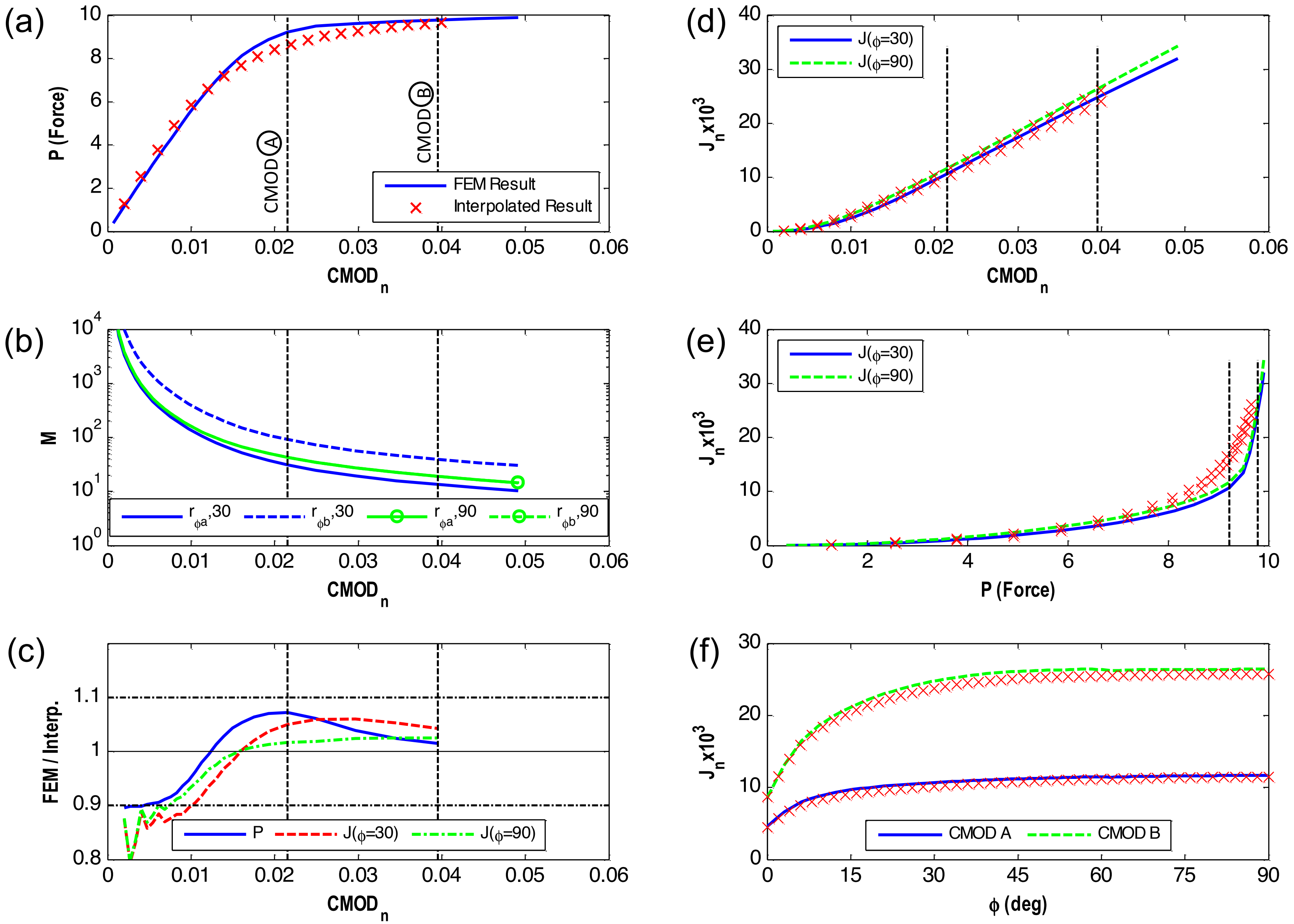

Figure B14. Comparison of benchmark model No. 14 FEM results and interpolated results for (a) P versus $CMOD_n$ (b) M versus $CMOD_n$, (c) benchmark FEM/interpolated results versus $CMOD_n$, (d) J_n versus $CMOD_n$ at $\phi = 30°$ and 90°, (e) J_n versus P at $\phi = 30°$ and 90°, and (f) J_n versus ϕ for $CMOD_n$ values A and B.

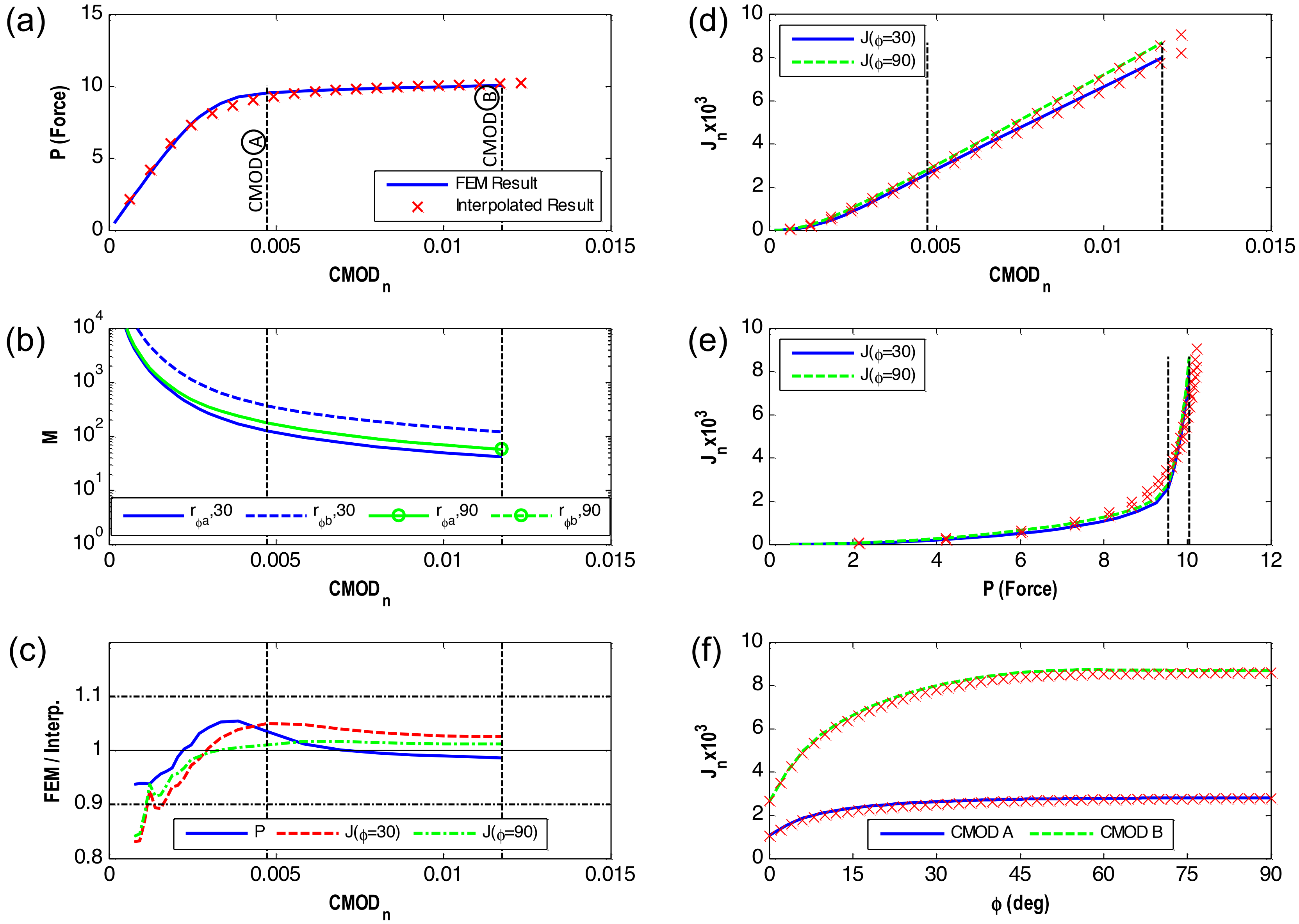

Figure B15. Comparison of benchmark model No. 15 FEM results and interpolated results for (a) P versus $CMOD_n$ (b) M versus $CMOD_n$, (c) benchmark FEM/interpolated results versus $CMOD_n$, (d) J_n versus $CMOD_n$ at $\phi = 30°$ and 90°, (e) J_n versus P at $\phi = 30°$ and 90°, and (f) J_n versus ϕ for $CMOD_n$ values A and B.

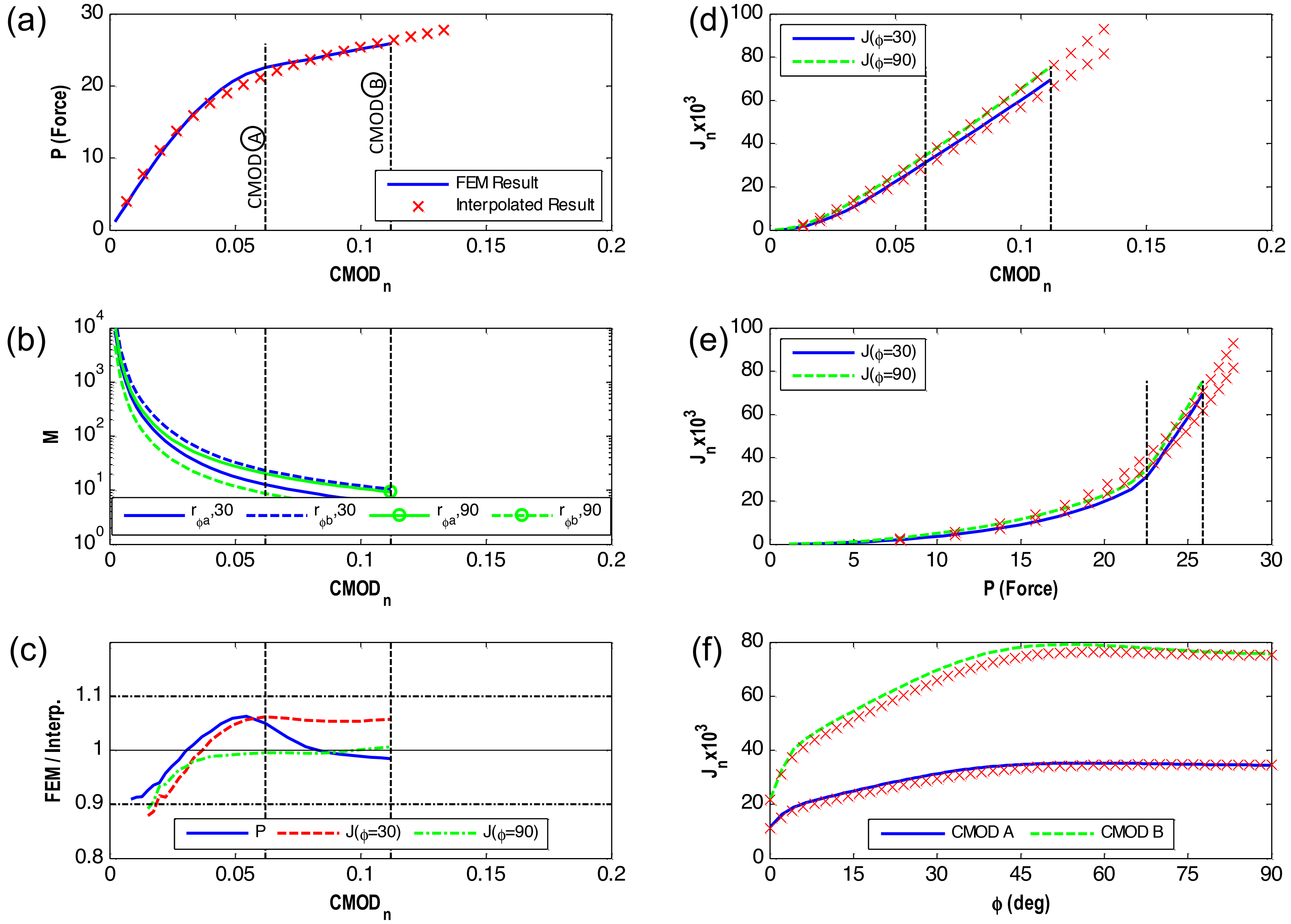

Figure B16. Comparison of benchmark model No. 16 FEM results and interpolated results for (a) P versus $CMOD_n$ (b) M versus $CMOD_n$, (c) benchmark FEM/interpolated results versus $CMOD_n$, (d) J_n versus $CMOD_n$ at $\phi = 30°$ and 90°, (e) J_n versus P at $\phi = 30°$ and 90°, and (f) J_n versus ϕ for $CMOD_n$ values A and B.

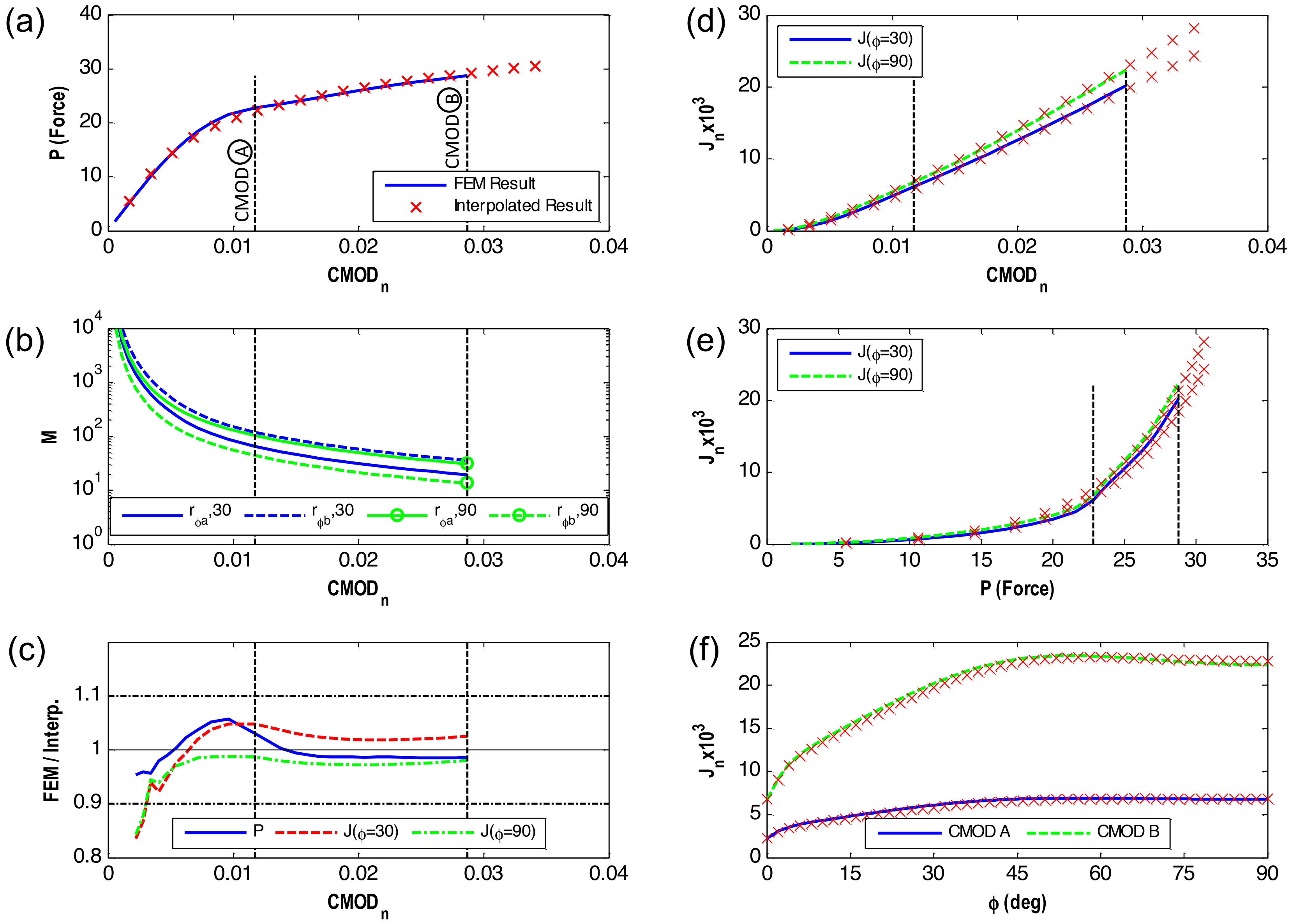

Figure B17. Comparison of benchmark model No. 17 FEM results and interpolated results for (a) P versus $CMOD_n$ (b) M versus $CMOD_n$, (c) benchmark FEM/interpolated results versus $CMOD_n$, (d) J_n versus $CMOD_n$ at $\phi = 30°$ and 90°, (e) J_n versus P at $\phi = 30°$ and 90°, and (f) J_n versus ϕ for $CMOD_n$ values A and B.

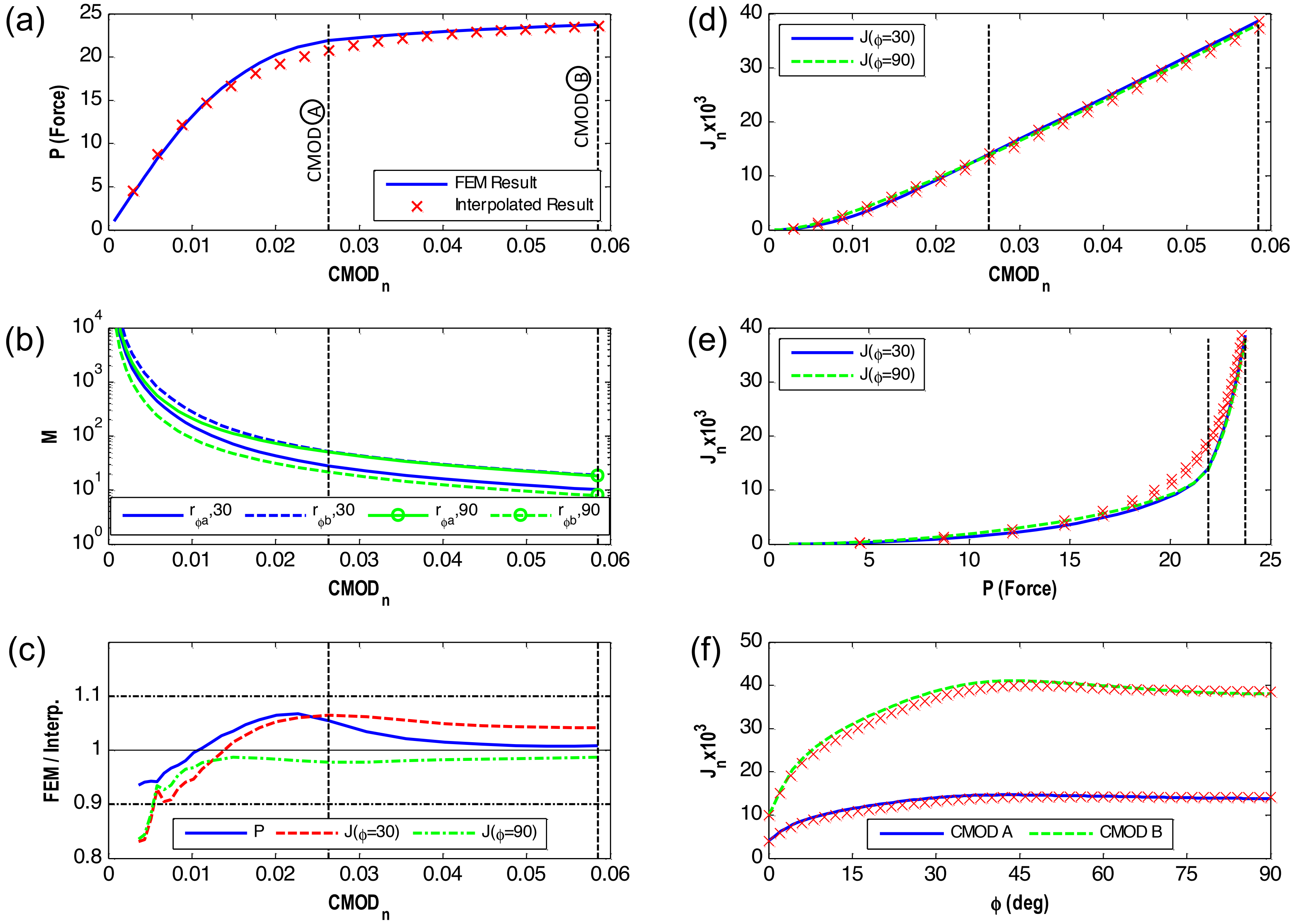

Figure B18. Comparison of benchmark model No. 18 FEM results and interpolated results for (a) P versus $CMOD_n$ (b) M versus $CMOD_n$, (c) benchmark FEM/interpolated results versus $CMOD_n$, (d) J_n versus $CMOD_n$ at $\phi = 30°$ and 90°, (e) J_n versus P at $\phi = 30°$ and 90°, and (f) J_n versus ϕ for $CMOD_n$ values A and B.

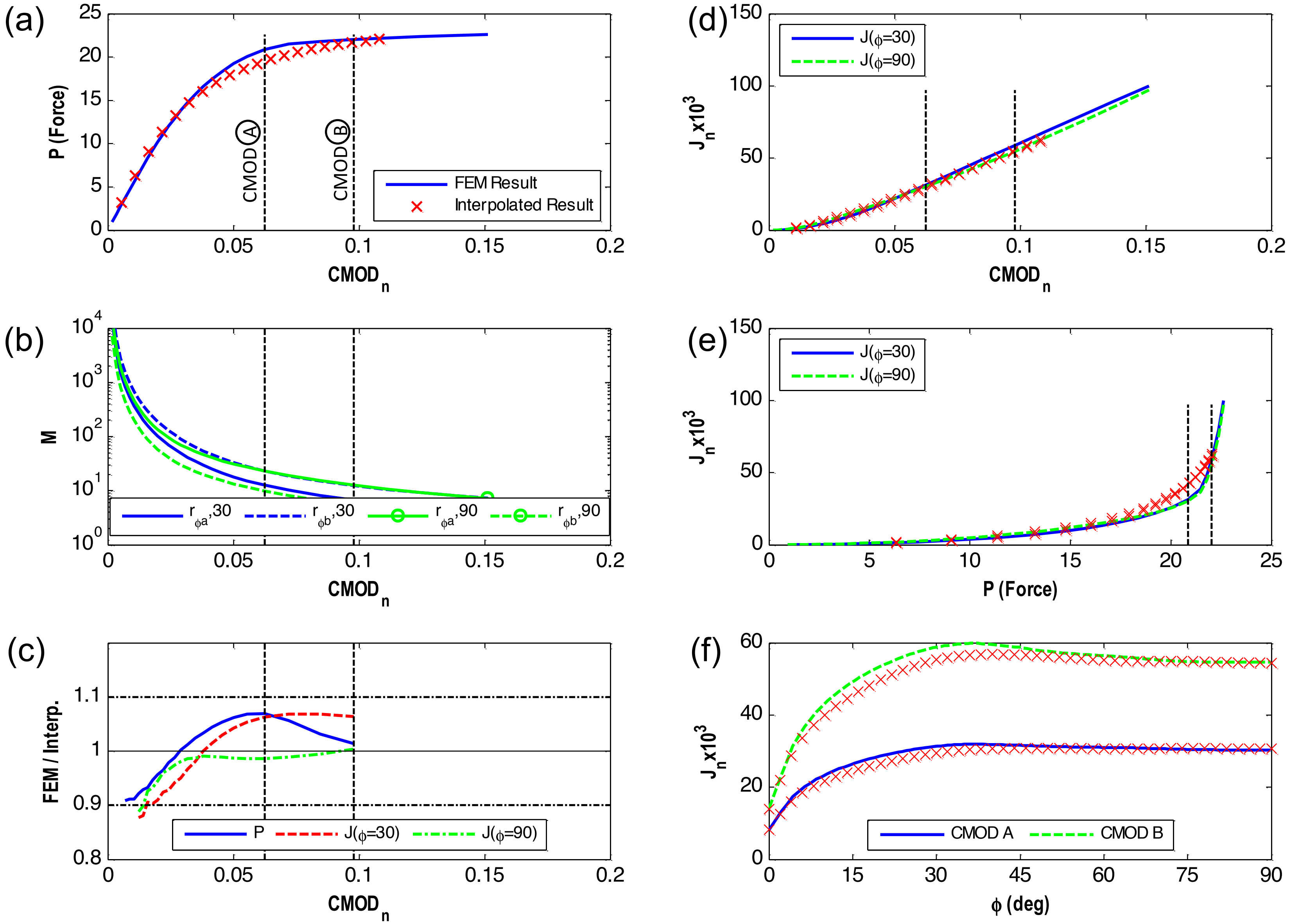

Figure B19. Comparison of benchmark model No. 19 FEM results and interpolated results for (a) P versus $CMOD_n$ (b) M versus $CMOD_n$, (c) benchmark FEM/interpolated results versus $CMOD_n$, (d) J_n versus $CMOD_n$ at $\phi = 30°$ and 90°, (e) J_n versus P at $\phi = 30°$ and 90°, and (f) J_n versus ϕ for $CMOD_n$ values A and B.

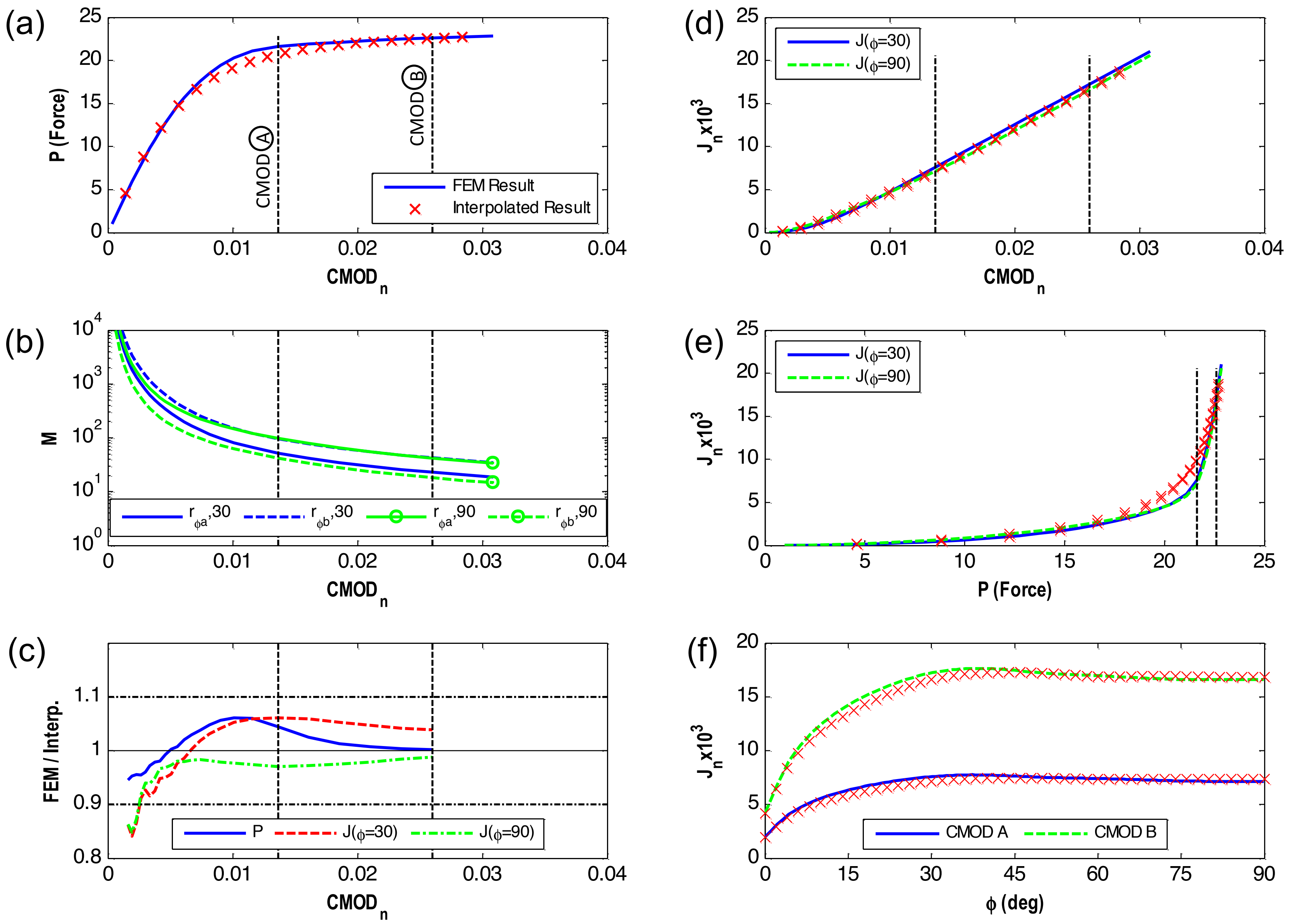

Figure B20. Comparison of benchmark model No. 20 FEM results and interpolated results for (a) P versus $CMOD_n$ (b) M versus $CMOD_n$, (c) benchmark FEM/interpolated results versus $CMOD_n$, (d) J_n versus $CMOD_n$ at $\phi = 30°$ and 90°, (e) J_n versus P at $\phi = 30°$ and 90°, and (f) J_n versus ϕ for $CMOD_n$ values A and B.

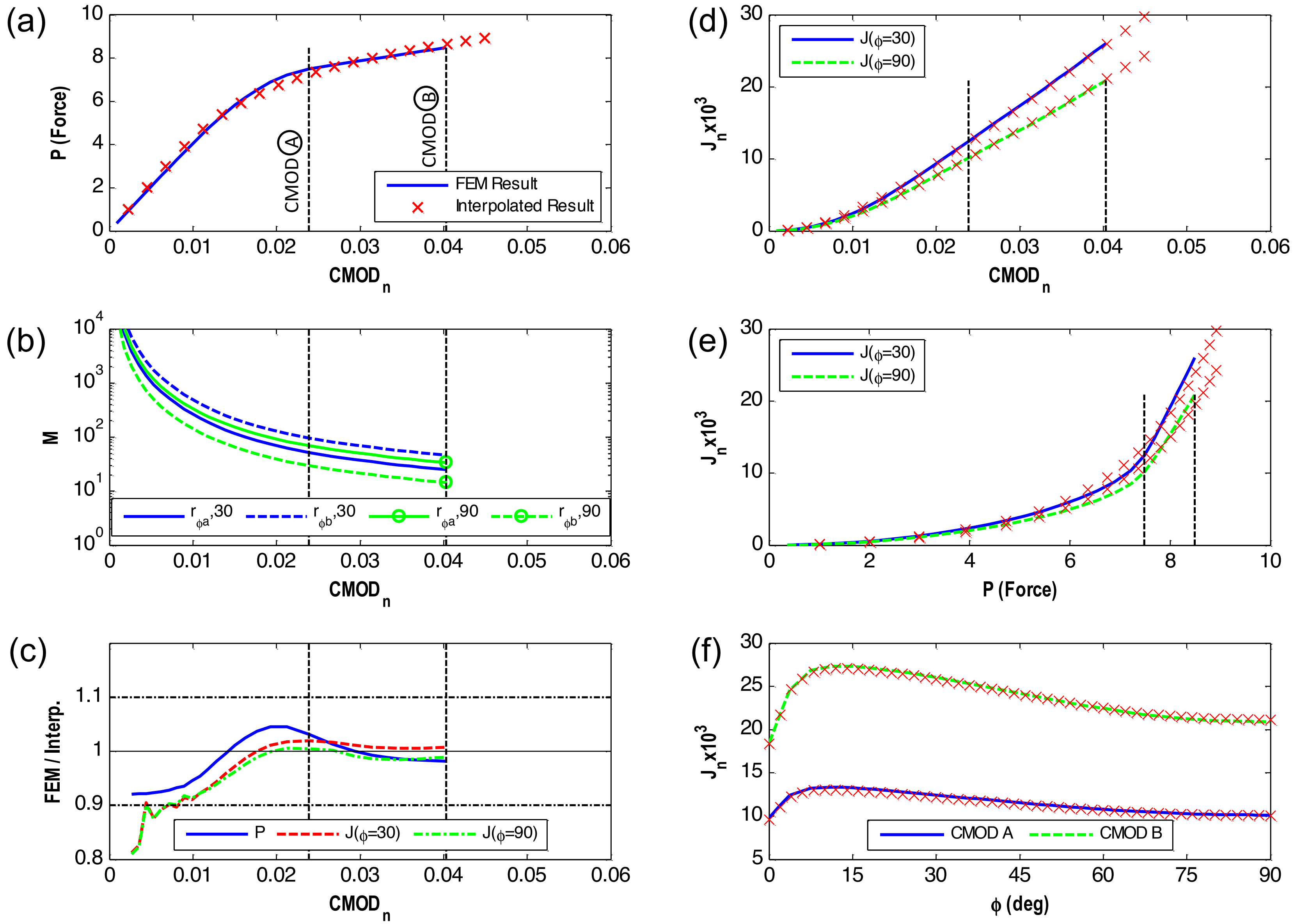

Figure B21. Comparison of benchmark model No. 21 FEM results and interpolated results for (a) P versus $CMOD_n$ (b) M versus $CMOD_n$, (c) benchmark FEM/interpolated results versus $CMOD_n$, (d) J_n versus $CMOD_n$ at $\phi = 30°$ and 90°, (e) J_n versus P at $\phi = 30°$ and 90°, and (f) J_n versus ϕ for $CMOD_n$ values A and B.

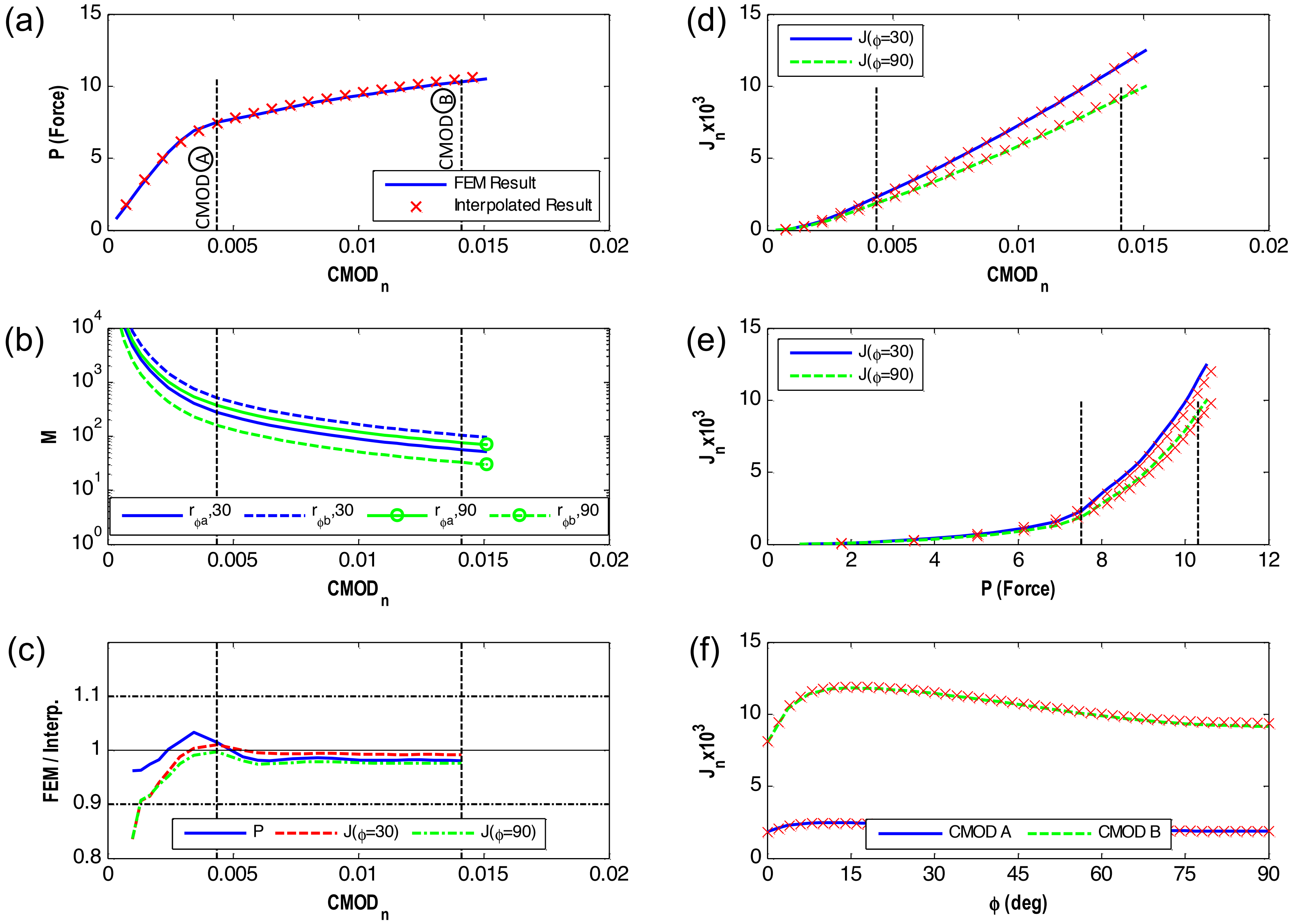

Figure B22. Comparison of benchmark model No. 22 FEM results and interpolated results for (a) P versus $CMOD_n$ (b) M versus $CMOD_n$, (c) benchmark FEM/interpolated results versus $CMOD_n$, (d) J_n versus $CMOD_n$ at $\phi = 30°$ and 90°, (e) J_n versus P at $\phi = 30°$ and 90°, and (f) J_n versus ϕ for $CMOD_n$ values A and B.

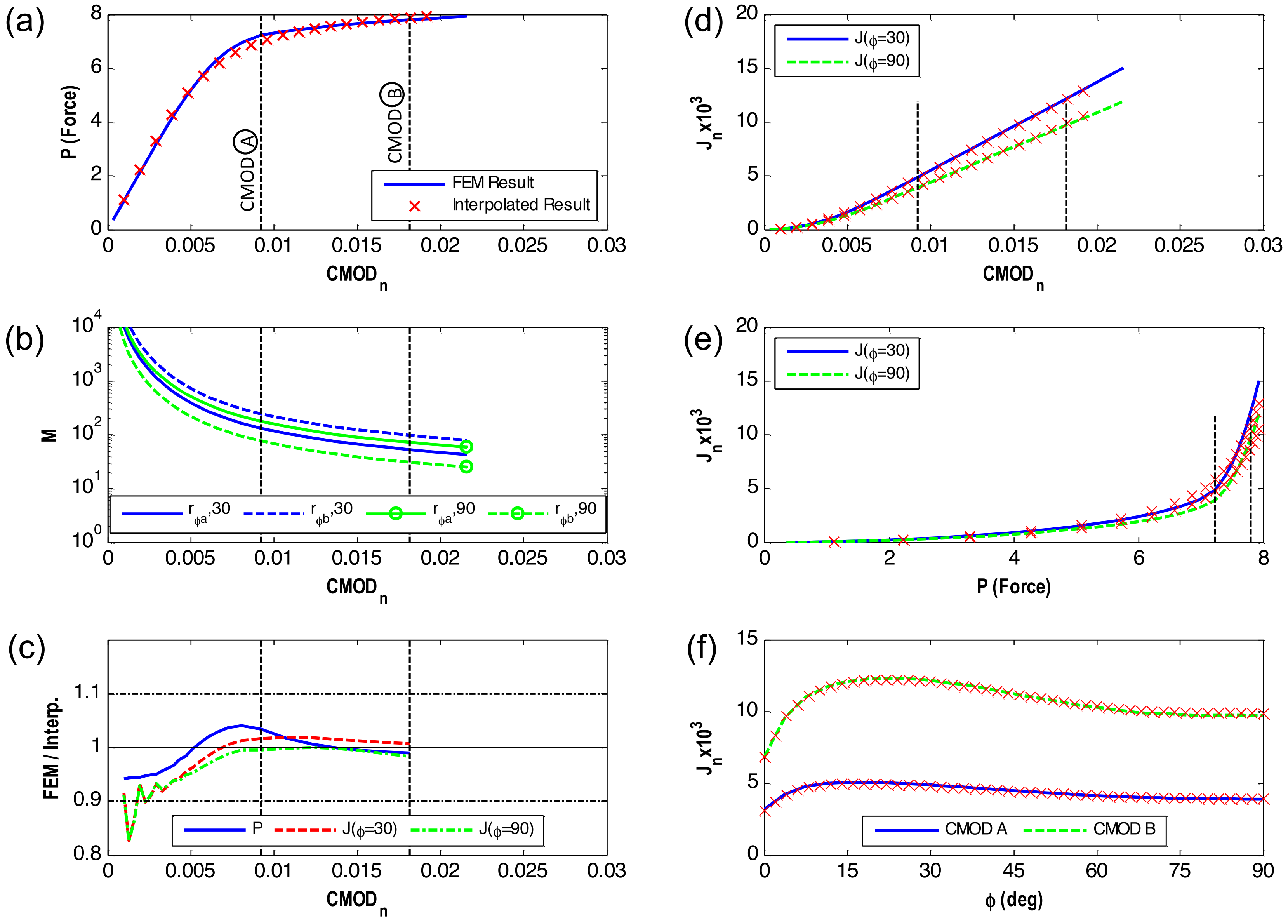

Figure B23. Comparison of benchmark model No. 23 FEM results and interpolated results for (a) P versus $CMOD_n$ (b) M versus $CMOD_n$, (c) benchmark FEM/interpolated results versus $CMOD_n$, (d) J_n versus $CMOD_n$ at $\phi = 30°$ and 90°, (e) J_n versus P at $\phi = 30°$ and 90°, and (f) J_n versus ϕ for $CMOD_n$ values A and B.

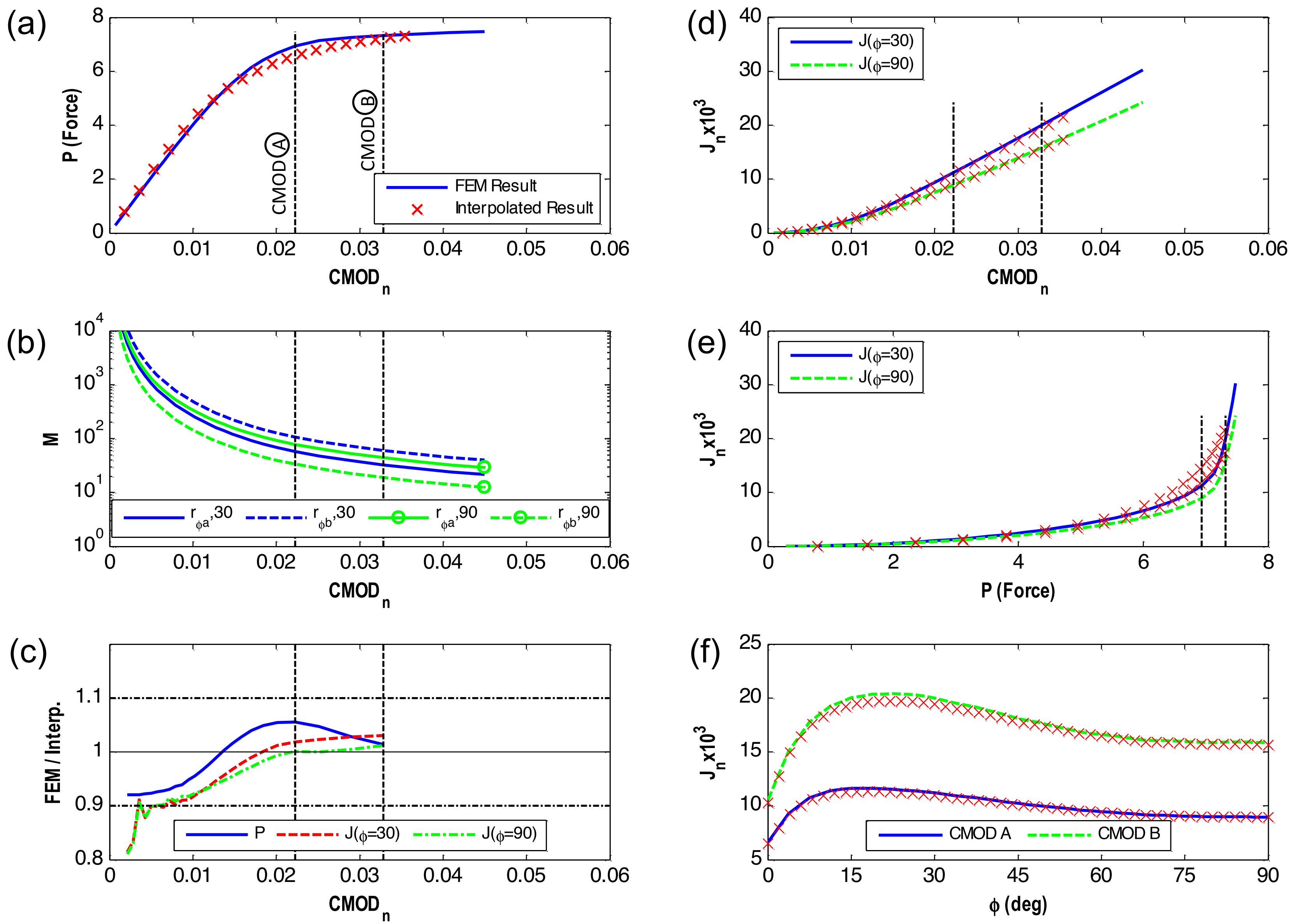

Figure B24. Comparison of benchmark model No. 24 FEM results and interpolated results for (a) P versus $CMOD_n$ (b) M versus $CMOD_n$, (c) benchmark FEM/interpolated results versus $CMOD_n$, (d) J_n versus $CMOD_n$ at $\phi = 30°$ and 90°, (e) J_n versus P at $\phi = 30°$ and 90°, and (f) J_n versus ϕ for $CMOD_n$ values A and B.

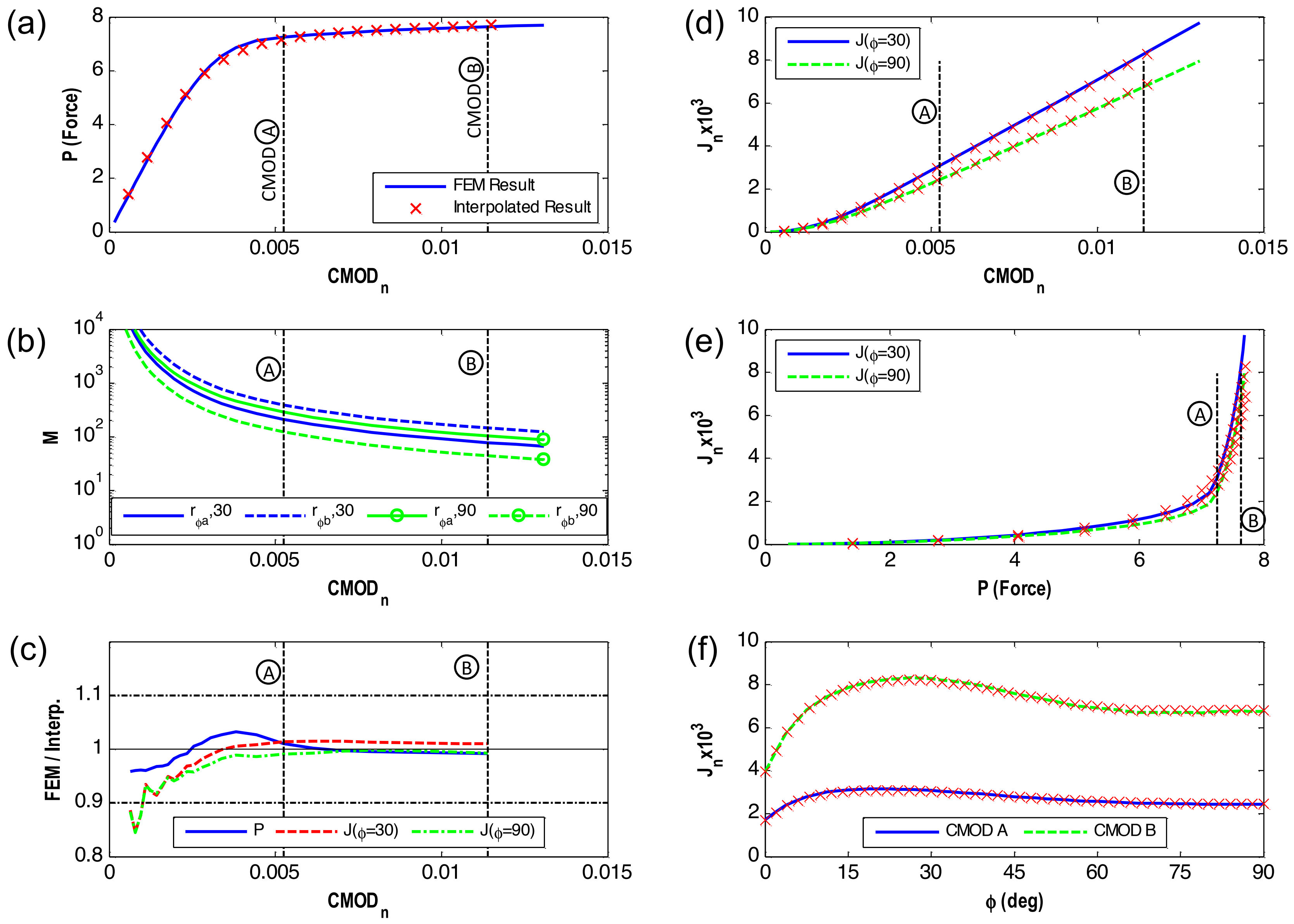

Figure B25. Comparison of benchmark model No. 25 FEM results and interpolated results for (a) P versus $CMOD_n$ (b) M versus $CMOD_n$, (c) benchmark FEM/interpolated results versus $CMOD_n$, (d) J_n versus $CMOD_n$ at $\phi = 30°$ and 90°, (e) J_n versus P at $\phi = 30°$ and 90°, and (f) J_n versus ϕ for $CMOD_n$ values A and B.

APPENDIX C—FINITE ELEMENT MODELS SOLUTION DATABASE

The 600 finite element solutions developed for this work have been compiled into an easily indexed database for distribution. Each independent FEM solution database follows exactly the same format and has the same number of rows and columns. Table 4 shows an example of the database format for one model. Each model is given a unique 'index' name made up of the a/B, a/c, n, and E/σ_{ys} values joined by underscores, e.g. '0.20_0.20_3_100.' The geometry and material property values are then listed under their appropriate labels. Each FEM result is divided into 20 even increments (steps) of $CMOD_n$ based on the maximum $CMOD_n$ in the specific solution, and the J-integral, reaction force, and $CMOD$ results are interpolated to these 20 increments. Step numbers are listed in the far left column followed by the corresponding normalized far-field stress, σ_n, and $CMOD_n$ values. The remainder of the columns list the normalized J-integral values, J_n, for $0 \geq \phi \geq 90$ in 2° increments of ϕ for each of the 20 load steps. The database for each individual FEM terminates with the keyword 'end.' All of the FEM solutions are collected into a single tab delimited text file that can be easily processed by computer programs. The database file is available upon request from the NASA Center for Aerospace Information (CASI) at <http://www.sti.nasa.gov>.

Table 4. Example database format for FEM solutions

Index	***a/B***	***a/c***	***n***	***E*/Sys**	***W***	***B***	**Sys**					
0.20_0.20_3_100	**0.2**	**0.2**	**3**	**100**	**10**	**1**	**1**					
**	**	phi	0	2	4	6	8	10	12	…	88	90
step	stress	*CMOD*	J0	J2	J4	J6	J8	J10	J12	…	J88	J90
1	7.937E-02	8.397E-04	1.240E-05	1.235E-05	1.224E-05	1.255E-05	1.313E-05	1.392E-05	1.492E-05	…	4.948E-05	4.949E-05
2	1.586E-01	1.679E-03	4.581E-05	4.606E-05	4.562E-05	4.674E-05	4.889E-05	5.182E-05	5.554E-05	…	1.841E-04	1.841E-04
3	2.376E-01	2.519E-03	9.888E-05	1.013E-04	1.004E-04	1.028E-04	1.074E-04	1.138E-04	1.219E-04	…	4.034E-04	4.035E-04
4	3.161E-01	3.359E-03	1.695E-04	1.780E-04	1.772E-04	1.811E-04	1.890E-04	2.000E-04	2.142E-04	…	7.070E-04	7.072E-04
5	3.940E-01	4.198E-03	2.565E-04	2.772E-04	2.790E-04	2.850E-04	2.969E-04	3.138E-04	3.356E-04	…	1.103E-03	1.104E-03
6	4.711E-01	5.038E-03	3.566E-04	3.955E-04	4.045E-04	4.144E-04	4.311E-04	4.547E-04	4.854E-04	…	1.586E-03	1.587E-03
7	5.472E-01	5.878E-03	4.681E-04	5.302E-04	5.516E-04	5.685E-04	5.917E-04	6.231E-04	6.640E-04	…	2.152E-03	2.153E-03
8	6.222E-01	6.717E-03	5.907E-04	6.798E-04	7.185E-04	7.467E-04	7.787E-04	8.199E-04	8.724E-04	…	2.801E-03	2.802E-03
9	6.956E-01	7.557E-03	7.244E-04	8.449E-04	9.046E-04	9.479E-04	9.923E-04	1.046E-03	1.112E-03	…	3.525E-03	3.526E-03
10	7.669E-01	8.397E-03	8.697E-04	1.026E-03	1.110E-03	1.171E-03	1.231E-03	1.300E-03	1.383E-03	…	4.306E-03	4.308E-03
11	8.320E-01	9.236E-03	1.021E-03	1.215E-03	1.325E-03	1.406E-03	1.482E-03	1.569E-03	1.670E-03	…	5.148E-03	5.150E-03
12	8.887E-01	1.008E-02	1.185E-03	1.423E-03	1.561E-03	1.663E-03	1.758E-03	1.863E-03	1.985E-03	…	6.002E-03	6.004E-03
13	9.355E-01	1.092E-02	1.354E-03	1.641E-03	1.809E-03	1.935E-03	2.049E-03	2.175E-03	2.319E-03	…	6.872E-03	6.874E-03
14	9.701E-01	1.176E-02	1.513E-03	1.848E-03	2.046E-03	2.196E-03	2.330E-03	2.477E-03	2.643E-03	…	7.754E-03	7.755E-03
15	9.914E-01	1.260E-02	1.658E-03	2.040E-03	2.268E-03	2.440E-03	2.595E-03	2.762E-03	2.950E-03	…	8.646E-03	8.648E-03
16	1.012E+00	1.343E-02	1.797E-03	2.225E-03	2.481E-03	2.675E-03	2.850E-03	3.037E-03	3.246E-03	…	9.544E-03	9.546E-03
17	1.030E+00	1.427E-02	1.917E-03	2.389E-03	2.670E-03	2.885E-03	3.077E-03	3.282E-03	3.512E-03	…	1.046E-02	1.046E-02
18	1.048E+00	1.511E-02	2.035E-03	2.553E-03	2.861E-03	3.096E-03	3.307E-03	3.532E-03	3.783E-03	…	1.138E-02	1.139E-02
19	1.067E+00	1.595E-02	2.154E-03	2.720E-03	3.057E-03	3.313E-03	3.542E-03	3.788E-03	4.060E-03	…	1.233E-02	1.233E-02
20	1.086E+00	1.679E-02	2.274E-03	2.889E-03	3.255E-03	3.532E-03	3.781E-03	4.047E-03	4.342E-03	…	1.327E-02	1.327E-02
end												

APPENDIX D—BENCHMARK FINITE ELEMENT MODELS SOLUTION DATABASE

The 25 benchmark finite element solutions developed for this work have been complied into an easily indexed database for distribution. The solution database follows the same format as the 600 model FEM database described in appendix C. The database file is available upon request from the NASA Center for Aerospace Information (CASI) at <http://www.sti.nasa.gov>.

REFERENCES

1. FEACrack, Quest Integrity Group, <http://www.questintegrity.com/products/feacrack-3D-crack-mesh-software/>, Verified December 12, 2012.

2. ABAQUS/CAE, Dassault Systèmes. <http://www.3ds.com/products/simulia/portfolio/abaqus/abaqus-portfolio/abaquscae/>, Verified January 16, 2013.

3. Newman, J.C.; and Raju, I.S.: Stress-Intensity Factor Equations for Cracks in Three-Dimensional Finite Bodies Subjected to Tension and Bending Loads, NASA/TM—1984–85793, Langley Research Center, VA, April 1984.

4. Newman, J.C.; Reuter, W.G.; and Aveline, C.R.: "Stress and Fracture Analyses of Semi-Elliptical Surface Cracks," *Fatigue and Fracture Mechanics*, P.C. Harris and K.L. Jerina (eds.), American Society of Testing and Materials, West Conshohocken, PA, Vol. 30, pp. 403–423, January 2000.

5. NASGRO, Southwest Research Institute, <http://www.swri.org/4org/d18/mateng/matint/nasgro/default.htm>, Verified January 16, 2013.

6. McClung, R.C.; Chell, G.G.; Lee, Y.D.; et al.: Development of a Practical Methodology for Elastic-Plastic and Fully Plastic Fatigue Crack Growth, NASA/CR—1999–209428, Marshall Space Flight Center, AL, July 1999.

7. Anderson, T.L.: *Fracture Mechanics: Fundamentals and Applications*, 3rd ed., CRC Press, Boca Raton, FL, 2005.

8. Kumar, V.; German, M.D.; and Shih, C.F.: An Engineering Approach for Elastic-Plastic Fracture Analysis, Tech. Rep. NP-1931, Electric Power Research Institute, Schenectady, NY, July 1981.

9. Kumar, V.; German, M.D.; Wilkening, W.W.; et al.: Advances in Elastic-Plastic Fracture Analysis, Tech. Rep. NP-3607, Electric Power Research Institute, Schenectady, NY, August 1984.

10. Kumar, V.; and German, M.D.: Elastic-Plastic Fracture Analysis of Through-Wall and Surface Flaws in Cylinders, Tech. Rep. NP-5596, Electric Power Research Institute, Schenectady, NY, January 1988.

11. Ainsworth, R.A.: "The assessment of defects in structures of strain hardening material," *Engineering Fracture Mechanics*, Vol. 19, No. 4, pp. 633–642, 1984.

12. Ramberg, W.; and Osgood, W.R.: Description of Stress-Strain Curves by Three-Parameters, Technical Note 902, National Advisory Committee on Aeronautics, Washington, DC, April 1943.

13. Yagawa, G.; Yasumi, K.; and Hiroyoshi, U.: “Three-dimensional fully plastic solutions for semi-elliptical surface cracks,” *International Journal of Pressure Vessels and Piping*, Vol. 53, No. 3, pp. 457–510, 1993.

14. Wilson, C.D.; and Natarajan, K.R.: Verification of NASGRO Elastic-Plastic Modules: J-Integral Computation, MCTR-03-03-01, Center for Manufacturing Research, Tennessee Technological University, TN, 2003.

15. Wang, X.: “Fully plastic J-integral solutions for surface cracked plates under biaxial loading,” *Engineering Fracture Mechanics*, Vol. 73, No. 11, pp. 1581–1595, March 2006.

16. Kim, Y.J.; Shim, D.J.; Choi, J.B.; and Young, J.K.: “Approximate J estimates for tension-loaded plates with semi-elliptical surface cracks,” *Engineering Fracture Mechanics*, Vol. 69, No. 13, pp. 1447–1463, September 2002.

17. Wells, D.N.; and Allen, P.A.: Analytical Round Robin for Elastic-Plastic Analysis of Surface Cracked Plates: Phase I Results, NASA/TM—2012–217456, Marshall Space Flight Center, AL, March 2012.

18. WARP3D, Static and Dynamic Nonlinear Analysis of Fracture in Solids, Dodds, R.H., University of Illinois at Urbana-Champaign, <http://code.google.com/p/warp3d/>, Verified December 12, 2012.

19. Matlab, Mathworks, <http://www.mathworks.com/products/matlab/>, Verified December 12, 2012.

20. Brocks, W.; and Scheider, I.: “Reliable J-Values: Numerical aspects of the path-dependence of the J-integral in incremental plasticity,” *Materialprüfung*, Vol. 45, No. 6, pp. 264–275, 2003.

REPORT DOCUMENTATION PAGE

Form Approved
OMB No. 0704-0188

1. REPORT DATE *(DD-MM-YYYY)* 01–04–2013	**2. REPORT TYPE** Technical Publication	**3. DATES COVERED** *(From - To)*

4. TITLE AND SUBTITLE

Elastic-Plastic J-Integral Solutions for Surface Cracks in Tension
Using an Interpolation Methodology

5a. CONTRACT NUMBER

5b. GRANT NUMBER

5c. PROGRAM ELEMENT NUMBER

6. AUTHOR(S)

P.A. Allen and D.N. Wells

5d. PROJECT NUMBER

5e. TASK NUMBER

5f. WORK UNIT NUMBER

7. PERFORMING ORGANIZATION NAME(S) AND ADDRESS(ES)

George C. Marshall Space Flight Center
Huntsville, AL 35812

8. PERFORMING ORGANIZATION REPORT NUMBER

M–1356

9. SPONSORING/MONITORING AGENCY NAME(S) AND ADDRESS(ES)

National Aeronautics and Space Administration
Washington, DC 20546–0001

10. SPONSORING/MONITOR'S ACRONYM(S)

NASA

11. SPONSORING/MONITORING REPORT NUMBER

NASA/TP—2013–217480

12. DISTRIBUTION/AVAILABILITY STATEMENT

Unclassified-Unlimited
Subject Category 39
Availability: NASA CASI (443–757–5802)

13. SUPPLEMENTARY NOTES

Prepared by the Materials and Processes Laboratory, Engineering Directorate
Supplemental database files available upon request.

14. ABSTRACT

No closed form solutions exist for the elastic-plastic *J*-integral for surface cracks due to the nonlinear, three-dimensional nature of the problem. Traditionally, each surface crack must be analyzed with a unique and time-consuming nonlinear finite element analysis. To overcome this shortcoming, the authors have developed and analyzed an array of 600 3D nonlinear finite element models for surface cracks in flat plates under tension loading. The solution space covers a wide range of crack shapes and depths (shape: $0.2 \le a/c \le 1$, depth: $0.2 \le a/B \le 0.8$) and material flow properties (elastic modulus-to-yield ratio: $100 \le E/ys \le 1{,}000$, and hardening: $3 \le n \le 20$). The authors have developed a methodology for interpolating between the goemetric and material property variables that allows the user to reliably evaluate the full elastic-plastic *J*-integral and force versus crack mouth opening displacement solution; thus, a solution can be obtained very rapidly by users without elastic-plastic fracture mechanics modeling experience. Complete solutions for the 600 models and 25 additional benchmark models are provided in tabular format.

15. SUBJECT TERMS

structural mechanics, metals and metallic materials

16. SECURITY CLASSIFICATION OF:			**17. LIMITATION OF ABSTRACT**	**18. NUMBER OF PAGES**	**19a. NAME OF RESPONSIBLE PERSON**
a. REPORT	**b. ABSTRACT**	**c. THIS PAGE**			STI Help Desk at email: help@sti.nasa.gov
U	U	U	UU	104	**19b. TELEPHONE NUMBER** *(Include area code)* STI Help Desk at: 443–757–5802

National Aeronautics and
Space Administration
IS20
George C. Marshall Space Flight Center
Huntsville, Alabama 35812